



Faculteit Bio-ingenieurswetenschappen

Academiejaar 2010 – 2011

Characterizing spatial variability of tropical rainforest
structure using hemispherical photography, in the reserves of
Yangambi and Yoko (Democratic Republic of Congo)

Elizabeth Kearsley

Promotoren: Dr. ir. Hans Verbeeck, Prof. Dr. ir. Robert De Wulf

Tutor: ir. Marjolein De Weirdt

Masterproef voorgedragen tot het behalen van de graad van
Master in de bio-ingenieurswetenschappen: Milieutechnologie

De auteur en de promotoren geven de toelating deze scriptie voor consultatie beschikbaar te stellen en delen ervan te kopiëren voor persoonlijk gebruik. Elk ander gebruik valt onder de beperkingen van het auteursrecht, in het bijzonder met betrekking tot de verplichting uitdrukkelijk de bron te vermelden bij het aanhalen van resultaten uit deze scriptie.

The author and promoters give the permission to use this thesis for consultation and to copy parts of it for personal use. Every other use is subject to the copyright laws, more specifically the source must be extensively specified when using results from this thesis.

Gent, juni 2011

Dr. ir. H. Verbeeck

Prof. Dr. ir. R. De Wulf

E. Kearsley

Acknowledgements

After a whole year of working, reading and writing, I can finally say that this long process is finished. My thesis is obviously not just my own credit and I want to thank everyone involved appropriately.

In the first place, my greatest gratitude and thanks go to dr. ir. Hans Verbeeck for giving me the opportunity to work on this project, for his support and excellent coaching. I also thank you for reviewing my work.

I also greatly thank Prof. Dr. ir. Robert De Wulf for broadening my knowledge, particularly with regard to tropical forests. I must also thank you for your critical reading and remarks.

I am enormously thankful to Marjolein De Weirdt, my supervisor, for her encouragement, guidance, support, and correction of my thesis. Your door was always open for consultations and to discuss results. I am very grateful that we could work together and that I could learn from you.

The fieldwork was performed in DRC in collaboration with the University of Kisangani. I want to thank Prof. Maté for both receiving and guiding us and for the use of the university's facilities during my stay in Kisangani. A special thank you goes out to Wannes Hubau for his constant guidance and support during my stay there.

I offer my thanks and blessings to all of those who supported me in any respect during the completion of this project. Geert Baert, Eef Meerschman, Frieke Van Coillie and Inge Jonckheere deserve special mention.

A warm thank you also to Kaat Verbiest and Egwin Minami for just being wonderful.

Finally, I would like to express my special gratitude to my parents. Five years ago they gave me the opportunity to follow this education. Thank you for your patience.

Samenvatting

In deze studie wordt het gebruik van hemisferische fotografie voor de bepaling van de horizontale component van kruinstructuur in het tropisch regenwoud onderzocht. Tijdens de zomer van 2010 werd een veldcampagne uitgevoerd in primair en transitiewoud in de reserves van Yangambi, Yoko en Masako in de Democratische Republiek Congo. De effectieve bladoppervlakte index (effective leaf area index, L_e) en de kruin openheid (canopy openness, CO) werden gemeten met behulp van de indirecte optische techniek van de hemisferische kruin fotografie.

Ruimtelijke variabiliteit van de kruinstructuur is onderzocht op een lokale schaal en op een meer regionale schaal. Vier sites in primair woud worden onderzocht, waarvan drie met een grootte van 9ha en één van 80ha. Vijf kleinere sites zijn geselecteerd in het transitiewoud, waar directe metingen van de bladoppervlakte index (leaf area index, LAI) ook werden uitgevoerd met als doel de validering van de indirecte methode. Er is geen significant verschil gevonden tussen structurele parameters van de verschillende sites van primair woud. Over het algemeen is een gemiddelde waarde van 4,0 voor L_e gevonden variërend tussen 2,6 en 7,4 en een gemiddelde waarde van 3,0% CO, variërend tussen 1,1% en 6,4%. Een significant verschil werd gevonden tussen de percelen in primair woud en transitiewoud, met een lagere schatting van L_e in transitiewoud en een hogere schatting van CO.

Naast de eigenlijke karakterisering van de kruinstructuur, is dit werk gericht op het onderzoek van de bruikbaarheid van de methode van hemisferische fotografie in tropisch regenwoud. We slaagden er niet in om nauwkeurige schattingen van LAI te maken met behulp van hemisferische fotografie, voornamelijk als gevolg van de complexe verdeling van bladeren in de kruin. De schattingen zijn niet absoluut doordat een aantal ruwe aannames genomen zijn betreffende de extinctiecoëfficiënt, en de distributie en de bladhoek in de kruin. De schattingen zijn ook erg afhankelijk van de belichting gebruikt tijdens de verwerving van de beelden, waarbij onderbelichting een nauwkeuriger resultaat gaf. De L_e waarden werden vergeleken met LAI schatting op basis van directe metingen, maar door moeilijkheden met beide methoden waren we niet in staat om de L_e schattingen echt te valideren. De schatting van de CO blijkt meer betrouwbaar omdat de aannames niet van belang waren voor de bepaling van deze parameter.

Er wordt besloten dat hemisferische fotografie op zich voldoende gevoelig is om het grote bereik aan LAI waarden in tropisch regenwoud vast te leggen, maar om een goede beschrijving van de complexe kruinstructuur te bieden is extra informatie. Een onafhankelijke beoordeling van de verdeling van de bladeren in de kruin zou een belangrijke verbetering geven van de resultaten afgeleid uit de hemisferische foto's.

Abstract

In this study, the use of hemispherical photography for determination of the horizontal component of canopy structure in tropical rainforest is examined. During the summer of 2010 a field campaign was carried out in primary and transition forest in the reserves of Yangambi, Yoko and Masako in the Democratic Republic of Congo. The effective leaf area index (L_e) and the canopy openness (CO) were measured using the indirect optical technique of hemispherical canopy photography.

Spatial variability of the canopy structure is studied on a local scale and on a more regional scale. Four sample plots in primary forest are examined, three of which are 9ha and one is 80ha. Five smaller sites are selected in transition forest, where direct measurements of leaf area index (LAI) are also conducted with the purpose to serve as validation for the indirect method. No significant difference is found between structural parameters of the different sample plots in the primary forest sites. Overall, a mean of 4.0 for L_e is found ranging between 2.6 and 7.4, and a mean of 3.0% CO ranging between 1.1% and 6.4%. A significant difference is found between plots in primary and transition forests, with a lower L_e estimate and more canopy openness in transition forests.

Next to the actual characterization of the canopy structure, this work focuses on the usefulness of the method of hemispherical canopy photography in tropical rainforest. We did not succeed in providing accurate estimates of LAI using hemispherical photography mainly due to the complex distribution of leaves in the canopy. The estimates were not absolute due to some crude assumptions made concerning light extinction, and the distribution and inclination of leaves in the canopy. The obtained estimates are also very dependent on the exposure setting used during images acquisition, with underexposure providing a more accurate result. The L_e values were compared to LAI estimation based on direct measurements, but due to difficulties encountered with both methods, we were not able to validate L_e estimates calculated from the hemispherical images. The estimation of CO is shown to be more reliable since the assumptions were of no importance for its estimation.

It is concluded that hemispherical canopy photography on its own is sensitive enough for the wide range of LAI values encountered in tropical forest, but to provide a good description of the complex canopy structure, auxiliary information is needed. An independent assessment of the distribution of the leaves within the canopy would greatly improve the results retrieved from the hemispherical images.

Contents

List of abbreviations.....	i
List of figures	ii
List of tables	iii
1 Introduction	1
2 Literature review.....	2
2.1 Central African tropical rainforests	2
2.2 Canopy structure	4
2.3 Leaf area index	5
2.3.1 Methods of LAI measurement.....	5
2.3.2 Leaf area index measurements in tropical rainforests	7
2.4 Canopy openness	10
2.5 Hemispherical canopy photography.....	10
2.5.1 Image acquisition.....	12
2.5.2 Image analysis.....	12
2.5.3 Sources of errors.....	17
2.6 Spatial variability	19
3 Materials and methods	20
3.1 Study sites and sampling scheme.....	20
3.1.1 Yoko study site.....	20
3.1.2 Yangambi study site.....	22
3.1.3 Masako study site	23
3.1.4 Site comparison	23
3.2 Data acquisition.....	24
3.2.1 Weather conditions	26
3.2.2 Direct measurements as validation	26
3.3 Data processing.....	26
3.3.1 Channel selection.....	27
3.3.2 Selected thresholding methods.....	27
3.3.3 Lens calibration.....	31
3.4 Spatial variability	31
3.4.1 Geostatistics	32
4 Results	35
4.1 Software comparison - thresholding methods.....	35

4.2	Comparison with direct measurements	39
4.2.1	Plots in transition forest.....	39
4.2.2	Individual trees	39
4.3	Differences during image acquisition and analysis	40
4.3.1	Weather conditions	40
4.3.2	Zenith angle	41
4.3.3	Gap fraction distributions	42
4.3.4	Exposure settings.....	42
4.3.5	Channels of RGB	43
4.4	Spatial variation – Primary forest.....	45
4.4.1	Variation of the forest structure.....	45
4.4.2	Patterns of variation of structural parameters.....	46
5	Discussion	53
5.1	Part 1: Assessment of hemispherical canopy photography.....	53
5.1.1	Structural parameters and the associated inaccuracies	53
5.1.2	Factors during image acquisition.....	55
5.1.3	Analysis of the images.....	56
5.2	Part 2: Spatial variability of canopy structure	58
5.2.1	Spatial dependency and sampling scheme	58
5.2.2	Intra-site variability.....	58
5.2.3	Inter-site variability.....	59
6	Conclusion	60
7	References	61
8	Appendix.....	I
8.1	Lens distortion.....	I
8.2	Matlab script: ECOM.....	II
8.2.1	L_e calculation.....	II
8.2.2	Circle and segments description.....	VIII
8.3	MAS/2010/1: Species	IX
8.4	Location maps	X
8.4.1	YAN/I.....	X
8.4.2	YOK/I	XII
8.4.3	YOK/II	XIV
8.4.4	YOK/III	XVI

8.4.5	YOK/II/III.....	XVIII
8.5	Interpolation maps	XX
8.5.1	YOK/I	XX
8.5.2	YOK/II	XXV
8.5.3	YOK/II/III.....	XXXI
8.5.4	YAN/I.....	XXXVII

List of abbreviations

DRC	Democratic Republic of Congo
LAI	Leaf area index
PAI	Plant area index
VAI	Vegetation area index
WAI	Wood area index
L_e	Effective leaf area index
CO	Canopy openness
PPFD	Photosynthetic photon flux density
PAR	Photosynthetically active radiation
SLA	Specific leaf area
GLA	Gap Light Analyzer
FOV	Field of view
RGB	Red - Green - Blue
OTV	Optimal thresholding value
ECOM	Entropy crossover method
TRAC	Tracing Radiation and Architecture of Canopies
YAN	Yangambi
YOK	Yoko
MAS	Masako

List of figures

Figure 1: Land cover map of Central African tropical forest.	3
Figure 2: The projection as seen with a hemispherical lens looking upward.....	11
Figure 3: Maps with exact sample locations.	21
Figure 4: Regular grid sampling scheme.	22
Figure 5: Example of hemispherical photograph.....	25
Figure 6: Projection transformation in GLA.....	31
Figure 7: The variogram and its characteristics.....	33
Figure 8: Overall assessment of $L_e(60^\circ, ue)$ of each forest type.....	35
Figure 9: Scatterplots comparing the thresholds selected using different thresholding methods.....	37
Figure 10: Scatterplots comparing derived $L_e(75^\circ)$ using different thresholding methods.	37
Figure 11: Comparison of different L_e values and direct LAI in transition forest.	39
Figure 12: Estimated $L_e(60^\circ, ue)$ and direct LAI during clearcut experiment.	40
Figure 13: Scatterplot comparing parameters acquired from images taken in different weather conditions.....	41
Figure 14: Comparison of L_e analysed using zenith angles 60° and 75°	42
Figure 15: Different gap fraction distributions.....	42
Figure 16: Comparison of parameters obtained from images acquired with a different exposure setting.	43
Figure 17: Multiple colour channels.	44
Figure 18: Experimental variograms and fitted theoretical variogram models for different plots in primary forest (from standard exposed images).....	49
Figure 19: Experimental variograms and fitted theoretical variogram models for different plots in primary forest (from underexposed images).	50
Figure 20: Interpolation maps of all structural parameters of YOK/II, st.....	51
Figure 21: Comparison of structural parameters of YOK/II, st.....	52
Figure 22: Interpolation maps for $L_e(60^\circ, st)$ and $L_e(75^\circ, st)$ for plot YOK/I.	52

List of tables

Table 1: Overview of methods for in situ leaf area index determination.....	6
Table 2: Levels at which errors can be introduced in hemispherical photography.....	18
Table 3: Overview of mean parameters of transition forests.	35
Table 4: Comparison of threshold methods.....	36
Table 5: Comparison of replication of manual thresholding method.....	38
Table 6: Comparison of thresholding methods after averaging structural parameters for every measurement location.....	38
Table 7: Results of images acquired in different weather conditions.	41
Table 8: Results of different colour channel analysis.	44
Table 10: Comparison of the means of different plots.	45
Table 9: Summary statistics of every plot in primary forest.	46
Table 11: Characteristics of the variograms for primary forest.	48

1 Introduction

The response of vegetation to a globally changing climate is crucial for the prediction of future atmospheric CO₂ concentrations. Tropical forests play a critical role because of their high carbon content and productivity. Large uncertainties exist about the response of Central African rainforests and their contribution to the global CO₂ budget, because of the absence of an extensive observation network. The contribution of Africa to the global carbon cycle is characterized by its low fossil fuel emissions, an increasing population which causes cropland expansion, and degradation and deforestation risk (de Wasseige *et al.*, 2009; Ciais *et al.*, 2011). Under the UN initiative REDD (Reducing Emissions from Deforestation and forest Degradation), countries with tropical forests can receive financial compensation for the preservation of their forests within the global CO₂ trading mechanism. It is therefore important for countries like the Democratic Republic of Congo (DRC) to identify and monitor the carbon stocks and fluxes in their forest ecosystems.

In this project, fieldwork was performed in DRC in collaboration with the University of Kisangani with the goal to contribute to the identification of carbon stocks and fluxes in the tropical rainforest. The focus of this study lies on leaf biomass. To estimate the carbon and water exchange between vegetation and the atmosphere the ecosystem, leaf area is a crucial scaling factor since leaves are the interface between the vegetation and the atmosphere. This work will provide more insight in the spatial variability of the leaf area and biomass in Central African tropical forests. Moreover, these kinds of field data are very useful for the ground validation of remote sensing data.

This study focuses on characterizing spatial variability of the canopy structure by the structural variables leaf area index (LAI) and canopy openness (CO). LAI is an interesting variable because of its close relationship with forest productivity and biogeochemical cycles. Light availability is also closely related to the canopy structure, and represented in this study by the CO.

The characterization of canopy structure and the understanding of its variability is a challenging task. Much of the variation in tropical forest structure and dynamics is still unknown due to the difficult access and the vastness of these biomes. Many different methods exist to characterize the forest structure, depending on the purposes and the available time. During my fieldwork in 2010, the technique of hemispherical photography was selected to characterize the canopy structure and assess the spatial variability. This study aims to assess the usefulness of hemispherical canopy photography in characterizing spatial variation in canopy structure in tropical rainforest. Therefore hemispherical photography is examined throughout the multiple steps from image acquisition to image analysis, and some key questions are tackled including settings of the camera, weather conditions during image acquisitions, appropriate sampling scheme, how to obtain fast and reliable results from numerous images and accuracy of analysis software. The obtained parameters are then used to characterize spatial variability in canopy structure in primary forest. Differences between primary and transition forests are also examined.

2 Literature review

2.1 Central African tropical rainforests

Tropical rainforests in general are characterized by a high biodiversity and a very large phytomass, as well as a complicated and irregular canopy structure (Trichon *et al.*, 1998). Tropical forests are especially important as carbon stock as they contain circa 13% of the global carbon stock of all terrestrial ecosystems and account for circa 30% of the terrestrial photosynthetic activity (Clark *et al.*, 2008). Climate, both regionally as well as globally, is to a large extent regulated by tropical rainforests because of their size and vast carbon stocks (Malhado *et al.*, 2009). Despite the large, extensive area of this rainforest and its important role in the global biosphere, there remains a lack of consistent information on its structure and function.

Central Africa has the second largest continuous block of tropical rainforest in the world, after the Amazon basin, with a forested area of 288 million ha. This block covers large parts of 6 countries: Cameroon, Congo (Brazzaville), the Democratic Republic of Congo (DRC), the Central African Republic, Gabon and Equatorial Guinea. The forest cover categories included as forested area are lowland dense forest, submontane forest, montane forest, swamp forest, mangrove, forest-cropland mosaic, forest-savanne mosaic and dense deciduous forest (Miombo). A detailed land cover map of the Central African tropical forest is shown in Figure 1. This study will pertain to moist evergreen forest.

DRC has a total forest area of 154 million ha (FAO, 2010), of which 54% is lowland dense forest (de Wasseige *et al.*, 2009), where the experimental area of this study is located. Currently the deforestation rates in DRC are very low, with an annual net loss of forest area of 0.20%, from 2000 until 2010 (FAO, 2010). The deforestation phenomenon remains relatively modest in the entire Congo Basin and although disturbed in a few places, overall the forest cover is very well preserved. (de Wasseige *et al.*, 2009).

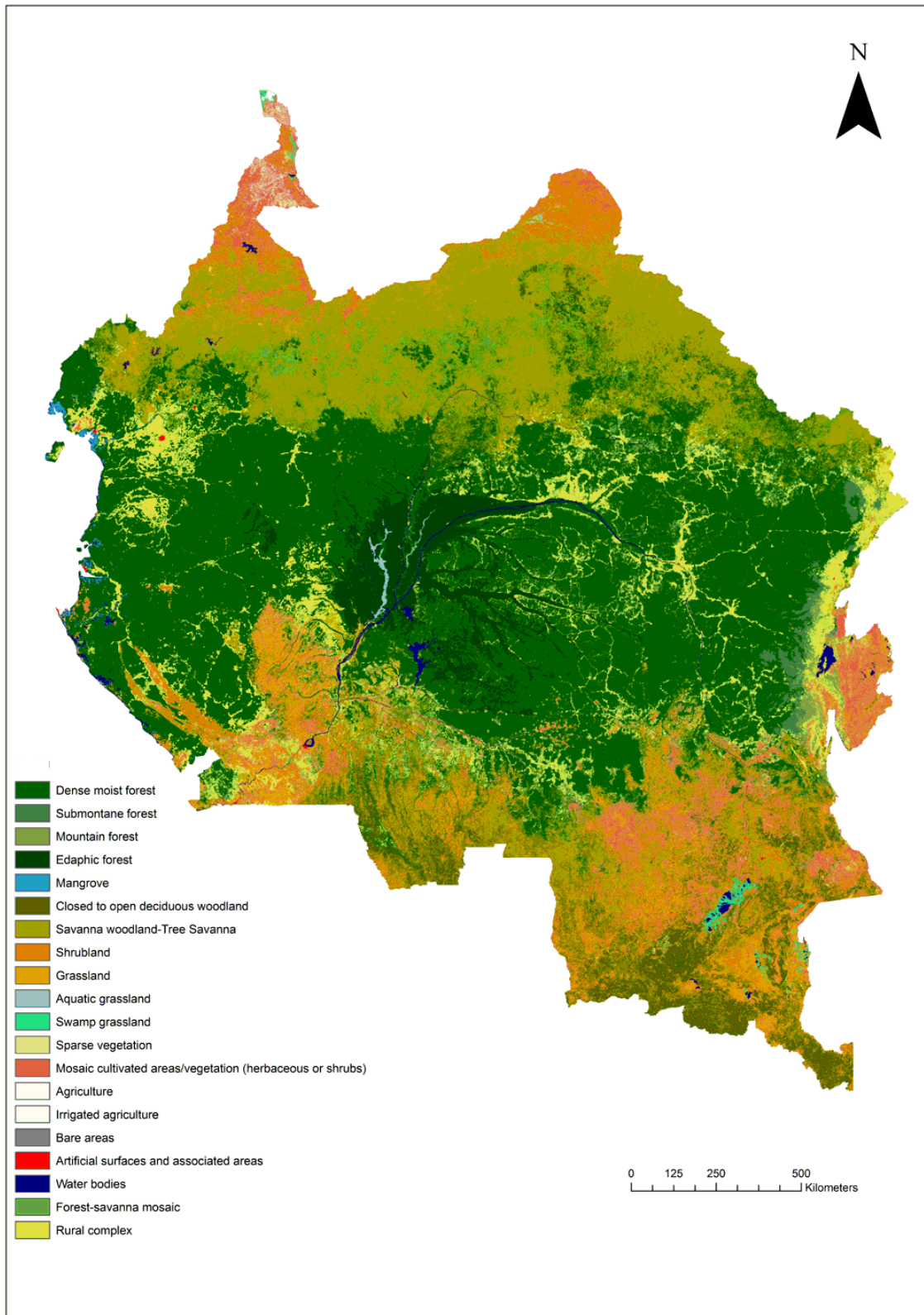


Figure 1: Land cover map of Central African tropical forest, based on information from 19 months of ENVISAT MERIS FRS observation and 8 years of SPOT VEGETATION time series (Verhegghen and Defourny, 2010).

2.2 Canopy structure

A description of the canopy structure is crucial to achieve an understanding of plant processes, because it influences plant-environment interactions (Norman and Campbell, 1989). The forest canopy acts as a functional interface between 90% of the terrestrial biomass and the atmosphere (Jonckheere *et al.*, 2005) and therefore, the canopy structure affects the exchange of energy and mass between the vegetation and its environment. The understanding of the canopy structure can facilitate insight into adaptation of vegetation to changes of physical, chemical or biotic factors (Norman and Campbell, 1989). In this time of global change, insight in these adaptations is of paramount importance.

Canopy structure, simply stated, is the amount and organization of above ground plant material (Norman and Campbell, 1989). Canopy structure can be characterized by variables such as orientation and positional distribution of leaves, shape and size of vegetation elements and by distribution of optical properties (Weiss *et al.*, 2004). Consequently, a large amount of data is necessary to give a detailed description of the canopy structure. However, an accurate description of canopy architecture is difficult because of the spatial and temporal variability. Additionally, the complexity increases when the focus varies from an individual tree, to pure stands, to heterogeneous stands (Norman and Campbell, 1989).

When more specifically looking at the canopy structure of tropical rainforest, it is often stated that the forest is stratified, meaning that the woody plants can be grouped into several height classes. The area from ground level to the tops of the tallest trees is never uniformly filled; there are always more leaves and branches at some levels than at others (Richards, 1996). The amount of stories of which the forest is built up is not clear and can be a matter of taste, but generally three layers can be observed: upper, middle and lower canopy layer. Emergent trees are usually regarded as belonging to a separate but strongly discontinuous layer. Similar to vertical structure, there is an important horizontal heterogeneity. Natural tropical rainforests are never homogeneous in structure and can be considered a mosaic of patches in different developmental stages. Light availability is also closely related to these stages and the canopy structure (Chazdon and Fetcher, 1984). The forest structure also depends largely upon species composition and density. The density (number per unit area) of trees in tropical rainforest varies greatly and depends on many factors. In mature forest with few gaps on more or less level, free-draining lowland sites the number of trees per hectare with a diameter at breast height greater than or equal to 10cm is usually about 300-700 (Richards, 1996).

Most research describes the canopy structure by a single or only a few variables, for example the leaf area density and the leaf area index (LAI) (Weiss *et al.*, 2004). The plant area index (PAI) and vegetation area index (VAI) are also sometimes used when a distinction between the leaf and other vegetation elements (e.g. wood) cannot be made due to the applied measurement technique (Jonckheere *et al.*, 2004). The focus of this study lies on LAI and canopy openness. The PAI and VAI will also be discussed further on.

2.3 Leaf area index

Leaf area index (LAI) was first defined by Watson in 1947 as the total one-sided area of photosynthetic tissue per unit ground surface area, a dimensionless variable, sometimes expressed as $\text{m}^2 \cdot \text{m}^{-2}$. This definition is clear and applicable when foliage elements are flat, but causes confusion when the one-sided area is not clearly defined, as is the case with non-flat leaves and needles (Jonckheere *et al.*, 2004). Many attempts have been made to take the irregular shapes into account such as a (horizontal) projected leaf area, which is defined as the area of 'shadow' that would be cast by each leaf in the canopy with a light source at infinite distance and perpendicular to it, summed up for all leaves in the canopy (Asner *et al.*, 2003). Other definitions have been proposed, but most recent research uses the following definition of LAI: one half of the total leaf area per unit ground surface area (Jonckheere *et al.*, 2004), and this definition of LAI will also be used in this study. When comparing results of LAI of different researchers, attention must be paid to which definition is used (Asner *et al.*, 2003).

LAI is a very interesting variable in climate studies because it describes the size of the interface between plant and atmosphere and is therefore important to quantify the exchange of mass and energy (Weiss *et al.*, 2004). It is an important variable in forest studies for the assessment of net primary productivity and the carbon cycle, as it contributes to the derivation of photosynthetic activity (de Wasseige *et al.*, 2003). And as LAI is a dimensionless variable, it can be measured and analysed on multiple spatial scales, ranging from individual canopies to large regions (Asner *et al.*, 2003). According to Jonckheere *et al.* (2005), LAI is the most common and most useful comparative measure of vegetation structure of the forest canopy. It is a valuable parameter in wide range of models such as productivity models and other soil–vegetation–atmosphere transfer models (Meir *et al.*, 2000). It is used in models for upscaling leaf-level processes to stand level and for the evaluation of remote sensing products (Asner *et al.*, 2003).

The LAI is not a fixed parameter and largely depends upon species composition, canopy structure developmental stages, site conditions, management practices and seasonality (Jonckheere *et al.*, 2004; Scurlock *et al.*, 2001). It can vary every year due to forest dynamics (Jonckheere *et al.*, 2004). Additionally, the assessment method has an influence on the LAI determined. Scurlock *et al.* (2001) constructed a database of worldwide estimates of LAI from 1932 to 2000. As an overview, LAI estimates are represented per biome, although a more detailed description per measurement is available in the dataset (Scurlock *et al.*, 2001; Asner *et al.*, 2003). Widely varying values are found for different biomes. After removal of outliers, mean LAI for 15 different biomes range from 1.3 ± 0.9 for deserts to 8.7 ± 4.3 for tree plantations. Highest values are most commonly found in coniferous forest, with values of up to 15. For tropical evergreen broadleaf forests, a mean value of LAI of 4.8 ± 1.7 with a minimum of 1.5 and a maximum of 8.0 is reported. Leigh (1999) reported higher typical LAI values for lowland tropical rainforests, ranging between 6 and 8. More detailed LAI studies and values in tropical forests in different regions are discussed in section 2.3.2.

2.3.1 Methods of LAI measurement

Table 1 lists direct and indirect LAI estimation methods that were reviewed by Jonckheere *et al.* (2004). The focus of this research was on ground-based (in situ) measurements. Air- and spaceborne methods were not included in the review. A distinction is made between direct and indirect

measurements. Direct methods are assumed to be more accurate, but also have important drawbacks, such as being very time-consuming, laborious, destructive and difficult to implement for monitoring purposes. Additionally, direct methods are only possible on a small scale. Consequently up-scaling errors are likely to occur. However, direct measurements are important as a calibration method for the indirect techniques. With indirect methods, LAI is derived from observations of another variable. These methods are faster, can be automated and are applicable for large spatial sampling.

Table 1: Overview of methods for in situ leaf area index determination (Jonckheere *et al.*, 2004).

Direct LAI measurements

- Leaf collection
- Leaf area determination techniques

Indirect LAI measurements

Indirect contact LAI measurement methods

- Inclined point quadrat
- Allometric techniques for forests

Indirect non-contact LAI measurement methods

- DEMON
 - Ceptometer
 - LAI-2000 canopy analyzer
 - TRAC (Tracing Radiation and Architecture of Canopies)
 - Hemispherical canopy photographs
 - LIDAR (Light Detection And Ranging)
-

Direct measurements include leaf collection combined with leaf area determination techniques. Leaves can be collected both in a harvesting manner by destructive sampling of a few representative trees only (the model tree method) or in a non-destructive manner using litter traps. From the collected leaves, the leaf area is determined with the planimetric technique which uses a scanning system or a video image analysis system, or with the gravimetric technique that correlates dry weight of the leaves to the leaf area (Jonckheere *et al.*, 2004).

Indirect measurements are divided in contact and non-contact methods. The inclined point quadrat method is a contact method where the canopy is pierced with a long thin needle under known elevation and azimuth angle and the number of canopy hits or contacts with the point quadrat is counted. The LAI can then be calculated using equations based on a radiation penetration model (Jonckheere *et al.*, 2004).

Another indirect contact method uses allometric techniques which rely on the relation of leaf area between another parameter of the tree carrying the leaf biomass, such as stem diameter, crown base height, etc.

The indirect non-contact methods include optical methods that provide a measurement of light transmission through the canopy from which canopy features can be derived with the help of an appropriate radiative transfer theory (Norman and Campbell, 1989; Jonckheere *et al.*, 2004). A range of instruments are available to determine LAI in plant canopies. Jonckheere *et al.* (2004) categorizes

them in two groups, whether they are based on gap fraction analysis or on gap size distribution analysis. The assessment of gap fraction and gap size data can be accomplished using different instruments, including DEMON, a ceptometer (the Sunfleck Ceptometer, Accupar-80), LAI-2000 canopy analyzer, TRAC and hemispherical canopy photography. Hemispherical photography is discussed in more detail further on. Forest structural parameters, including LAI, can also be assessed using an upward scanning, ground-based LIDAR system, although LIDAR is usually used as an airborne system (Strahler, 2008).

The indirect non-contact methods perform relatively accurately in broadleaf canopies with a horizontally continuous cover, but tend to underestimate the LAI in coniferous forests, forest canopies with significant foliar clumping and canopies with discrete crowns (Asner *et al.*, 2003).

Although not reported in the review of Jonckheere *et al.* (2004), LAI can also be estimated with remote sensing. Where other techniques are mostly limited to small-scale estimates, LAI can be assessed for whole forests and other large-scale systems using these methods. The estimation of LAI through remote sensing is generally based on empirical relationships between ground measured LAI and the observed spectral responses of the sensor used (Lee *et al.*, 2006). These spectral responses are usually represented by vegetation indices, and a statistical relation between multispectral reflectance and LAI is described through regression techniques (De Wulf, 1992). A multitude of vegetation indices are used for these empirical models, such as a normalized difference vegetation index (NDVI) and a simple ratio (De Wulf, 1992; Lee *et al.*, 2006). NDVI is a widely used index for the estimation of LAI for multiple biomes. However, for high values of LAI and thus for closed canopy systems the correlation between NDVI and LAI becomes less significant. This occurs from values of LAI higher than 3 (Lee *et al.*, 2006; Aguilar-Amuchastegui and Henobry, 2006). Aguilar-Amuchastegui and Henobry (2006) proposed the use of a wide dynamic range vegetation index (WDRVI), which is a generalization of the NDVI, for use with denser vegetation. As observed in the discussed studies in tropical forest in the next section, the MODIS LAI product is also commonly used.

Every method is subject to limitations, including sampling error for direct measurements and nonrandom leaf distribution and inclination for indirect methods. Specifically for the case of optical methods, complicating factors include leaf spatial distribution, leaf angle distribution and the contribution of nonphotosynthetically active elements (e.g. stems and branches) (Asner *et al.*, 2003).

Obviously many methods are available for determination of LAI and the choice of a particular method depends on the ease of use at a specific study site (Asner *et al.*, 2003). For example in tropical forests, research is often conducted in a protected reserve and a destructive sampling would therefore not be allowed. De Wasseige *et al.* (2003) pointed out that not all methods are adapted for the use in tropical forest ecosystems. LAI measurements using different techniques performed in tropical rainforests are reviewed in the next section.

2.3.2 Leaf area index measurements in tropical rainforests

The determination of LAI in tropical forest ecosystems is not straightforward, as the canopy structure is typically very complex and study sites are difficult to access (Clark *et al.*, 2008). The choice of methodology frequently depends on the ease of use in particular field conditions (Asner *et al.*, 2003).

Both the use of direct methods and indirect methods has been commonly reported, with the majority of the study sites being located in the Amazon basin.

Leaf collection has been obtained through destructive sampling (e.g. McWilliam *et al.*, 1993; Clark *et al.*, 2008) and with the non-destructive litter trap methodology (e.g. Roberts *et al.*, 1996; Juárez *et al.*, 2009).

McWilliam *et al.* (1993) determined the leaf area index and the above-ground biomass of a *terra firme* Amazonian rainforest by destructive sampling and found a mean LAI value of 5.7 ± 0.5 . Clark *et al.* (2008) also used destructive sampling with the difference that they measured on a landscape scale, respectively the first (according to the authors) direct landscape scale measurement of LAI in a tropical rainforest. Their study site was 515 ha of primary forest located in Costa Rica where they used a movable modular tower and stratified random sampling to collect all leaves in vertical transects from forest floor to the canopy top. With this strategy, it was possible to measure horizontal and vertical distribution of LAI and to assess LAI variation across environmental gradients. Additionally, the vertical distribution of LAI among plant functional groups was estimated, with the result that trees as a functional group (excluding palms) accounted for the largest part of the total LAI (LAI 3.29), followed by palms (LAI 1.33) and lianas (LAI 0.73). An overall mean LAI of 6.00 was estimated.

The direct method using litter traps has also been reported. For example in a study in central Amazon, Brazil, Roberts *et al.* (1996) estimated LAI values of 4.63 in Ji-Parana, 6.1 in Manaus and 5.38 ± 0.43 in Marabá using the litterfall methodology. Juárez *et al.* (2009) determined a litterfall based LAI of 5.45 in an Amazon forest site located in the Tapajós National Forest. Juárez *et al.* (2009) used both the litterfall methodology and the indirect hemispherical photography method. They determined a mean value of 5.70 ± 0.23 for LAI obtained with the hemispherical photographs, which produced only a 5% difference with the litterfall LAI estimate.

The technique of hemispherical canopy photography has been used in several other earlier studies of tropical forest. Trichon *et al.* (1998) used hemispherical photographs to identify spatial patterns in the tropical rainforest canopy. They investigated structural variability at a local (intra-site) and a regional (inter-site; tens of kilometers) scale. For this purpose, four primary forest sites in Central Sumatra, Indonesia, were investigated. Mean values of around 5 were found for the Plant area index (PAI). The term PAI is used since both leaves as well as stems and branches are included in the estimation.

Meir *et al.* (2000) used the technique of hemispherical photography to estimate LAI in two secondary forests. The first study site was located in the Mbalmayo Reserve in Cameroon in a semi-deciduous secondary forest with a mean canopy height of 36 m. Another site was at the Reserva Jarú in Brazil, which is an open tropical rainforest and has a canopy height of 35-45 m. From the images, an area-averaged mean value of 4.4 ± 0.2 for LAI was found for the site in Mbalmayo and 4.0 ± 0.1 for the site in Jarú. This research did not focus on the estimation of LAI, but LAI was determined in addition to leaf area density.

Vierling and Wessman (2000) also estimated the LAI using hemispherical photography in a tropical forest, namely in the Nouabalé-Ndoki National Park, in the Republic of Congo. Measurements were made in a monodominant *Gilbertiodendron dewevrei* tropical rainforest. The main objective of the

study was the characterization of the intensity and temporal heterogeneity of sunflecks. They measured photosynthetic photon flux density (PPFD) in the context of leaf photosynthesis and LAI in order to relate the PPFD regimes to leaf ecophysiology and canopy structure. They derived a mean total LAI of 7.2 at the site.

Malhado *et al.* (2009) provide a study on the seasonal dynamics of various leaf variables, namely LAI, leaf mortality, biomass, growth rate and residence time from 50 sample plots in a primary tropical forest site at Belterra, Pará State, Brazil. LAI measurements were taken using multiple LAI-2000 Plant Canopy Analyzers and an annual mean value of 5.07 ± 0.17 for LAI was estimated.

De Wasseige *et al.* (2003) used the LAI-2000 Plant Canopy Analyzer instrument in the tropical forest of Ngottot, in the Central African Republic. They determined a decrease in forest foliage during the dry season that occurs from December to February, with an accompanying seasonal variation of LAI of 0.34. The LAI ranged from 5.47 at the end of November to 5.13 at the end of February.

Brando *et al.* (2008) used a LI-COR 2000 Plant Canopy Analyzer in the Tapajós National Forest, Brazil and reported a mean value for LAI of approximately 5.9.

Remote sensing is also commonly used for the estimation of LAI. Myneni *et al.* (2007) investigated temporal LAI dynamics of the Amazon forest using remote sensing data. Data recorded continuously from 2002 until 2005 from the MODIS onboard the NASA Terra satellite was used to determine leaf area changes. A notable seasonality was observed, with an amplitude of 25% compared to the average annual LAI of 4.7. Doughty and Goulden (2008) also studied the seasonal pattern of LAI in evergreen tropical forests using satellite measurements (MODIS) combined with in situ measurements of the amount of PAR intercepted by the canopy (above and below canopy PPFD using PPFD sensors, LAI determined using a radiation transfer model). Their in situ LAI values increased from 6 to 10 in the period between August 2001 and March 2004, due to regrowth following logging. In comparison to related literature, these values are overestimated. According to Malhado *et al.* (2009), this overestimation could be a consequence of methodology using the whole PAR spectrum, including the green waveband with possible noise caused by radiation reflected by the leaves. The seasonal changes determined with MODIS differed from the in situ measurements but (although overestimated) Doughty and Goulden (2008) have more confidence in the in situ LAI measurements.

Clark *et al.* (2008) used the in situ measurements (discussed in the beginning of this section) to validate indirect estimates obtained with MODIS. Four pixels of 1 km² covered the study area and in each pixel, a median LAI value of 6.1 was found, very similar to the value of 6.0 found with the in situ measurements. They concluded that the MODIS algorithm works well for this type of forest.

As mentioned before, Scurlock *et al.* (2001) and Asner *et al.* (2003) reviewed and set up a database of LAI measurements reported from 1932 till 2000. For tropical evergreen broadleaf forests, a mean value of LAI of 4.8 ± 1.7 with a minimum of 1.5 and a maximum of 8.0 was reported, based on 60 published observations. Tropical evergreen broadleaf forest showed a high consistency based on the overall coefficient of variation. The results discussed above, also the ones obtained after 2000, are similar.

2.4 Canopy openness

Canopy openness (CO) is defined as the portion of the sky hemisphere that is not obscured by vegetation elements when viewed from a point. CO is a measure directly related to light regime and is therefore regularly linked to plant survival and growth. It can provide information on the growth conditions of seedlings, saplings and subdominant trees. CO is also frequently used to indirectly measure the amount of photosynthetically active radiation (PAR) available (Jennings *et al.*, 1999).

An old instrument for assessing CO is the 'moosehorn'. With this device the canopy is viewed through a transparent screen with an overlay of a marked grid of evenly spaced dots. The number of dots that overlap with the canopy are then counted by the recorder. More common is the spherical densitometer. This instrument consists of a convex or concave shaped mirror which is engraved with a grid. The curvature of the mirror allows a large area of the sky hemisphere to be reflected. The analyst assumes four equally spaced dots in each square of the grid and the dots intercepting with the reflection of the canopy are counted (Jennings *et al.*, 1999). Engelbrecht and Herz (2001) estimated light conditions in the understory of tropical forests, in a lowland forest in Panama, assessing the suitability of different indirect methods, namely hemispherical photography, LAI-2000 Plant Canopy Analyzer, 38-mm and 24-mm photographs and a spherical densitometer. The spherical densitometer, using CO as a measure of light, turned out to be the only one not highly correlated with the direct measurement.

Hemispherical photography provides the most complete measure of CO (Jennings *et al.*, 1999). Ostertag (1998) used hemispherical photography to estimate CO in a lowland rainforest in Costa Rica, this to assess belowground effects of canopy gaps. Percentage CO was 7.31 ± 1.82 in gaps and 3.90 ± 1.62 in the understory. Sterck and Bongers (2001) investigated crown development in a tropical rainforest in French Guiana and assessed the influence of tree height and light availability. CO was obtained using hemispherical photography and was used as an estimate of light availability. CO of individual trees smaller than 25 m ranged from 0.8% to 30%. For taller trees, a wide range was found, from 12% to 80%. Richards (1996) reported CO of 6% in closed lowland tropical rainforest at Danum (Sabah) found using hemispherical canopy photography.

2.5 Hemispherical canopy photography

This study determines LAI with hemispherical photography, a technique that employs a fisheye lens with a large angle of view, of up to 180 degrees. The technique can be used for the characterization of plant canopies, and is accomplished by taking photographs looking upward from below the canopy or looking downward from above the canopy (Rich, 1990). In this study, images are taken from below the canopy. From the hemispherical photographs, the determination of solar radiation penetration through canopy openings or the assessment of aspects of the canopy structure is possible, based on the measurements of the geometry of sky visibility and sky obstruction (Rich, 1990). The hemispherical photograph maps the size, magnitude and distribution of gaps in the canopy layer relative to the location where the image was taken (Jarčuška, 2008).

Different sampling strategies can be used, but normally the photographs are taken along a transect or in a grid pattern to sample spatial variability. The photographs can be repeated at exactly the same position over a period of time to determine dynamics and temporal variations. The formation

and closure of canopy gaps can be characterized and seasonal changes in foliage densities can be monitored (Rich, 1990).

Essentially, the hemispherical lens produces a projection of a hemisphere on a plane (Rich, 1990; Jonckheere *et al.*, 2004). A circular image is created with the zenith in the centre and the horizon on the edge. Each position on the image corresponds to a sky direction (Jonckheere *et al.*, 2004) and can be characterized by two variables: the zenith angle θ (the angle between the zenith and the sky direction) and the azimuth angle α (the angle measured counterclockwise between north and the compass direction of the sky direction) (Figure 2). It should be noted that the north and south are correctly positioned in the image, but east and west have switched places because of the upward view of the camera (Rich, 1990). The angular coordinates of openings in the canopy, as seen from the camera position, can thus be recorded. The nature of the projection depends on the geometry of the lens, which can be equidistant (polar or equiangular), orthographic, Lambert's equal area or stereographic equal angle (Jonckheere, 2007). Most commonly, the fisheye lens uses an equidistant projection (Jonckheere *et al.*, 2004), in which the zenith angle is proportional to the distance along a radial axis in the image (Rich, 1990). The projection of the lens also determines the accuracy of the results. Since there is always a slight deviation from the theoretical projection, a lens correction is necessary (Jonckheere *et al.*, 2005).

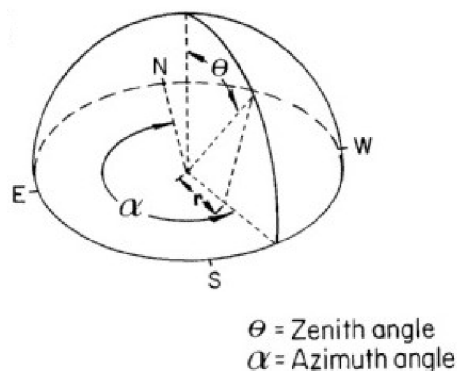


Figure 2: The projection as seen with a hemispherical lens looking upward. The hemispherical lens projects a hemisphere of directions on a plane. Each sky direction can be represented by unique angular coordinates, a zenith angle θ and an azimuth angle α (Rich, 1990).

The first hemispherical lens was created by Hill in 1924 for his study on cloud formation. Later on, forest ecologists optimized the technique to determine the light environment under forest canopies. In 1959, Evans and Coombe were the first to use this technique in an ecological framework when they estimated sunlight penetration through canopy openings by overlaying solar track diagrams on hemispherical canopy photographs (Rich, 1990). In 1967, Grubb and Whitmore were the first to use hemispherical photography in a tropical rainforest ecosystem when they compared the light reaching the forest floor of both a montane and a lowland site in Ecuador (Trichon *et al.*, 1998). The use of hemispherical photography and some results of LAI measurements in tropical rainforest were discussed in section 2.3.2.

In the following sections, the entire protocol of hemispherical canopy photography is discussed.

2.5.1 Image acquisition

There is no standardized field protocol for the acquisition of hemispherical photographs (Jonckheere *et al.*, 2004), but most researchers agree on acquisition procedures that minimize measurement errors. Amongst these are weather and light conditions, camera position and orientation, and exposure settings. Acquisition guidelines are provided and discussed by Jonckheere (2007). The camera is mounted on a tripod or telescopic monopod, levelled and oriented in such a way that the lens is oriented to the zenith and the camera itself is oriented to magnetic or to true north. Images are preferably acquired under overcast sky or under clear sky at sunrise or sunset. A clear sky can cause a strong contrast in brightness between zenith and horizon and also according to azimuth. Interference with the sun and light spots on leaves could cause problems during image analysis as these leaves could be misclassified as sky. Other weather conditions that have to be avoided are windy and rainy days.

A carefully exposed image is an important requirement for reliable results. Errors associated with exposure setting are discussed in section 2.5.3. The use of an underexposed image may be convenient (Jonckheere, 2007).

2.5.2 Image analysis

The four basic steps of image analysis are (Jonckheere, 2007):

1. Extraction of blue channel and field of view (FOV)
2. Thresholding
3. Determining gap fraction
4. Determining LAI

Several software packages are available for image analysis, including Gap Light Analyzer (GLA) from Gordon W. Frazer, WinPhot from Hans ter Steege, WinSCANOPY (Regent Instruments Inc., Quebec, Canada) and HemiView (Delta-T Devices Ltd, Cambridge, UK).

We start this section with the indices we want to derive from the images (steps 3 and 4), to clarify the goal of the image analysis. Next, the first to two steps are discussed.

2.5.2.1 Indices derived from hemispherical photographs

Before any other parameter can be derived from a hemispherical photograph, the gap fraction has to be determined. The obtained gap fraction data can then be used as input for inversion models to calculate structural canopy features (Norman and Campbell, 1989). Light extinction models rely on the strong relation between canopy structure and gap fraction and can provide estimates of LAI (Jonckheere *et al.*, 2004). Gap fraction is thus the crucial variable that needs to be determined for input in the models.

Gap fraction refers to the integrated value of the gap frequency over a given surface area, with the gap frequency being the probability that a radiation beam is not intercepted by a vegetation element before reaching the ground (Weiss *et al.*, 2004) and is determined as follows (Jonckheere *et al.*, 2004):

$$T(\vartheta, \alpha) = \frac{P_s}{P_s + P_{ns}} \quad (1)$$

where $T(\vartheta, \alpha)$ is the gap fraction as a function of a range of zenith angle ϑ and azimuth angle α , P_s is the fraction of sky visible in that region and P_{ns} is the fraction obstructed by vegetation in the same region.

The derivation of LAI now consists of the inversion of the gap fraction data using the Poisson model for gap frequencies (Weiss *et al.*, 2004),

$$\begin{aligned} P_0(\theta_v, \varphi_v) &= \exp(-N(\theta_v, \varphi_v)) \\ &= \exp\left(\frac{-G(\theta_v, \varphi_v)L}{\cos(\theta_v)}\right) \end{aligned} \quad (2)$$

with $P_0(\theta_v, \varphi_v)$ the gap fraction in direction (θ_v, φ_v) , the mean number of contacts $N(\theta_v, \varphi_v)$ between a light beam and a vegetation element, the projection function $G(\theta_v, \varphi_v)$ and LAI L . The Poisson model is based on a number of assumptions: canopy is closed, horizontally homogeneous, with vegetation elements randomly oriented with respect to azimuth, with a random spatial distribution within the canopy volume or deviating from randomness with a constant factor, small in size compared to the measurement area, and not transparent to solar radiation (Trichon *et al.*, 1998). Alternatively, when the assumption of random distribution is not satisfied, the gap fraction can be expressed as an exponential function of LAI (Weiss *et al.*, 2004):

$$P_0(\theta_v, \varphi_v) = \exp(-K(\theta_v, \varphi_v)L) \quad (3)$$

with $K(\theta_v, \varphi_v)$ the extinction coefficient.

When the gap fraction method (Norman and Campbell, 1989) is used in the analysis of hemispherical images, it is not possible to differentiate between photosynthetically active tissue and other plant elements including trunks and branches (Jonckheere *et al.*, 2004). This means that it is not exactly a leaf area index that is derived and other terms have been proposed and used, such as plant area index (PAI) (e.g. Trichon *et al.*, 1998) and vegetation area index (VAI) (e.g. Fassnacht *et al.*, 1994).

Optical methods also suffer from other inaccuracies, due to the canopy's deviation from the assumption of random distribution, defined as clumping, which leads to an underestimation of the derived LAI (Chen and Black, 1992; Bréda, 2003). Therefore a clumping index is introduced which describes the non-random distribution of the canopy elements (Black *et al.*, 1991; Trichon *et al.*, 1998). This clumping index equals 1 for a random canopy and is smaller than 1 for a clumped canopy. The index should be determined independently from the used method (Trichon *et al.*, 1998). Chen and Black (1992) introduced the operational term 'effective LAI' (L_e) for LAI estimates that were determined optically. According to Jonckheere *et al.* (2004), this term seems most appropriate because it recognizes that the inversion models are unable of measuring the surface area contributed solely by canopy elements, and that they cannot compensate for their non-random distribution.

The alternative terms for LAI (VAI, PAI, L_e) are not frequently used by most researchers and LAI remains the preferred parameter, as the relation to photosynthesis and other biophysical processes is more straightforward. The value PAI actually derived with optical methods can be transformed to

LAI with the help of a wood area index (WAI) and a clumping factor (C), both independently derived (Trichon *et al.*, 1998) (Juárez *et al.*, 2009):

$$PAI = C \cdot LAI + WAI \quad (4)$$

An even more accurate transformation should include an additional clumping factor for WAI (Juárez *et al.*, 2009). The estimation of the WAI however is rarely done. For the rainforest in a French Guiana site, Bonhomme *et al.* (1974) estimated that 7% of the total canopy elements are woody area. For the estimation of LAI in tropical rainforest, Juárez *et al.* (2009) even neglected the WAI (=0) and just expressed that the canopy was very dense. When ignored, a high woody portion will probably result in an overestimation of LAI (Trichon *et al.*, 1998).

2.5.2.2 Image preprocessing

Before proceeding with the actual analysis of the images, a preprocessing step is required. This includes a lens correction, the extraction of an appropriate channel, generally the blue channel, registration of the image and determination of FOV that will be used (Jonckheere, 2007). Editing and image enhancement techniques are available, but their use increases the processing time significantly and can introduce additional types of errors (Rich, 1990). Large tree trunks and other artefacts on the image can be masked before the actual image analysis.

The different channels of a colour image, red-green-blue (RGB), can be examined to determine which channel shows the best contrast between the sky and the vegetation. According to many researchers (e.g. Frazer *et al.*, 2001; Nobis and Hunziker, 2005), the blue channel performs best for the separation between sky and vegetation. The explanation for this is that the absorption by the canopy elements is maximal and scattering of sky is generally lowest in this blue channel (Jonckheere *et al.*, 2005). Choosing for the blue channel for the analysis can mean a trade-off with another factor, namely small vegetation elements might not be visible in the blue channel (Frazer *et al.*, 2001). Jonckheere *et al.* (2005) observed the same effect and concluded that for their images, the use of the entire spectral resolution showed more detail of the canopy, especially in sunlit areas.

2.5.2.3 Classification of images

One of the most critical steps in image processing is the thresholding step (Nobis and Hunziker, 2005; Jonckheere *et al.*, 2005), in which the image is transformed into a binary image. A classification is made between sky and vegetation elements. The method consists of selecting an optimum brightness value as a threshold, any pixel with a value above this threshold is classified as sky and at or below this value is classified as vegetation (Rich, 1990; Jonckheere *et al.*, 2005).

Determining a correct threshold is challenging and deviations of the true value have a significant influence on the subsequent calculations (Nobis and Hunziker, 2005). When the threshold is set too low, sky pixels will be overestimated resulting in a loss of foliage elements and an overestimation of the gap. Conversely, over-thresholding leads to underestimation of the gap fraction (Jonckheere *et al.*, 2005). Thresholding is a relatively simple and effective tool when there is a substantial difference between grey levels representing sky or vegetation (Sezgin and Sankur, 2004). However, this

condition is not always fulfilled and problems can occur due to uneven exposure, uneven reflectance within vegetation elements and background, and edges sampling effects (Rich, 1990). Edge sampling effects are due to mixed sky and foliage pixels at the edges, which lead to an intermediate grey value. This effect is minimized when working with high dynamic range digital imagery because the frequency of mixed pixels is much lower (Jonckheere *et al.*, 2005). Problems causing difficulties for thresholding are discussed in section 2.5.3.

In most software packages, thresholding is performed manually, based on visual interpretation by the operator. Obviously, this is an arbitrary and subjective way of determining the threshold value and several researchers have indicated manual thresholding as a source of inconsistency and errors (Rich, 1990; Frazer *et al.*, 2001; Jonckheere *et al.*, 2004; Nobis and Hunziker, 2005). Single manual thresholding can be improved by taking a mean manual threshold selected by one or multiple operators (Frazer *et al.*, 2001; Jonckheere *et al.*, 2005). Manual thresholding is also very time-consuming and thus not very practical when many images have to be processed (Jonckheere *et al.*, 2005). Recently, automatic thresholding techniques have received considerable interest, because they are objective, operator-independent and fast. Different automatic thresholding methods exist and can be categorized in 6 groups according to the information they use (Sezgin and Sankur, 2004; Jonckheere *et al.*, 2005):

- Histogram shape-based methods, analysing shape properties of the histogram including, peaks, valleys and curvatures.
- Clustering-based methods, based on clustering analysis where two clusters are defined as object and background.
- Entropy-based methods, using the entropy of background and foreground regions, the cross-entropy between original and binary image, etc. The maximization of entropy of the binary image should be indicative of maximal information transfer.
- Object attribute-based methods, selecting a threshold value similarity measure between the original and binary image, with attributes including edge matching, fuzzy shape similarity etc.
- Spatial methods using higher order probability distribution and/or correlation between pixels for thresholding.
- Local methods calculate a threshold at each pixel depending on local image characteristics such as range, variance etc.

Nobis and Hunziker (2005) presented an automatic thresholding method based on edge detection and Juárez *et al.* (2009) present an analysis of hemispherical images based on histogram analysis, in which they calculated an optimal threshold value using the entropy crossover method.

The method introduced by Juárez *et al.* (2009) is selected for this study since they tested their methodology in a tropical forest site in eastern Amazonia and obtained good results. The Nobis and Hunziker (2005) method is chosen since it is an automated thresholding method still including a visual control of the selected threshold. This yields a good basis of comparison of the thresholds selected with the Juárez *et al.* (2009) method, where the analysis of the images is conducted in batch mode without the possibility of visual control.

Automatic thresholding based on edge detection

Nobis and Hunziker (2005) presented an optimal threshold algorithm that calculates a threshold value that gives the highest local contrast at the edges between classified sky and vegetation elements.

The original image is first transformed into 255 new binary black and white images, using a different threshold value t (ranging from 0 to 254) for each transformation:

$$f(b, t) = \begin{cases} 1, & b > t \\ 0, & b \leq t \end{cases} \quad (5)$$

The thresholding is applied to a single channel of the RGB image, usually blue, setting brightness values b above t to 1 and below t to 0. On every newly transformed images, a 2 by 2 moving window is used to average the absolute differences of the corresponding brightness values b of the original image. This is only done for those pairs of pixels representing an edge in the transformed image, thus when the transformed pixels have different values. The optimal threshold value t_{opt} is defined as the threshold which has the maximum average brightness difference at the edges in the original images, defined as

$$t_{opt} = \arg \max_t (\text{mean}_S \{ |b_{x_1, y_1} - b_{x_2, y_2}| \mid f(b_{x_1, y_1}, t) \neq f(b_{x_2, y_2}, t) \}) \quad (6)$$

This automatic thresholding method is implemented in the software tool SideLook (shareware downloadable at <http://www.appleco.ch>), written by M. Nobis (2005).

Nobis and Hunziker (2005) tested the performance of their algorithm by comparing the results with results obtained with manual thresholding (single and mean). Data were collected in Switzerland under different forest canopy conditions. Both thresholding methods were evaluated by comparing the obtained threshold values, and the canopy openness and diffuse transmittance derived after thresholding. The calculated diffuse transmittance was also compared to the photosynthetic photon flux density (PPFD) measurements obtained separately. Their results showed that the actual threshold values determined with the different methods have large variations, but the calculated parameters show very high correlations.

Nobis and Hunziker (2005) concluded that the automatic threshold method based on edge detection could have advantages over manual thresholding. The automatic method is objective and reproducible and may improve the accuracy of the results. An additional advantage of this automatic method is that it is much less time-consuming and that it can be applied on a large set of images.

Optimal threshold value based on histogram analysis

Juárez *et al.* (2009) apply a thresholding method for determining LAI in Amazon forest in Brazil where the optimal thresholding value (OTV) was calculated with the entropy crossover method (ECOM) following Sahoo *et al.* (1997). Entropy is a statistical measure of randomness that can be used to characterize the texture of the image.

In a first step, the ECOM calculates an *a priori* entropy E of the image by:

$$E = - \sum_{i=100}^{255} p_i \log_2(p_i) \quad (7)$$

where p_i is the density function or the fraction of pixels with grey level i . Therefore, it is assumed that OTV will be found in the range of 100 and 255, based on an initial histogram analysis, simply to reduce processing time. After this, classes of black pixels (BP) and white pixels (WP) are separately defined and *a priori* entropies E_{BP} and E_{WP} are defined for both classes using a threshold value t by:

$$E_{BP} = - \sum_{i=100}^t \left(\frac{p_i}{p(BP)} \log_2 \frac{p_i}{p(BP)} \right) \quad \text{with} \quad p(BP) = \sum_{i=100}^t p_i \quad (8)$$

$$E_{WP} = - \sum_{i=t+1}^{255} \left(\frac{p_i}{p(WP)} \log_2 \frac{p_i}{p(WP)} \right) \quad \text{with} \quad p(WP) = \sum_{i=t+1}^{255} p_i \quad (9)$$

with

$$p(BP) + p(WP) = 1 \quad (10)$$

Finally, OTV is determined as the grey level where these two entropies are equal, constrained by the minimum of $(E_{BP} - E_{WP})^2$.

Once the OTV is determined, LAI is calculated with the gap fraction method described by Norman and Campbell (1989). Juárez *et al.* (2009) implemented this procedure in IDL. This software is available at ftp://lba.cptec.inpe.br/lba_archives/CD/CD-04/lai/gap_fraction/.

Juárez *et al.* (2009) validated the derived LAI against LAI measurements with the CI-100 device and LAI estimates from litterfall collection. A mean LAI value of 5.70 ± 0.23 was estimated from the hemispherical photographs, which was 5% higher than the litter-LAI, but 28% higher than the CI-LAI.

An important strength of this method is the possibility of analysing multiple images in batch mode, with an average time of 15 minutes for 100 images according to Juárez *et al.* (2009). A weakness of this batch mode analysis is the lack of a visual comparison between the original and binary image, to make sure that the thresholding is done realistically. Another weakness when studying the source code is the absence of a lens correction.

Another advantage is the possibility to make changes to the source code, since this is freely available. For example the incorporation of other parameters after the image classification is possible.

2.5.3 Sources of errors

Since hemispherical canopy photography involves many steps, errors can be introduced at multiple levels, listed in Table 2. Errors that can occur during image acquisition should be minimized by following a strict protocol. This includes errors introduced by camera alignment, settings and climate conditions, which can easily be avoided (Jonckheere, 2007). Frequently discussed sources of errors are exposure, thresholding and clumping. These are discussed below.

Table 2: Levels at which errors can be introduced in hemispherical photography (Jonckheere *et al.*, 2004).

Image acquisition
- Camera position
- Horizontal/vertical position
- Exposure
- Evenness of sky lighting
- Evenness of foliage lighting (reflections): direct sunlight
- Optical distortion
Image analysis
- Distinguishing foliage from canopy openings
- Assumed direct sunlight distribution
- Assumed diffuse skylight distribution
- Assumed surface of interception
- Image editing/enhancement
- Consideration of missing areas
Violation of model assumptions
- Assessment of G-function variations
- Leaf angle variability
- Consideration of clumping

Exposure settings have been identified as an important source of error by multiple researchers (e.g. Rich, 1990; Jonckheere *et al.*, 2005; Zhang *et al.*, 2005). Zhang *et al.* (2005) concluded that image acquisition using automatic exposure is not reliable. These images result in an overestimation of gap fractions for medium and high density canopies and consequently in an underestimation of effective LAI. The opposite result is obtained for open canopies. They developed a protocol for the determination of a suitable exposure using a built-in camera light meter. Generally, their procedure requires much shorter exposure than automatic exposure for closed canopies, and longer for open canopies.

As stated above, thresholding is one of the most critical steps in the image analysis. Thresholding can be very straightforward when the contrast between vegetation elements and sky is high, but problems often occur due to variable exposure and uneven reflectance within vegetation elements and the background. The selected threshold value can cause misclassifications, classifying reflections on leaves as sky and dark sky regions as vegetation elements. Additionally, small openings tend to be underestimated and large openings are overestimated (Rich, 1990).

Clumping of the leaves is one of the main problems when using the gap fraction models (Weiss *et al.*, 2004). Indirect methods generally result in an underestimation of LAI caused by the violation of the model assumption of random distribution of the leaves within the canopy (Bréda, 2003). The clumping index should be derived independently. A reliable instrument for its assessment is the TRAC (Tracing Radiation and Architecture of Canopies) instrument. The TRAC determines the clumping effect by measuring the canopy gap size distribution (Weiss *et al.*, 2004).

2.6 Spatial variability

Spatial statistics includes all statistics where the spatial locations of the data play a prominent role. Geostatistics are used in this study, since the locations of measurements are crucial for describing spatial variability. Geostatistics are historically an important instrument for mining engineers and is commonly used in geology (Matheron, 1963). Spatial statistics are also used to describe ecological systems. Some studies in tropical forests are discussed.

A common geostatistical tool is the variogram, representing the variance as a function of distance between sample locations. The variogram consists of three characteristics, namely the nugget, range and sill. The nugget is the estimate of the variance at distance 0. The range represents the distance at which the data is no longer autocorrelated and the sill represents the variance of the random field. The variogram is discussed in detail further on in the study. The parameters of the variogram can then be used for interpolation within the entire study area, based on measurements at sample locations. Interpolation is generally known as 'kriging' in geostatistics. Different variants of kriging exist and the appropriate one has to be determined for each study (Burrows *et al.*, 2002).

From comparative studies of structure and composition of tropical forests, it is clear that marked differences exist between forests in different geographic regions and climatic patterns. Less attention is paid to the structural variability of neighbouring sites, for example 1 to 100km separation. Differences in structure and composition on this small scale could be a consequence of changing soil conditions or elevations, or could be caused by disturbances in the past (Chapman *et al.*, 1997).

Chapman *et al.* (1997) examined spatial and temporal variability over a small scale in a moist evergreen forest in Uganda (Kibale National Park), transitional between lowland and montane forest. Size and densities of tree species are examined and compared between forest sites separated by less than 15km. They documented a significant difference in tree species composition among the different sites.

Wirth *et al.* (2001) studied spatial and temporal variability of canopy structure in a tropical moist semideciduous forest in Panama. LAI was estimated by an indirect approach based on the measured radiation interception and leaf angles and used as a parameter for canopy structure. Both vertical and horizontal spatial variability as the seasonal variability were examined. For the spatial analysis, kriging was used to interpolate the LAI measurements between grid points of a 0.21 ha plot. The created semivariograms were solely used for the creation of contour maps, the characteristics of the variograms were not further discussed. The horizontal distribution of LAI in the plot was described as widely ranging between 3 and 8, with a mean of 5.41.

Trichon *et al.* (1998) examined spatial patterns in the tropical rainforest structure in Central Sumatra, Indonesia. 1 ha plots were investigated, with measurements locations in a regular pattern with 10m intervals. Semivariograms were used for the detection of spatial patterns in LAI and CO. No significant dependency between adjacent measurements were found. Inter-site comparisons were made by comparing the difference of their means and the significance. They concluded that even within regions with the same bioclimate and a small altitude range, tropical rainforest exhibit a large structural variability.

3 Materials and methods

3.1 Study sites and sampling scheme

The fieldwork for this study took place in primary and transition tropical rainforest at different experimental sites near Kisangani, Democratic Republic of Congo (DRC). This is in the north eastern part of DRC, at 447 m above sea level. The average rainfall is high throughout the year, with an annual mean precipitation of 1728 mm. Two short dryer seasons occur respectively from December to February and from June to August, with an average precipitation of 60 mm for the driest month. The temperature is relatively constant throughout the year with a mean of 24.5 °C. The annual average relative humidity is also high, 82% (Nshimba, 2008).

To maximize the spatial range, hemispherical photographs were taken in different plots at different locations in the region of Kisangani. Exact locations of the study sites are the Man and Biosphere (MAB) reserve of Yangambi (N00°48'; E24°29'), and in the reserves of Yoko (N00°17'; E25°18') and Masako (N00°36'; E25°13') (Figure 3). Hemispherical photographs were taken in Yoko from July 19 until July 28 2010, in Yangambi between August 11 and August 17 2010 and in Masako between August 27 and September 4 2010, all in the drier season.

3.1.1 Yoko study site

In Yoko, three separate plots are examined. Two of these plots (YOK/II and YOK/III) are located within a permanent sample plot of 400 ha in primary forest, installed by the REAFOR project. This sample plot is divided in a 'bloc nord' and a 'bloc sud', each of 200 ha. Badjoko (2009) made an inventory of all emergent and dominant trees present in the south bloc. Emergent trees were defined as all trees with a height between 35 and 45m and dominant trees were trees with a height between 25 and 35m. Badjoko (2009) assessed different formations of vegetation within this permanent sample plot. The sample plots of this study are located in what Badjoko (2009) defines as monodominant forest of *Gilbertiodendron dewevrei* (De Wild.) and mixed forest. Abundant species include *Alstonia boonei* (De Wild.), *Celtis mildbraedii* (Engl.), *Copaifera mildbraedii* (Harms), *Entandrophragma candollei* (Harms), *Julbernardia seretii* (De Wild.) Troupin, *Pericopsis elata* (Harms) Van Meeuwen, *Piptadeniastrum africanum* (Hook.f.) Brenan, *Polyalthia suaveolens* (Engl. & Diels), *Prioria oxyphylla* (Harms) Breteler and *Pterocarpus soyauxii* (Taub.). The third sample plot in Yoko (YOK/I) is located outside of this permanent sample plot, but in a nearby part of the forest which (visually) resembles the other plots. The soils in Yoko are very similar as those in Yangambi (described below), with a clay content around 30 to 40% (Personal communication Geert Baert). The plots are at an altitude of around 470m.

The sample scheme determined *a priori* for this study had to be altered in the field. The initial plan was to sample the entire south bloc in a regular grid every 100m. In the field, the topography precluded this sample scheme and only the first 80 ha were sampled (YOK/III). Since another small plot was available outside this permanent sample plot (YOK/I), it was decided to change the strategy. In the larger permanent sample plot, this new sample scheme was also used (YOK/II).

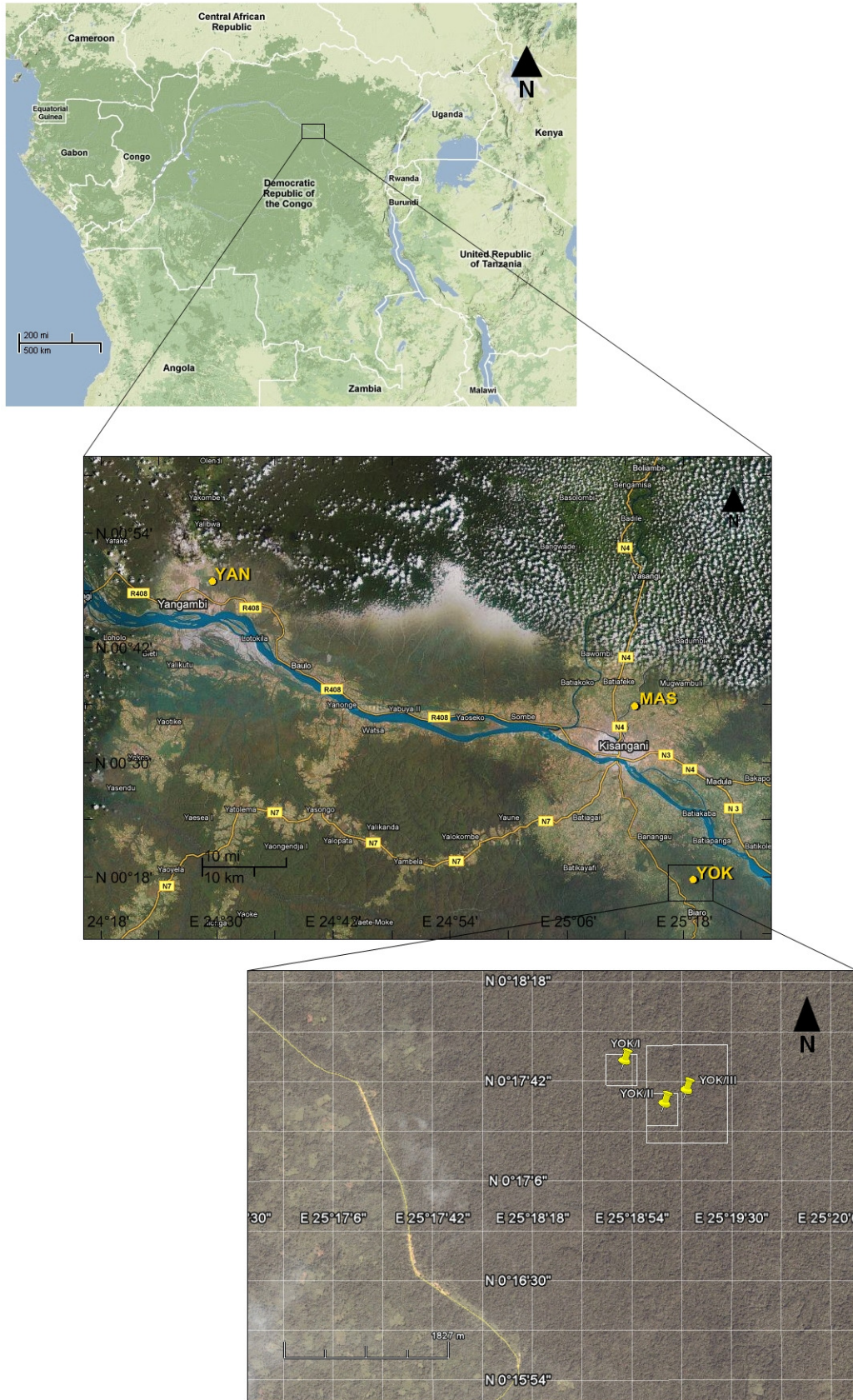


Figure 3: Maps with exact sample locations (Google Earth and Google Maps).

The two plots referred to as YOK/I (central coordinates: N00°17'46"; E25°18'50.1"; ±7m) and YOK/II (central coordinates: N00°17'30.6"; E25°19'4.5"; ±5m) are both plots of 9 ha. Images were collected in a 300 m by 300 m regular grid, with nodes every 25 m (Figure 4a). The larger plot of 80 ha (YOK/III; central coordinates: N00°17'35.4"; E25°19'12.4"; ±8m), in the permanent plot, was sampled in a predetermined manner. Images were taken in a regular grid of 800 m by 1000m with nodes every 100 m (Figure 4b). Images could not be collected in the north eastern corner of this grid due to difficulties in reaching the measurement locations (transect G-I, from 700 m until 1000 m). Note that YOK/II lies in this larger plot YOK/III (darker square in Figure 4b). From YOK/III, images taken in standard exposure setting of transect A, at 0 and 100m are lost.

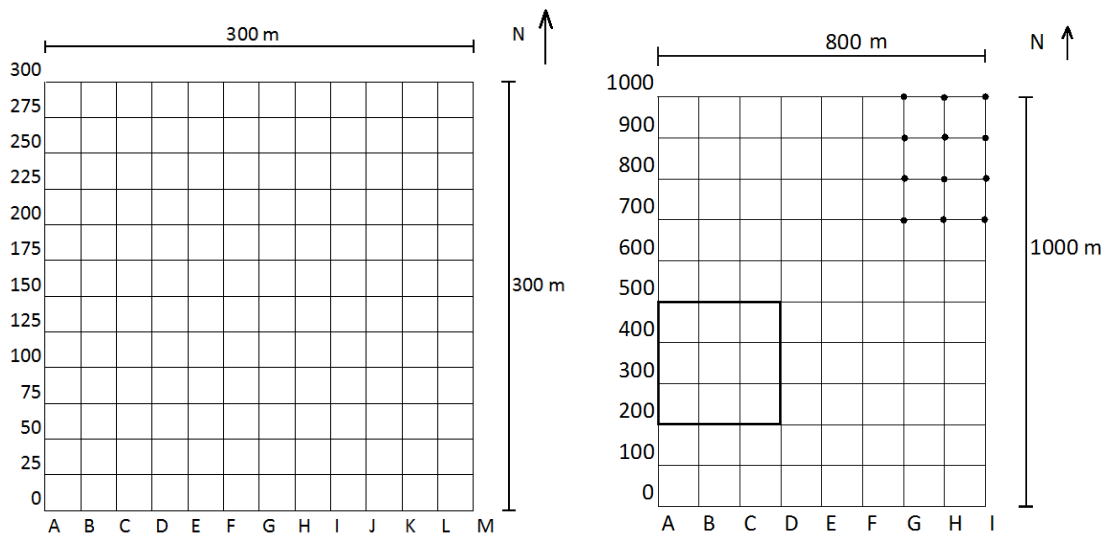


Figure 4: a) Regular grid sampling of 9 ha plot. Hemispherical images were taken at every node. YOK/I, YOK/II and YAN/I were sampled in this manner. b) Regular grid sampling of 80 ha plot. Hemispherical images were taken at every node. Measurement locations where no sampling was possible are indicated by dots. YOK/III was sampled in this manner. The position of YOK/II is indicated by the black border.

Additionally, in an experimental site in transition forest in Yoko, clearcut experiments were performed in July 2010 (Buggenhout, 2011). All leaves were collected and weighed from circular plots with radius 7 m. Subsamples were taken from which wet and dry weight and leaf area were determined. Photographs were taken in the direct neighbourhood of these plots (YOK/2010/1, YOK/2010/2 and YOK/2010/4; detailed description: Buggenhout, 2011), for comparison of obtained data. Photographs could not be acquired prior to the clearcut experiments, because the other students started their fieldwork earlier. Note that leaves of lianas were not included in leaf collection.

3.1.2 Yangambi study site

The reserve of Yangambi is characterized by different vegetation types. In order of magnitude, these formations are old transition forest, semideciduous dense forest, young transition forest, evergreen dense forest, a mosaic of agricultural land, experimental agricultural parcels and houses, a mosaic of fallow shrubs and herbs and swamp forest (Toirambe, 2010).

The sample plot in Yangambi (YAN/I) is located in semideciduous dense forest (Gilson *et al.*, 1956) characterized by the presence of deciduous species losing their leaves in the dry season, in combination with evergreen species. Representative species of these forests are *Prioria oxyphylla* (Harms) Breteler, *Prioria balsamifera* (Vermeesen) Breteler, *Pericopsis elata*, *Cola griseiflora* (De Wild.), etc. (Toirambe, 2010). An inventory at the exact location of the sample plot is not made.

The soils of the plateau of Yangambi consist mainly of eolian sediment, composed mostly of quartz sand, kaolinite clay and more or less hydrated iron oxides (Gilson *et al.*, 1956). The sample plot lies in the series of Y1 as defined by Gilson *et al.* (1956). Soils in this series are latosols developed in the undisturbed eolian deposit of Yangambi. The soil has a clay content of 30 to 40 % and features a reddish colour. The existence of the B-horizon is common.

The plot in Yangambi (YAN/I; altitude 450m; central coordinates: N00°48'54.1"; E24°29'34.2"; ±5m), 9 ha large, was investigated in exactly the same way as YOK/I and YOK/II (Figure 4a). In a smaller area of 1 ha inside this plot (south western corner, transects A-E, each transect until 100 m), image acquisition was repeated at the same measurement locations, but in different/sunnier weather conditions. This was meant to determine the influence of different weather conditions on the parameters derived from hemispherical images. This area located inside YAN/I is referred to as YAN/II.

In Yangambi, additional hemispherical images were taken in two plantations of *Gilbertiodendron dewevrei* and *Pericopsis elata*, species that are common in primary tropical rainforest. Hence species specific LAI could be derived. In these plantations, 3 positions for sampling were chosen randomly on site, with a minimum of 15 m between measurement locations. The plantations themselves are small (around 100 m by 100 m). This has to be taken in mind for image analysis, because the edges of the images contain other species. The zenith angle appropriate for analysis will depend on the occurrence of other species at the edges of the images.

3.1.3 Masako study site

In Masako, photographs were taken during clearcut experiments (Buggenhout, 2011). Two sites were selected, one in a young transition forest (MAS/2010/1) and one in an old transition forest (MAS/2010/2) (detailed description: Buggenhout, 2011). All trees in both plots with a radius of 7 m were systematically cut down and sampled in the same manner as in the clearcut experiments in Yoko. An initial photograph was taken in the centre of the plot. Subsequently, an image was taken after every tree was cut down. Sometimes a couple of trees were taken down due to the connection of lianas, before a photograph could be taken. For comparison additional images were taken in the direct neighbourhood of the plots.

3.1.4 Site comparison

All the plots of 9 ha in primary forest, both in Yangambi as in Yoko, were (visually) quite similar to each other with respect to amount of understory, tree size, appearance, etc. Additionally, the soils of the areas are similar (personal communication Geert Baert). The topography in the plot of 80 ha in Yoko was different, with occurrence of valleys in the north of the plot.

The plots in the transition forest in Yoko were very similar to each other, with similar species and presumably the same soils conditions. They were very close together (maximum 100m apart). The plots were representative for the surrounding forest. A considerable amount of understory was present.

In Masako, the two selected plots in transition forest were slightly different. MAS/2010/1 resembled the plots in Yoko, while MAS/2010/2 was selected in an older, more mature forest. For the clearcut experiment in Masako, it was not allowed to cut large trees. A plot with this condition was selected, but the surrounding forest also contained larger trees. Less understory was present in MAS/2010/2.

3.2 Data acquisition

With the goal of assessing structural parameters of the canopy, LAI and CO, hemispherical photographs were acquired using a Sigma 4.5mm f/2.8 EX DC HSM Circular Fisheye (equisolid-angle projection) mounted on a Nikon D300 camera. Images were taken looking upward with a full 180° angle of view. The camera was fixed on a tripod (Manfrotto) with adjustable ball-head (Manfrotto 498RC2), 1 m above the ground, levelled with a bubble spirit level fixed to the camera and oriented to magnetic north. Images were recorded with a high resolution of 4288 x 2848 pixels, associated with the 'fine' setting on the camera and with an ISO set at 200. Understory present in the direct neighbourhood (up to 1.5m) of the measurement location was cut down. At each measurement location, 6 photographs were taken, 3 with automatic exposure values (referred to as standard exposure value) and 3 pictures that were underexposed at exposure value -3.0 (e.g. Figure 5) (personal communication, Inge Jonckheere). For each measurement location, the derived parameters of the 3 images after analysis are averaged and a single value is assigned.

Data was collected under overcast sky conditions to avoid overexposure and to reduce sun reflections. The time of day when photographs were taken varied between 8:00 a.m. and 18:00 p.m.

The coordinates of every measurement location were taken using a handheld GPS, Garmin E-Trex. The accuracy of the assigned coordinates under the dense canopy was on average 7m, and varied between 3m and 17m.



Figure 5: Example of hemispherical photograph (image from plot YAN/I, primary forest). Top: image acquired using standard exposure setting; Bottom: underexposed image.

3.2.1 Weather conditions

Most researchers agree that images have to be acquired early or late in the day or under even overcast conditions. In tropical rainforests, little light reaches the ground (only 5%) due to the high biomass content (Trichon *et al.*, 1998). The question could be asked if weather conditions are important to acquire images under these closed canopies. This is tested in Yangambi, where YAN/I is taken in overcast weather conditions and YAN/II is taken 5 days later at the exact same location, but under a clear sky. Paired t-test is used to compare the images.

3.2.2 Direct measurements as validation

Data collected from the clearcut experiments in the transition forests in Yoko and Masako will be used for validation of parameters derived from the hemispherical photographs. The selected plots are YOK/2010/1, YOK/2010/2, YOK/2010/4, MAS/2010/1 and MAS/2010/2. These plots were representative for the surrounding forest.

Buggenhout (2011) determined the wet weight of the entire canopy, dry and wet weight of representative subsamples and the specific leaf area (SLA) (m^2/g dry weight) for every single tree in the plot. Combining these parameters gives the total leaf area of each tree. Since we know the ground area of the sampling plots (7m radius), the summation of the projected total leaf areas divided by the total ground area produces an overall LAI of the sampling plot. The term 'direct LAI' is used, referring to the applied methodology.

A problem occurred with a couple of trees, where the leaves were rotten and further analysis was stopped. The SLA for these trees were regarded as outliers, and was not calculated. Exclusion of the projected areas of these trees would underestimate the LAI of the sampling plot. Since SLA of different individuals within a single tree species was very similar, this SLA was used for trees with missing data. If the same species was located in the same plot, their SLA was used. If not, the SLA of the same species in neighbouring plots was used.

3.3 Data processing

All LAI values obtained from hemispherical photographs in this study are effective values, i.e., stems and branches are included in the LAI and clumping effects are not taken into account. The true LAI values will deviate from this effective LAI, but could be derived if a WAI and clumping factor are determined. This assessment is not made in this study.

The effective LAI in this study is referred to as ' L_e '. Between brackets, auxiliary information is given:

- Zenith angle used for analysis (in degrees)
- Exposure setting: standard (st) or underexposed (ue)
- Measurement plot

For example $L_e(75^\circ, \text{ue}, \text{YOK/I})$.

3.3.1 Channel selection

First, the decision has to be made what channels of the RGB images will be used for further analysis. To determine to channel best suited for analysis, each channel – blue, green and red – of a selection of images is separately analysed using the ECOM discussed below (section 3.3.2). The selected threshold and the structural parameters derived from the images are compared with a paired t-test.

For the selection of images, 4 measurement locations (6 images per measurement location) are selected from every plot in primary forest and 4 locations in total in the transition forests. The locations are selected over a range of less dense canopy over middle dense until very dense canopy, based on a visual comparison of the images.

Ultimately, the blue channel is selected for the analysis of the images (see results). The extraction of the blue channel is possible in each software program discussed below.

3.3.2 Selected thresholding methods

As previously discussed in the literature review, the conversion of a photograph into a binary image is a crucial step in the image analysis and has a large influence on the calculation of parameters from the images. Three thresholding methods are compared and the influence of the selected threshold on the final parameters is assessed.

The following three thresholding methods are tested (see literature review, section 2.5.2.3),

- Manual thresholding, using Gap Light Analyzer (GLA) (Frazer *et al.*, 1999)
- Edge detection, using SideLook (Nobis and Hunziker, 2005)
- Histogram analysis based on entropy crossover method (ECOM), using Matlab (based on Juárez *et al.*, 2009).

A selection of images is made to compare the different methods. This selection is based on their measurement location. Images taken on a location or in the direct neighbourhood of a location where clearcut experiments were performed and direct LAI is derived, are selected (Buggenhout, 2011). These plots are referred to as YOK/2010/1, YOK/2010/2, YOK/2010/4, MAS/2010/1 and MAS/2010/2. In total, 18 measurement locations (108 images) are selected.

It should be noted that the thresholding method using the ECOM in Matlab is already selected as the software that will be used for the final analysis of the images, independent of the results of this survey. The selection is based on the ability of analysing the images in batch mode. This was necessary due to the large amount of images that needed to be analysed (around 4500 images) and the limited time available for processing. The comparison with the other methods, manual thresholding and edge detection, is still made to assess the performance of the software. A paired t-test is used to compare the selected threshold of each image and to compare the derived parameters.

Manual

In manual thresholding, a visual comparison is made between the original image and the binary image. The analyst interactively adjusts the working binary image by changing the threshold value until it best resembles the original image. This threshold is set and a final binary image is produced. This is done in the program GLA (downloadable at <http://www.ecostudies.org/gla/>; Frazer *et al.*, 1999). After the image classification, the canopy structure data ($L_e(60^\circ)$, $L_e(75^\circ)$ and CO) are also computed in GLA.

Since manual thresholding is the only subjective method, a replication of this analysis is made by the same analyst (only for YOK/2010/1 and YOK/2010/2, 45 images) for the purpose to assess the consequences of single manual thresholding. For the comparison of the thresholding methods, the thresholds and derived parameters from single manual thresholding are used.

Edge detection

The edge detection thresholding method is an automated method implemented in SideLook (shareware downloadable at <http://www.appleco.ch>), written by M. Nobis (2005). All threshold values between 0 and 255 are tested and new images are produced. On these transformed images, the positions of the edges are detected and a 2 by 2 moving window is used to average the absolute differences of the corresponding original brightness values b on these positions. The optimal threshold value is defined as the threshold which has the maximum average brightness difference at the edges in the original images (Nobis and Hunziker, 2005). The analyst can then decide if the selected threshold is adequate, based on visual comparison with the original image. In case the absolute maximum is not appropriate, local maxima can be tested which are detected within a window of ± 20 threshold units.

Computing canopy structure parameters is not possible in SideLook. The binary image has to be saved for analysis in other software tools. In this study, the images are further analysed in GLA.

Histogram analysis based on entropy crossover method

Juárez *et al.* (2009) combined a thresholding method introduced by Sahoo *et al.* (1997) and the gap fraction method (Norman and Campbell, 1989) for the calculation of LAI. This combination was written as IDL software and is available at ftp://lba.cptec.inpe.br/lba_archives/CD/CD-04/lai/gap_fraction/. This software makes it possible to analyse the images in batch mode, which is a major advantages as there is a large amount of images to be analysed.

This software, originally written in IDL– 6.0 is rewritten in Matlab, version 7.8.0 (R2009a), available in Appendix 2. Slight changes are made in the script as described below.

First, a new function DIRR (Maximilien Chaumon 2009, available at <http://www.mathworks.com/matlabcentral/fileexchange/8682-dirr-find-files-recursively-filtering-name-date-or-bytes>) is used to filter all the JPG files in the directory, which makes it possible to work in batch mode.

Then the image has to be registered in which the circular extent of the hemispherical images is recognized. Therefore the square in which the circle is situated, the effective area of the hemispherical image, has to be defined. The same registration pixels selected for the registration in GLA are used. The description of the circle is done using the function MidpointCircle (created by Peter Bone, available at <http://www.mathworks.com/matlabcentral/fileexchange/authors/22116>). This function draws a circle in a matrix using the integer midpoint circle algorithm. The function is slightly rewritten so that also segments of the circle can be described.

Next the histogram of the circle is computed, which is the basis of the thresholding method. The threshold selection is based on minimizing the difference between entropies of the object and the background distributions of the histogram (Sahoo *et al.*, 1997). Therefore the following equations are used. First the *a priori* entropy E of the image is calculated by (Juárez *et al.*, 2009):

$$E = -\sum_{i=20}^{255} p_i \log_2(p_i) \quad (11)$$

with p_i is the density function.

Next, every threshold t from 20 to 255 is tested and classes of black pixels (BP) and white pixels (WP) are separately defined. *A priori* entropies E_{BP} and E_{WP} are defined for both classes subsequently using the different threshold values:

$$E_{BP} = -\sum_{i=20}^t \left(\frac{p_i}{p(BP)} \log_2 \frac{p_i}{p(BP)} \right) \quad \text{with } p(BP) = \sum_{i=20}^t p_i \quad (12)$$

$$E_{WP} = -\sum_{i=t+1}^{255} \left(\frac{p_i}{p(WP)} \log_2 \frac{p_i}{p(WP)} \right) \quad \text{with } p(WP) = \sum_{i=t+1}^{255} p_i \quad (13)$$

Finally, the optimal threshold is selected as the grey level where these two entropies are equal, restricted by the minimum of $(E_{BP} - E_{WP})^2$. In the Matlab software, these equations are included using the function Entropy.

Note that in the software the histogram and the threshold selection start at brightness value 20. Histograms were initially computed from 0 to 255, but this resulted in errors for a few images. Thresholds below 15 were sometimes found, which are not realistic thresholds to distinguish sky from vegetation elements. Since the cause of the problem could not be identified, a robust solution was used to solve this problem. The histograms are computed starting from threshold value 20.

For the calculation of LAI, Juárez *et al.* (2009) used the gap fraction method (Norman and Campbell, 1989). The gap fraction is calculated for multiple angular rings on a pixel by pixel basis as white pixels over total pixels. These gap data are then used in a gap fraction radiative transfer inversion model to calculate L_e . Juárez *et al.* (2009) only utilized the angular rings extending to a zenith angle of 75° for the calculation of L_e , to be compatible with a CI-110 device. The Matlab software was expanded to include other canopy structure parameters, namely L_e using angular rings extending to 60° zenith angle and the CO using the entire image (90° zenith angle). The CO is simply the total gap fraction of the circle. These parameters were chosen for the compatibility with the parameters calculated with GLA. $L_e(60^\circ)$ is calculated in a separate script. Thus from all images, the parameters $L_e(60^\circ)$, $L_e(75^\circ)$ and CO are derived, except for the plantations where only $L_e(60^\circ)$ is calculated, due to the occurrence of other tree species at the edges of the image.

Practically, the following equations are used to determine L_e from the gap fraction, described by Norman and Campbell (1989) (Juárez *et al.*, 2009). The transmitted fraction (T) of a beam of radiation in a canopy is described by the Lambert-Beer equation as

$$T(z_i) = \exp\left(-\frac{K_{ij}(z_i, \alpha) \cdot PAI}{\cos(z_i)}\right) \quad (14)$$

where K_{ij} is the extinction coefficient at a zenith angle z_i for a class of leaves j with inclination angle α and with PAI the effective plant area index.

The elements in the canopy are assumed to be randomly distributed. The extinction coefficient is defined by a generalized ellipsoidal leaf angle distribution model as

$$K_i = \frac{\sqrt{x^2 + \tan^2 \theta_i}}{x + 1.774(x + 1.182)^{-0.733}} \quad (15)$$

with θ_i the solar zenith angle. In this equation, x is the sole parameter that determines the shape of the distribution. Equation 14 is solved for PAI and x using nonlinear least-square regression technique.

PAI is expressed as

$$PAI = C \cdot LAI + WAI \quad (16)$$

where C is the clumping factor and WAI is the wood area index. The nonlinear least-square regression looks for values of x that produce a reasonable fit to the input data of $T(z_i)$. Norman and Campbell (1989) reported that when the input data is inconsistent or contains too much error, large values of x are needed to avoid a negative LAI. Juárez *et al.* (2009) included the calculation of a mean square error (MSE) between the transmitted light fraction optimized by the bisection method (T_{pred}), and the transmitted light fraction measured over the different annulus (T_{meas}). They found that large constraints of x produce a MSE larger than one and produce discontinuities in the LAI vs. grey level curve. They used the MSE as a simple metric to accept or reject the calculated LAI. LAI was rejected when MSE was larger than or equal to one.

An important remark has to be made on the extinction coefficient, namely that the empirical values utilized have not been validated. These values should be determined from extinction tests by measuring light at different stages in the canopy. Since Juárez *et al.* (2009) also worked in a tropical rainforest, namely in an Amazon forest site located in the Tapajós National Forest, the empirical values have been adopted in this study. This is an important assumption and will be discussed in section 5.1.1.

In Equation 16, the PAI is what we defined as L_e . Juárez *et al.* (2009) included a C and a WAI to derive the LAI. Since the values of C and WAI are not accurately known in this study, C is set to 1 and WAI to 0. If the values are accurately known, they can be easily set in the script and LAI can be determined.

The saturation level of L_e is assessed by analysing a completely black circle.

Lens correction was not included in the IDL software of Juárez *et al.* (2009). This was implemented in the Matlab software for the lens used in this study, as described in the next section.

3.3.3 Lens calibration

The used fisheye lens (Sigma 4.5mm f/2.8 EX DC HSM Circular Fisheye) has an equisolid-angle projection, also known as an equal-area projection,

$$R = 2f \cdot \sin \frac{\theta}{2} \quad (17)$$

with R the image radius, f the principle distance and θ the incidence angle. With this kind of projection, the ratio of the incident solid angle and the resulting area on the image is constant. This lens is suited for cover area measurements (Schneider *et al.*, 2009).

The images have to be corrected for lens distortions so that they can be used for photogrammetric purposes. According to Schneider *et al.* (2009), it is sufficient to correct for radial symmetric lens distortion to achieve a high accuracy. This radial symmetric distortion causes the edges of the image to be compressed and consequently cause these areas to be smaller and underestimated in area analysis.

In Gap Light Analyzer, the lens correction was implemented by simply inserting the calibration data. In Figure 6, it can be seen that the segments on the edges are more compressed when the distortion data is included. This same methodology of including distortion parameters was used in the Matlab script, where the outer segments are more compressed. Calibration data for this specific lens was supplied by the Sigma Corporation (Appendix 1).

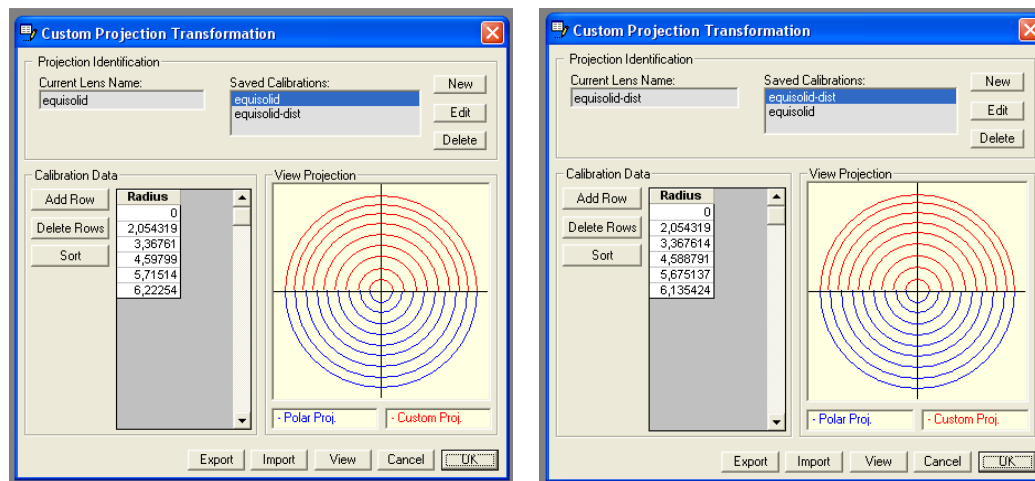


Figure 6: Projection transformation in GLA. Left: Equisolid-angle projection without distortion correction; Right: Equisolid-angle projection with distortion projection.

3.4 Spatial variability

The sampling scheme and the locations of the different plots (Figures 3 and 4) can provide information on spatial variability. Recall that YOK/I and YOK/II are both plots of 9 ha, and the plots are not far apart (645 m). The forest type did not change over this distance and soil is comparable in both plots. Comparison of these plots will give us an idea of local variations in canopy structure. YOK/III is a plot of 80 ha with sampling distances of 100 m and YOK/II is part of this plot with sampling distances of 25 m. This will give us an idea of sampling scale variations. A comparison

between YAN/I, YOK/I and YOK/II gives an idea of large scale variations and the possibility of extrapolating measurements over a larger scale, since the distance between the plots in Yoko and Yangambi is 108 km.

Means of the plots are compared. First a one-way ANOVA model is calculated with the different locations (plots) as factor variables. Then Tukey's HSD (Honestly Significant Difference) test is performed to find which means of the plots are significantly different from each other.

3.4.1 Geostatistics

In geostatistics, the spatial variability is modelled in function of the distance between measurement locations. In general, locations that are closely together are more similar to each other and thus more correlated than locations that are further on (Burrows *et al.*, 2002). This is graphically represented by a variogram (Figure 7), which is a summarizing tool that is very helpful in the interpretation of the structure of the spatial variability. This variogram $\gamma(h)$ represents variance as a function of the distance between sample locations, defined as (Burrows *et al.*, 2002),

$$\gamma(h) = \frac{1}{2N(h)} \sum_{N(h)} \{z_i - z_j\}^2 \quad (18)$$

with $N(h)$ the number of pairs of observations separated by the distance vector h and z_i and z_j observations at locations i and j , such that the distance between i and j equals h . The distance between sample locations, h , will be referred to as lags.

First an experimental variogram is calculated, which is a plot of $\gamma(h)$ values versus h (Figure 7). Then a theoretical variogram model is fit to this experimental variogram resulting in a continuous function. This variogram can be modelled using different generalized equations, e.g. spherical, exponential, Gaussian and linear equations. It is the characteristics of the fitted theoretical variogram model that are important for the interpretation of the structure of the spatial variability and these characteristics are also the basis for the subsequent interpolation. The first characteristic is the nugget effect, which is the estimate of the variance at a distance $h = 0$. In theory, the variogram would be zero at this distance, but in practice there is a minimal distance between the two nearest locations and the model needs to be extrapolated to distance $h = 0$. The intercept on the Y-axis is called the nugget effect. The second characteristic is the sill, which represents the variance of the random field (study area as a whole). The third characteristic is the range, the distance where the data are no longer related. It is the lag at which the sill is reached (Burrows *et al.*, 2002).

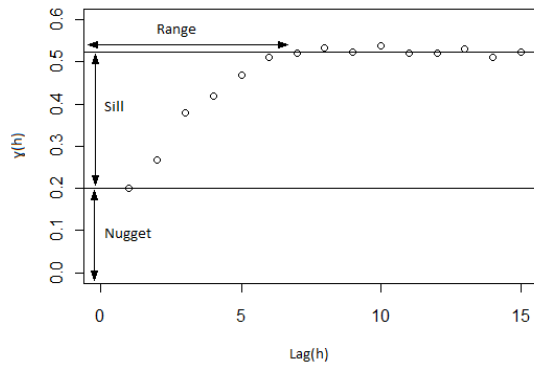


Figure 7: The variogram and its characteristics.

The theoretical variogram model can then be used for kriging. The interpolation is conducted by taking the local information from each measurement location and by applying it to the entire plot based on the variogram model. A map is produced that predicts the values of the variable over the entire study area (Burrows *et al.*, 2002).

Ordinary kriging is selected in this study, calculated as (Martinez *et al.*, 2010):

$$Z^*(x_0) = \sum_{\alpha=1}^{n(x_0)} \lambda_{\alpha} Z(x_{\alpha}) \quad (19)$$

Practically, four steps are followed to investigate spatial variability and for the graphical representation:

- Maps with sample locations and values (Location maps)
- Experimental variogram
- Theoretical variogram modelling
- Ordinary kriging

Since the accuracy of the GPS varied considerably, the measurement locations seemed to be randomly dispersed in the plot. On the ground, every measurement location was accurately determined along parallel transects and measured with 25m between every measurement location of the 9ha plots and 100m for the 80ha plot. For the generation of the location and kriging maps, a regular grid is created without the actual coordinates, but simply showing the sampled transects. Every observation is located in this grid as is measured on the ground.

From the display of the location maps and from some preliminary test, no anisotropy is detected. The directions in which observations are located versus each other will not be considered during the calculation of the variograms. The variograms are therefore omnidirectional and the spatial variability is isotropic.

For the calculation of the experimental variogram, different combinations of number of lags and lag distances are tested and one is selected. The maximal lag distance never exceeds half the maximal distance of the study area. This was to avoid that only the observations near the edges are available for calculating the variogram. Additionally, the minimum number of lags is set at 10.

Next, a set of possible theoretical variogram models are fitted to this experimental variogram. Not all functions are suitable for modelling the variogram. After some preliminary tests, the spherical and the exponential type seemed to fit the data best. Multiple models were fitted using different combinations of the nugget effect, sill, range and type of model. This step is the most interactive and subjective step, and the different models have to be compared. Cross validation is used for the selection of the model that best fits the data and for assessing the performance of the model that is selected. In cross validation, every observation from the data set is separately removed and estimated using the remaining data and the specified variogram model. Since we know the observed value at the specified location, the interpolation error is calculated as

$$\text{residual} = \text{estimated value} - \text{observed value} \quad (20)$$

The mean square estimation error (MSEE) and mean absolute estimation error (MAEE) are then used to evaluate the performance of the interpolation method.

In the last step, the selected variogram model is used as input for ordinary kriging. The interpolation grid, and its resolution, has to be specified. For the visualization of the kriging map, a resolution of 5m is chosen which results in an easily interpretable map. Note that inaccuracies are introduced due to this resolution, since measurements are only made every 25m.

Kriging is not applicable when there are less than 100 measurement locations available. This means that the interpolation of YOK/III as is, is not possible. Since the plot YOK/II is located in YOK/III, these data are added to the data of YOK/III. To avoid confusion with the separate plots, the combination of the two plots is referred to as YOK/II/III.

When kriging is used, it is assumed that the regionalized variable is acquired without uncertainty. This is not the case. It is not possible to include the uncertainty in the interpolation. This has to be kept in mind when examining the results.

For the calculation of the experimental variogram and the fitting of multiple variogram models, the Stanford Geostatistical Modeling Software (SGeMS) is used (open-source package available at <http://sgems.sourceforge.net/>). The software has a GUI and the fitting of the variogram models is very easily done visually. Since cross validation is not possible in SGeMS, the following steps are continued with the program Surfer (Golden Software, CO, USA).

4 Results

Before showing detailed results in the following sections, an overview of the parameter effective leaf area index $L_e(60^\circ, ue)$ for the different forest types at the different locations is provided (Figure 8). These results show a slightly higher estimate in primary forest than in transition forest. The mean of L_e for the two plantations are lower than those in primary forests and in transition forests.

On average a relative standard deviation of 3% is found for L_e and 5.5% for CO, based on the three images acquired at one measurement location. Saturation of L_e is found at a value of 12.5 using ECOM analysis. All obtained values are well below this value.

In this results section, we will first show the results and impacts concerning image acquisition and analysis and next the results on spatial variation.

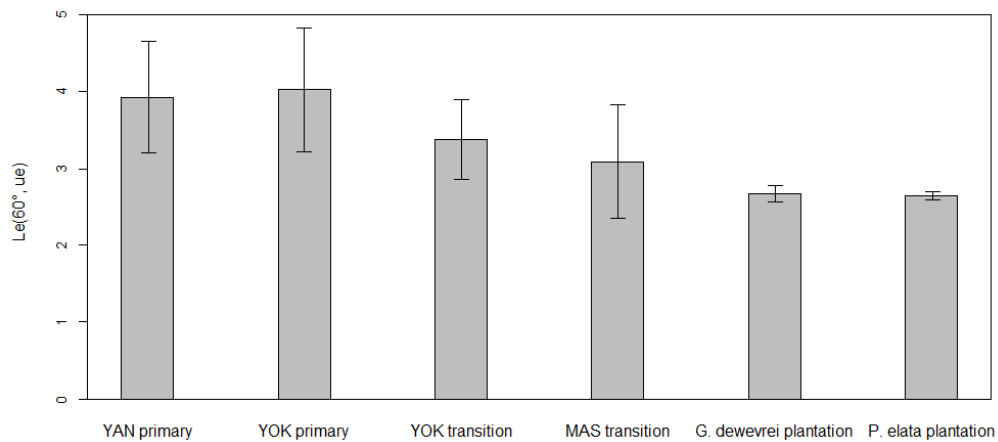


Figure 8: Overall assessment of $L_e(60^\circ, ue)$ of each forest type.

4.1 Software comparison - thresholding methods

First of all, an assessment of the image analysis using different software is made. This is based on a selection of images (108 images in total) from transition forests in Yoko and Masako. An overview of the structural parameters estimated for these plots is shown in Table 3, listing the parameters derived using the ECOM analysis.

Table 3: Overview of mean parameters of transition forests in Yoko and Masako, derived using ECOM.

	$L_e(60, st)$	$L_e(75, st)$	CO(% , st)	$L_e(60, ue)$	$L_e(75, ue)$	CO(% , ue)
YOK/2010/1	2.5	2.9	10.0	3.3	3.8	6.4
YOK/2010/2	2.8	3.0	6.5	3.5	3.7	3.5
YOK/2010/4	2.6	3.0	6.3	3.4	3.8	3.4
MAS/2010/1	2.6	2.8	8.9	2.9	3.1	7.7
MAS/2010/2	3.1	3.0	6.9	3.9	3.7	3.8

When comparing the thresholding methods, overall, the selected thresholds of the edge detection method are lower than the manually selected thresholds, and the thresholds from the ECOM fluctuate around the manually selected thresholds, but thresholds from ECOM have a larger dispersion than thresholds acquired with edge detection (Figure 9). In Table 4, a detailed comparison of the methods is shown, which are the results of a paired t-test on every separate image.

First, from Table 4, it can be observed that most parameters differ significantly from one another when derived using a different thresholding method. From inspection of the scatterplots (Figure 9), it is clear that the methods are significantly different and that different binary images will be produced. Although the derived parameters also differ significantly, it can be observed from their scatterplots (e.g. $L_e(75^\circ)$, Figure 10) that the data are closer to the 1:1 line.

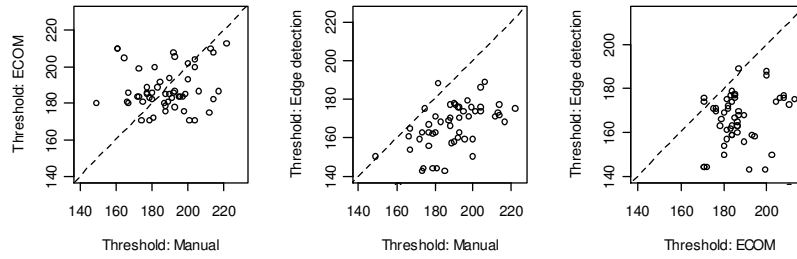
The only selected thresholds that do not differ significantly from each other are the manually selected thresholds and the threshold selected with ECOM for the standard exposed images. In the scatterplots displaying these two methods, a difference of up to 50 threshold units is visible, but the mean of the differences is almost 0. The structural parameters derived from these two thresholding methods also show a high similarity with the exception of $L_e(60^\circ, st)$. When comparing these two methods for the underexposed images, all parameters are significantly different. The automatically selected threshold using ECOM lies lower than the manually selected thresholds, with a mean of their difference of 19 thresholding units. These thresholds of ECOM more closely resemble the thresholds selected with edge detection, although their difference is still significant. The mean of the difference of the thresholding units between them is only 12, while it was 24 for the standard exposed images. The difference between manual thresholding and automatic thresholding using edge detection is highly significant, both for the selected thresholds as for the derived parameters.

Secondly, there is a difference between thresholding of the standard exposed and underexposed images. This difference is most obvious from the scatterplots. The selected thresholds are much lower for the underexposed images, as would be expected. The mean of the differences in thresholding units between the standard and underexposed images is 59 units for the ECOM analysis, 40 units for the manual selection and 48 units using edge detection (not shown in Table 4). The derived parameters from the underexposed images using the different thresholding methods are closer to the 1:1 line than the standard exposed images (Figure 10).

Table 4: Comparison of threshold units and derived parameters from different thresholding methods. Results of paired t-test of a selection of 18 measurement locations, 108 images. Significance codes: * $p < 0.05$; ** $p < 0.01$; *** $p < 0.001$.

	Manual - ECOM		Manual - Edge detection		ECOM - Edge detection	
	p-value	Mean of diff.	p-value	Mean of diff.	p-value	Mean of diff.
Threshold(st)	0.983	0.06	< 0.0001***	23.57	< 0.0001***	23.52
$L_e(60^\circ, st)$	< 0.0001***	0.30	< 0.0001***	0.17	0.001**	-0.13
$L_e(75^\circ, st)$	0.512	-0.02	< 0.0001***	0.17	< 0.0001***	0.19
CO(%, st)	0.051	-0.43	< 0.0001***	-1.02	0.015*	-0.59
Threshold(ue)	< 0.0001***	19.39	< 0.0001***	31.39	0.002**	12.00
$L_e(60^\circ, ue)$	< 0.0001***	0.54	< 0.0001***	0.28	< 0.0001***	-0.25
$L_e(75^\circ, ue)$	0.0006***	0.13	< 0.0001***	0.27	0.0003***	0.14
CO(%, ue)	< 0.0001***	-0.97	< 0.0001***	-0.82	0.447	0.16

Standard exposure



Underexposure

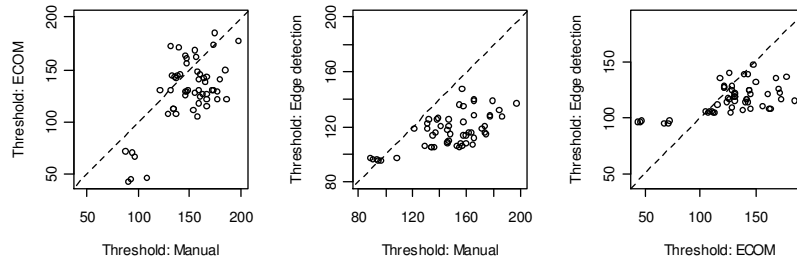
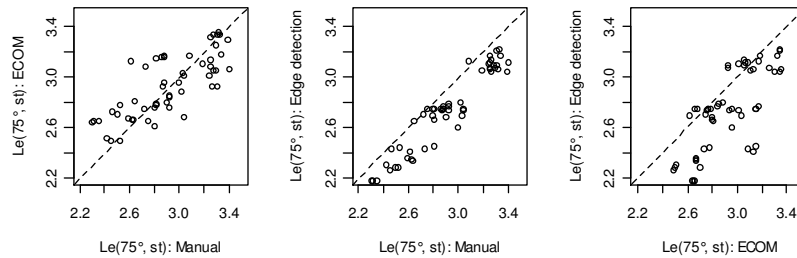


Figure 9: Scatterplots comparing the thresholds selected using manual threshold selection, the edge detection method and the ECOM. The dotted line indicates the 1:1 line. Upper three figures are from analysing images acquired with standard exposure value, lower three figures are from underexposed images.

Standard exposure



Underexposure

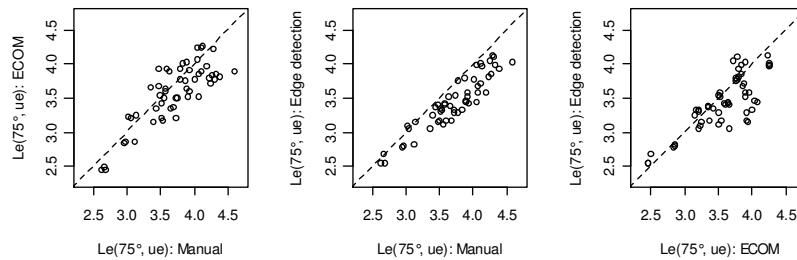


Figure 10: Scatterplots comparing structural parameter $L_e(75^\circ)$ derived from images analysed using the different thresholding methods. The dotted line indicates the 1:1 line. Upper three figures are from analysing images acquired with standard exposure value, lower three figures are from underexposed images.

Results of the replication of the manual thresholding are presented in Table 5. It is clear that when repeating the thresholding of standard exposed images, significant differences are obtained, both for the selected thresholds as for the derived parameters. Although the difference is significant, the mean of the difference is still rather small. The underexposed images are repeated with no significant difference.

Table 5: Comparison of replication of manual thresholding method for plots YOK/2010/1 and YOK/2010/2 (45 images), results of paired t-test. Significance codes: * $p < 0.05$; ** $p < 0.01$; *** $p < 0.001$.

	Manual - replication - st		Manual - replication - ue	
	p-value	Mean of diff.	p-value	Mean of diff.
Threshold	0.001***	-9.83	0.590	-1.79
$L_e(60^\circ)$	0.001**	-0.08	0.671	-0.01
$L_e(75^\circ)$	0.001***	-0.07	0.698	-0.01
CO(%)	0.001***	0.38	0.727	0.03

For the subsequent characterization of the spatial variability, the structural parameters of the three repetitions of images acquired at one measurement location are averaged. When repeating the paired t-test for averaged structural parameters per measurement location, given in Table 6, a difference in significance is noticeable with the parameters that are not averaged (Table 4). The differences between the parameters derived with manual thresholding and thresholding using ECOM, are less significant, both for standard exposed as underexposed images, still with the exception of $L_e(60^\circ)$. Additionally, the significance of the difference between the two automatic thresholding methods has decreased.

Table 6: Comparison of thresholding methods after averaging structural parameters for every measurement location. Results of paired t-test. Significance codes: * $p < 0.05$; ** $p < 0.01$; *** $p < 0.001$.

	Manual - ECOM		Manual - Edge detection		ECOM - Edge detection	
	p-value	Mean of diff.	p-value	Mean of diff.	p-value	Mean of diff.
$L_e(60^\circ, st)$	0.0004***	0.30	< 0.0001***	0.17	0.071	-0.13
$L_e(75^\circ, st)$	0.702	-0.02	< 0.0001***	0.17	0.002**	0.19
CO(%, st)	0.177	-0.43	< 0.0001***	-1.02	0.091	-0.59
$L_e(60^\circ, ue)$	< 0.0001***	0.54	< 0.0001***	0.28	0.002**	-0.25
$L_e(75^\circ, ue)$	0.017*	0.13	< 0.0001***	0.27	0.018*	0.14
CO(%, ue)	0.017*	-0.97	< 0.0001***	-0.82	0.653	0.16

4.2 Comparison with direct measurements

4.2.1 Plots in transition forest

In Figure 11, a comparison is made in every plot in transition forest between L_e from the hemispherical images and the direct LAI from the clearcut experiments. A pattern is visible in all plots, with the exception of MAS/2010/2, with the direct LAI higher than the L_e . Additionally the $L_e(75^\circ)$ is slightly higher than $L_e(60^\circ)$ (except MAS/2010/2) and the underexposed images systematically result in higher parameters than the standard exposed images. For YOK/2010/1, the direct LAI is the same as $L_e(75^\circ, ue)$. On the contrary, the direct LAI of YOK/2010/2 is almost double $L_e(75^\circ, ue)$. For YOK/2010/4 and MAS/2010/1, the direct LAI is similar, but the L_e for these plots differs, with lower L_e estimated for MAS/2010/1.

The different result in MAS/2010/2 is actually expected and can easily be explained since the visual site description of this plot was different than the others. A plot was selected containing only small trees, although the surrounding site also contained taller trees. Canopies of neighbouring trees were emerging over the plot, but since they were not actually in the plot they were not cut. The leaves of these trees are consequently not accounted for in the direct LAI, but obviously are present in the images and are accounted for in L_e resulting in the inverse relation between L_e and LAI. Additionally, in the plot MAS/2010/2, less understory was present, explaining the lower L_e at 75° than at 60° zenith angle, since $L_e(75^\circ)$ normally takes some understory into account.

A strict relationship between the direct LAI and L_e cannot be found.

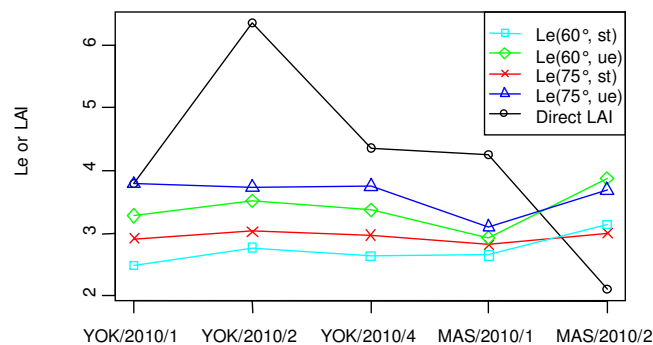


Figure 11: Comparison of different L_e values and direct LAI (Buggenhout, 2011) of every plot in transition forest.

4.2.2 Individual trees

A comparison is made between the L_e derived from images taken during the clearcut experiment in MAS/2010/1 after every tree was cut down, and the calculated direct LAI representing the same state (Figure 12). The total L_e does not match the L_e shown in Figure 11. The values in Figure 12 only account for the trees included in the clearcut experiment and not those that are present outside this plot. Trees that are visible at the edges of the image in which all the experimental trees are cut, are excluded.

In Figure 12, a clear but unexpected relation can be observed. The difference between parameters derived from subsequent images where one single tree was cut was not significant. Problems arise with overlapping vegetation elements of different trees and only very small differences are visible between subsequent images. For some trees, no difference is observed between the image where it was still present and the image where it is cut. The gap in Figure 12 represents a small group of trees that was cut down and that accounted for 1.1 of the direct LAI. This group was not observed with hemispherical photography. Small differences in thresholding and the resulting binary images also cause problems determining the differences between the images, sometimes even producing a slightly higher estimate for an image where a tree is cut as opposed to the image where the tree was still present.

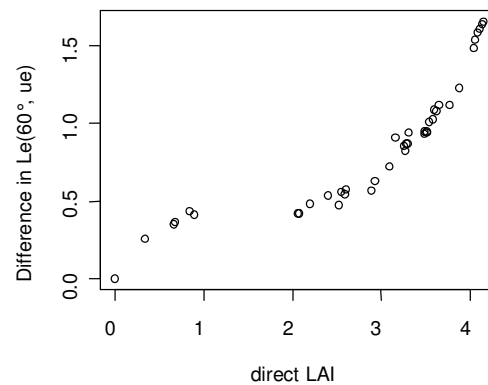


Figure 12: Estimated $L_e(60^\circ, ue)$ and direct LAI (Buggenhout, 2011) of the entire plot of MAS/2010/1 with subsequent cutting of individual trees during clearcut experiment. Every time a tree (or multiple trees) is cut down, a new assessment of standing leaf biomass is made.

4.3 Differences during image acquisition and analysis

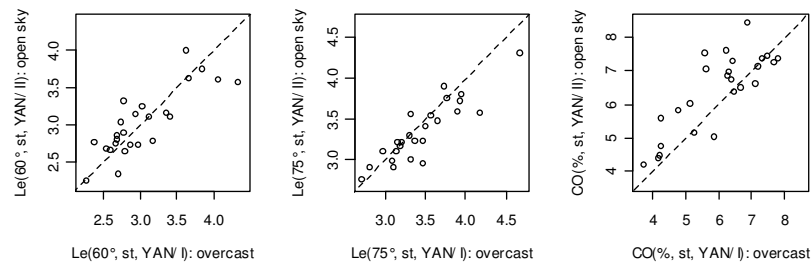
4.3.1 Weather conditions

The images of the entire plot YAN/I were taken in cloudy weather condition. Measurements in 1 ha of this plot, YAN/II, is repeated under extremely sunny conditions. These images are acquired at exactly the same measurement locations. The images taken in overcast sky conditions are compared with the images taken in clear sky conditions using a paired t-test (Table 7). A difference is found between the results obtained using different camera exposure settings. For the images taken with a standard exposure setting, the structural parameters $L_e(75^\circ)$ and CO are significantly different for the different weather conditions. This is not the case for $L_e(60^\circ)$. For the images acquired with an underexposed setting, no significant difference is found for any structural parameter, although the mean of the differences is higher for $L_e(60^\circ)$ and CO than with the standard exposed images. When examining the scatterplots (Figure 13), the images taken under sunny weather conditions with the standard exposure value produce a slightly lower $L_e(75^\circ)$ and slightly higher CO than images taken under overcast conditions. This is to be expected since sunlit leaves will be classified as sky, resulting in a lower L_e and higher CO values.

Table 7: Results of paired t-test for comparison of images acquired in different weather conditions. YAN/I represent images taken under even overcast sky; YAN/II represent images taken under clear sky. The first columns compare images taken with the standard exposure value, the second columns compare underexposed images. Significance codes: * $p < 0.05$; ** $p < 0.01$; *** $p < 0.001$.

	YAN/I - YAN/II - st		YAN/I - YAN/II - ue	
	p-value	Mean of diff.	p-value	Mean of diff.
$L_e(60^\circ)$	0.926	0.01	0.283	-0.10
$L_e(75^\circ)$	0.015*	0.12	0.959	3.10^{-3}
CO(%)	0.005**	-0.45	0.487	-0.86

Standard exposure



Underexposure

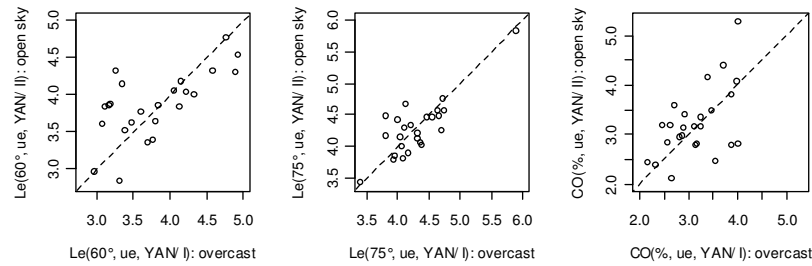


Figure 13: Scatterplot comparing $L_e(60^\circ)$, $L_e(75^\circ)$ and CO acquired from images taken in cloudy weather condition (YAN/I) and in sunny weather conditions (YAN/II). The dotted line indicates the 1:1 line. Upper three figures compare images taken with standard exposure value, lower three figures compares underexposed images.

4.3.2 Zenith angle

L_e derived from analysis using different zenith angle produce highly significantly different results. The scatterplots (Figure 14) comparing $L_e(60^\circ)$ and $L_e(75^\circ)$ assigned to every measurement location for the selected images, show a distinct pattern. Overall, $L_e(75^\circ)$ seems to be higher than $L_e(60^\circ)$. This changes at higher L_e values, where $L_e(75^\circ)$ features a lower estimate than $L_e(60^\circ)$. The same pattern occurs for the standard and underexposed images.

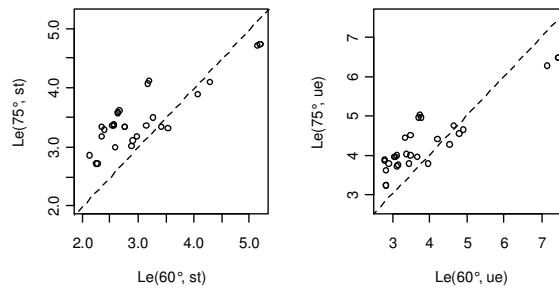


Figure 14: Comparison of L_e analysed using zenith angles 60° and 75° . The dotted line indicates the 1:1 line. Left: standard exposure; Right: underexposed.

4.3.3 Gap fraction distributions

Figure 15 shows three examples of gap fraction distributions in function of the zenith angles used for analysis. From these distributions it is clear that vegetation elements are not randomly distributed within the canopy. If this were the case, the gap fraction would be maximal at small zenith angles and decrease towards higher zenith angles since the probability of light penetration, i.e. the probability of seeing a gap, would decrease when looking at increasing angles deviating from the lenses optical axis. From Figure 15, it is also obvious that the distribution is dependent on the measurement location and it is not possible to assign a single gap fraction distribution to an entire plot.

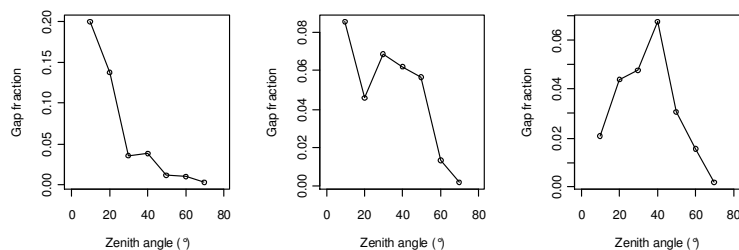


Figure 15: Different gap fraction distributions derived from hemispherical images obtained at different measurement locations (A250, A300 and B175) in YOK/I.

4.3.4 Exposure settings

Images acquired with a different exposure value result in different structural parameters. Overall, a higher L_e and a lower value of CO are obtained for images acquired in an underexposed mode. Figure 16 shows the comparison of parameters derived from the images taken with the standard exposure setting and the underexposed setting. For every structural parameter, a highly significant difference (paired t-test; p-values < 0.0001) is found when acquired with the different exposure settings. For $L_e(60^\circ)$, a mean difference of 0.8 is found, which is an increase of 26% in value obtained from the underexposed image in comparison to the value from the standard exposed image. For $L_e(75^\circ)$, the

mean difference is 0.8, relatively similar to that of $L_e(60^\circ)$, with an increase of 24% over the standard image. For CO the mean difference is 2.7 which equals a decrease of 45% of the standard image. The reason for these differences is obvious from examining the images (Figure 5). Openings in the canopy appear larger in the images with a standard exposure setting. When the binary version of these images is created, it is obvious that less pixels are classified as leaves for the standard exposure setting as compared to the underexposed images.

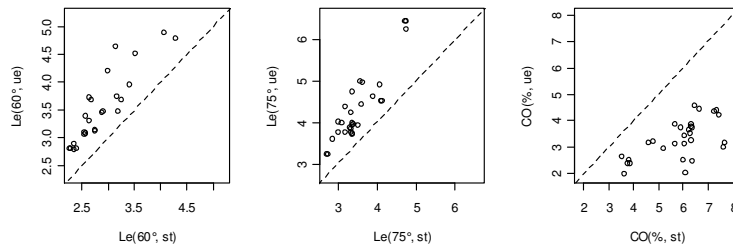


Figure 16: Comparison of structural parameters obtained from images acquired with a different exposure setting. The dotted line indicates the 1:1 line.

4.3.5 Channels of RGB

In Figure 17, a small section of an image is shown from a photograph taken under cloudy conditions and representative for the majority of the images. In these optimal conditions, little difference can be seen between the true colour image and the red, green or blue channel, except for the grey tone. Based on visual analysis, there are no areas in the images that appear to be covered by leaves in the true colour image and not in the separate channels of the image or vice versa. A difference can be seen among the separate channels. The blue channel seems to be darker in tone, explained by the higher absorption of light in this channel. Intuitively, the transformation of the blue channel into a binary image would be more accurate, since there is a greater difference in grey levels of leaves and sky. This difference in tones of grey between the three channels is less clear in the image taken with underexposure. In these underexposed images, it could be expected that the choice of channel is less significant.

The comparison of the results of the analysis of the different colour channels of the RGB image are shown in Table 8. All structural parameters obtained from analysis of the three channels of the standard exposed images are significantly different from one another. The mean of the differences of the threshold units and the parameters between the blue and the green channels is larger than between any other channels. The blue and red channels also produce different results, although the mean of the difference is lower than between the blue and green channel. Parameters derived from the red and green channel more closely resemble each other. When looking at the grey levels of these extracted channels (Figure 17), these channels do look similar, especially for the standard exposure settings. For the underexposed images, a higher correlation is found for all the channels.

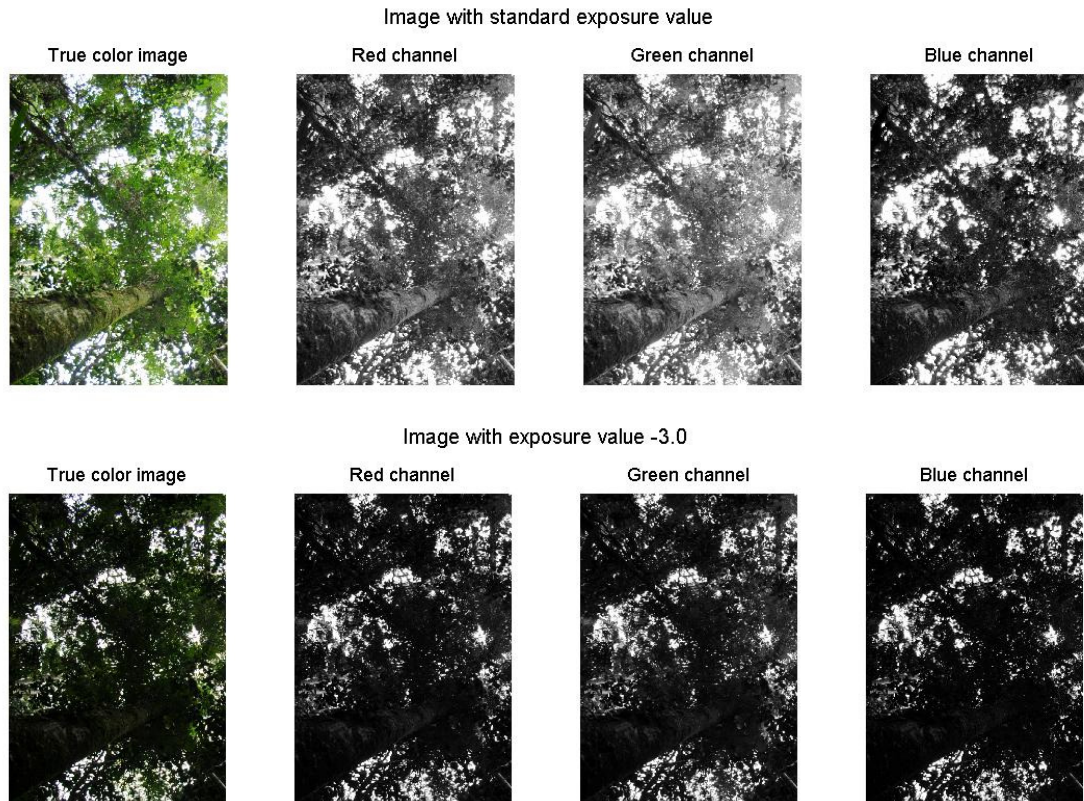


Figure 17: Parts of image in plot YOK/I (primary forest); first row are parts of the image with standard exposure value; second row are parts of the image with underexposure.

Table 8: Results of paired t-test, comparing the thresholds and structural parameters acquired from analysis of different channels, YOK/2010/1 (24 images). Significance codes: * $p < 0.05$; ** $p < 0.01$; *** $p < 0.001$.

	Blue - Green		Blue - Red		Green -Red	
	p-value	Mean of diff.	p-value	Mean of diff.	p-value	Mean of diff.
Threshold(st)	< 0.0001***	-44.75	< 0.0001***	-24.95	< 0.0001***	19.80
$L_e(60^\circ, st)$	< 0.0001***	-0.37	< 0.0001***	-0.20	0.017*	0.17
$L_e(75^\circ, st)$	< 0.0001***	-0.37	0.0007***	-0.18	0.011*	0.19
CO(% , st)	< 0.0001***	0.71	< 0.0001***	0.43	0.0008***	-0.29
Threshold(ue)	0.579	-5.07	0.813	1.87	0.562	6.93
$L_e(60^\circ, ue)$	0.599	0.07	0.786	0.03	0.826	-0.04
$L_e(75^\circ, ue)$	0.180	0.21	0.217	0.17	0.826	-0.05
CO(% , ue)	0.006**	-6.59	0.026*	-5.45	0.739	1.14

4.4 Spatial variation – Primary forest

4.4.1 Variation of the forest structure

In Table 9, summary statistics of every plot are shown. The coefficient of variation ($CV = 100 \cdot SD / \text{Mean}$) is included to improve comparability between the different plots. The combination of YOK/II and YOK/III is also included, since this was necessary for interpolation of YOK/III, as will be discussed below. The table is arranged per structural parameter, facilitating the comparison of the plots. The plots do show a high similarity in all the summary statistics. For the standard exposure setting, an overall mean of 3.2 for $L_e(60^\circ)$, with an absolute minimum of 2.0 and an absolute maximum of 6.0 is found. For $L_e(75^\circ)$, an overall mean of 3.8 is obtained ranging between 2.5 and 5.5. The overall mean of 5.5 % is found as CO, ranging between 2.1 and 10.7 %. As discussed previously, the values obtained using the underexposed images are higher for both L_e and lower for CO. For $L_e(60^\circ)$ an overall mean of 4.0 is found with 2.6 as minimum and 7.4 as maximum. The mean for $L_e(75^\circ)$ is 4.4 and ranges between 3.3 and 7.4. Lastly a mean of 3.0 % ranging between 1.1 and 6.4 % is obtained for CO.

Tukey's HSD test was used to compare the means of the plots separately, including an overall comparison of primary and transitional forest stands (Table 10). Values of the parameters of transition forest can be found in Table 3. The comparison of YOK/I and YOK/II shows that small scale variations are not significant for any of the structural parameters. Even large scale variations assessed by comparison of means of YAN/I with both YOK/I and YOK/II, show no significant difference for the structural parameters with the exception of $L_e(75^\circ, \text{st})$. The comparison of the means of YOK/II and YOK/III, which have a different sampling scheme and also topographical differences, showed significantly different results for $L_e(75^\circ, \text{st})$ and CO(% , st). Significant differences are found between the different stand types. Primary forests feature a larger value of L_e and a lower value of CO. The mean of difference is larger for parameters derived from underexposed images.

Table 10: Results of Tukey's HSD test, comparing the means of the different plots. Significance codes: * $p < 0.05$; ** $p < 0.01$; *** $p < 0.001$.

	YOK/I - YAN/I		YOK/II - YAN/I		YOK/II - YOK/I		YOK/III - YOK/II		Prim. - Trans.	
	p-value	Diff.	p-value	Diff.	p-value	Diff.	p-value	Diff.	p-value	Diff.
$L_e(60^\circ, \text{st})$	0.251	0.12	0.929	0.04	0.602	-0.08	0.995	-0.02	< 0.0001***	0.55
$L_e(75^\circ, \text{st})$	0.036*	0.13	0.785	0.05	0.295	-0.09	0.038*	-0.16	< 0.0001***	0.66
CO(% , st)	0.353	-0.21	0.455	-0.19	0.998	0.02	0.012*	0.48	< 0.0001***	-2.47
$L_e(60^\circ, \text{ue})$	0.441	0.12	0.996	0.02	0.581	-0.11	0.929	0.06	< 0.0001***	0.73
$L_e(75^\circ, \text{ue})$	0.104	0.14	0.983	0.02	0.224	-0.12	0.690	-0.08	< 0.0001***	0.84
CO(% , ue)	0.806	-0.07	0.975	-0.03	0.964	0.04	0.997	0.02	< 0.0001***	-2.34

Table 9: Summary statistics of every plot in primary forest, arranged per exposure setting and per structural parameter.

	Mean	SD	CV (%)	Min.	1st Qu.	Median	3rd Qu.	Max.	N° of gridpoints
$L_e(60^\circ, \text{st}, \text{YAN/I})$	3.2	0.6	18.2	2.0	2.8	3.1	3.5	6.0	169
$L_e(60^\circ, \text{st}, \text{YOK/I})$	3.3	0.6	18.4	2.2	2.9	3.2	3.5	5.3	169
$L_e(60^\circ, \text{st}, \text{YOK/II})$	3.2	0.6	18.6	2.1	2.8	3.1	3.5	5.2	169
$L_e(60^\circ, \text{st}, \text{YOK/III})$	3.2	0.6	18.7	2.4	2.8	3.0	3.4	5.2	85
$L_e(60^\circ, \text{st}, \text{YOK/II/III})$	3.2	0.6	18.7	2.1	2.8	3.0	3.5	5.2	245
$L_e(75^\circ, \text{st}, \text{YAN/I})$	3.6	0.5	12.9	2.5	3.2	3.5	3.7	5.3	169
$L_e(75^\circ, \text{st}, \text{YOK/I})$	3.7	0.4	11.9	3.0	3.4	3.6	3.9	5.5	169
$L_e(75^\circ, \text{st}, \text{YOK/II})$	3.6	0.4	11.9	2.8	3.3	3.5	3.7	5.4	169
$L_e(75^\circ, \text{st}, \text{YOK/III})$	3.4	0.5	14.2	2.5	3.2	3.4	3.7	5.2	85
$L_e(75^\circ, \text{st}, \text{YOK/II/III})$	3.5	0.4	12.6	2.5	3.3	3.5	3.7	5.3	245
$\text{CO}(\%, \text{st}, \text{YAN/I})$	5.5	1.4	24.7	2.1	4.4	5.6	6.3	10.7	169
$\text{CO}(\%, \text{st}, \text{YOK/I})$	5.3	1.0	19.0	2.7	4.8	5.3	5.9	8.5	169
$\text{CO}(\%, \text{st}, \text{YOK/II})$	5.3	1.1	19.7	3.1	4.6	5.2	6.0	8.3	169
$\text{CO}(\%, \text{st}, \text{YOK/III})$	5.8	1.2	21.4	2.9	5.1	5.7	6.5	8.9	85
$\text{CO}(\%, \text{st}, \text{YOK/II/III})$	5.5	1.2	21.0	2.9	4.7	5.4	6.2	8.9	245
$L_e(60^\circ, \text{ue}, \text{YAN/I})$	3.9	0.7	18.3	2.8	3.5	3.8	4.3	6.9	169
$L_e(60^\circ, \text{ue}, \text{YOK/I})$	4.1	0.8	19.0	2.6	3.6	4.0	4.5	6.9	169
$L_e(60^\circ, \text{ue}, \text{YOK/II})$	4.0	0.8	20.4	2.6	3.5	3.8	4.3	7.4	169
$L_e(60^\circ, \text{ue}, \text{YOK/III})$	4.0	0.8	18.7	2.9	3.5	3.8	4.3	6.9	87
$L_e(60^\circ, \text{ue}, \text{YOK/II/III})$	4.0	0.8	20.0	2.6	3.5	3.8	4.3	7.4	247
$L_e(75^\circ, \text{ue}, \text{YAN/I})$	4.4	0.5	12.6	3.4	4.0	4.3	4.6	7.2	169
$L_e(75^\circ, \text{ue}, \text{YOK/I})$	4.5	0.6	13.3	3.5	4.1	4.4	4.8	7.4	169
$L_e(75^\circ, \text{ue}, \text{YOK/II})$	4.4	0.6	13.4	3.4	4.0	4.3	4.6	6.6	169
$L_e(75^\circ, \text{ue}, \text{YOK/III})$	4.3	0.6	13.6	3.3	4.0	4.1	4.5	6.5	87
$L_e(75^\circ, \text{ue}, \text{YOK/II/III})$	4.3	0.6	13.3	3.3	4.0	4.3	4.6	6.6	247
$\text{CO}(\%, \text{ue}, \text{YAN/I})$	3.0	0.8	25.3	1.1	2.5	2.9	3.5	6.2	169
$\text{CO}(\%, \text{ue}, \text{YOK/I})$	3.0	0.7	22.9	1.2	2.5	2.9	3.3	5.4	169
$\text{CO}(\%, \text{ue}, \text{YOK/II})$	3.0	0.7	24.3	1.4	2.5	2.9	3.5	6.4	169
$\text{CO}(\%, \text{ue}, \text{YOK/III})$	3.0	0.6	21.1	1.5	2.6	3.0	3.4	5.4	87
$\text{CO}(\%, \text{ue}, \text{YOK/II/III})$	3.0	0.7	23.4	1.4	2.5	2.9	3.4	6.4	247

4.4.2 Patterns of variation of structural parameters

The location maps of every structural parameter at all sites can be found in Appendix 4, and provide a first idea of the macrostructure of the sites. The computed experimental variograms and the fitted theoretical variograms of each structural parameter of each plot can be found in Figure 18 for the standard exposed images and in Figure 19 for the underexposed images. The characteristics used for fitting the variogram model are summarized in Table 11. The errors found with crossvalidation are the smallest errors that were obtained when testing multiple theoretical variograms. The characteristics of the theoretical variogram yield information on the spatial patterns within each plot and are a basis of comparison between the plots. Especially the range is important, indicating that

the variance is spatially dependent over a specific scale. The nugget provides an idea of the variation at distance 0. A nugget different from 0 indicates that the variance is not attributed to spatial dependence. This nugget could be caused by measurement errors or by variations at small distances (Burrows *et al.*, 2002).

It was not possible to fit a theoretical variogram model for all parameters at all sites. From literature, it is known that variograms generally show two phases. A first ascending phase where the variability is spatially dependent and a second phase where a plateau is reached starting at the range, indicating no further spatial dependence of the variability. For most of the generated experimental variograms, the range could easily be defined, but the plateau does not remain stable beyond this range. For some parameters, points randomly fluctuate around the plateau defined with the theoretical variogram, e.g. $L_e(75^\circ, st, YAN/I)$ and $L_e(75^\circ, ue, YOK/I)$. For others, a slight wave pattern is visible, where the points fluctuate in an orderly manner around the plateau, e.g. $L_e(75^\circ, st, YOK/II)$. This wave pattern is especially visible for the experimental variograms of YOK/II/III, where a larger maximal distance for the variogram was computed. The fitting of the theoretical variograms is optimized for the points before the range, with less emphasis on points at larger distances. These models produced the smallest errors after crossvalidation.

For $L_e(60^\circ, st)$ and $L_e(60^\circ, ue)$ of YAN/I, the fitting of a suitable theoretical variogram was not obvious. The experimental variogram of $L_e(60^\circ, st)$ (Figure 18) is a waveform with only two points ascending in the first wave before the descent starts. A similar wave pattern is visible in the first experimental variogram of $L_e(60^\circ, ue)$ (Figure 19, (A)). For this parameter, the experimental variogram varied strongly when choosing a different number of lags and lag separation. A second experimental variogram for $L_e(60^\circ, ue)$ (Figure 19, (B)) is shown where the wave pattern is minimized and a pure nugget effect is visible, indicating all variability is random and unstructured. This pure nugget effect means that every observation is completely independent from the others, which is clearly different from the wave pattern found with the first experimental variogram. Additionally, the experimental variogram of CO(%), st) of YOK/I shows another pattern which is difficult to model. The variogram starts in a concave manner and does not allow the fitting of an exponential or spherical type of theoretical variogram. No theoretical variograms are fitted for these parameters and consequently no interpolation maps are created.

The estimated range per structural parameter differs slightly for each plot. When looking at small scale variations, comparing YOK/I and YOK/II, the ranges are quite similar. The largest difference in range between them is for the parameter $L_e(75^\circ, ue)$, with 36m range for YOK/I and 71m for YOK/II, although this difference is probably due to the applied type of variogram model. All other parameters show a high similarity, indicating a similar spatial variability of these parameters on a small scale. When inspecting large scale variations, comparing YAN/I with YOK/I and YOK/II, a difference can be seen. The ranges of YAN/I are systematically slightly lower than the ones of YOK/I and YOK/II, with the exception of $L_e(75^\circ, ue, YOK/I)$. Note that within YAN/I, all parameters have a very similar range between 42 and 54 m. This overall similarity within one plot is not found within the other plots.

The ranges between YOK/II and YOK/II/III do show a large difference, indicating measurement scale variations. Only the range of parameter $L_e(75^\circ)$ is similar. All other parameters of YOK/II/III have a very large range in comparison the ranges found in 9ha plots.

Overall, smaller errors for L_e were computed with the standard exposed images and for CO, the underexposed images gave a better result using crossvalidation.

Table 11: Characteristics used for the computation of the experimental variogram and the theoretical variogram model. Results of crossvalidation using the variogram model for prediction of sample points.

	Experimental variogram		Variogram model				Crossvalidation	
	N° of lags	Lag sep. (m)	Type	Nugget	Sill	Range (m)	RMSE	MAEE
$L_e(60^\circ, \text{st}, \text{YAN/I})$	16	10						
$L_e(60^\circ, \text{st}, \text{YOK/I})$	14	7	Exp.	0.17	0.22	39	0.622	0.466
$L_e(60^\circ, \text{st}, \text{YOK/II})$	16	6	Exp.	0.13	0.227	43.2	0.593	0.446
$L_e(60^\circ, \text{st}, \text{YOK/II/III})$	10	36	Exp.	0.27	0.10	140.4	0.644	0.486
$L_e(75^\circ, \text{st}, \text{YAN/I})$	10	14	Exp.	0.01	0.185	54	0.400	0.280
$L_e(75^\circ, \text{st}, \text{YOK/I})$	14	7	Sph.	0.125	0.075	83.3	0.421	0.316
$L_e(75^\circ, \text{st}, \text{YOK/II})$	12	12	Sph.	0.076	0.116	90.72	0.351	0.263
$L_e(75^\circ, \text{st}, \text{YOK/II/III})$	14	24	Sph.	0.07	0.115	67.2	0.416	0.318
$\text{CO}(\%, \text{st}, \text{YAN/I})$	10	14	Exp.	0.1	1.65	51	1.231	0.985
$\text{CO}(\%, \text{st}, \text{YOK/I})$	11	12						
$\text{CO}(\%, \text{st}, \text{YOK/II})$	10	12	Exp.	0.45	0.65	72	0.991	0.797
$\text{CO}(\%, \text{st}, \text{YOK/II/III})$	14	30	Exp.	0.72	0.48	162	1.141	0.895
$L_e(60^\circ, \text{ue}, \text{YAN/I})$	$16^{(A)}/10^{(B)}$	$10^{(A)}/15^{(B)}$						
$L_e(60^\circ, \text{ue}, \text{YOK/I})$	12	8	Exp.	0.1	0.54	29.76	0.780	0.587
$L_e(60^\circ, \text{ue}, \text{YOK/II})$	10	15	Exp.	0.25	0.43	42	0.806	0.595
$L_e(60^\circ, \text{ue}, \text{YOK/II/III})$	11	36	Exp.	0.46	0.27	118.8	0.815	0.620
$L_e(75^\circ, \text{ue}, \text{YAN/I})$	10	14	Exp.	0.08	0.205	42	0.523	0.372
$L_e(75^\circ, \text{ue}, \text{YOK/I})$	12	8	Sph.	0.05	0.32	36.48	0.586	0.423
$L_e(75^\circ, \text{ue}, \text{YOK/II})$	14	9	Exp.	0.01	0.35	70.56	0.505	0.373
$L_e(75^\circ, \text{ue}, \text{YOK/II/III})$	12	35	Exp.	0.03	0.33	81	0.541	0.404
$\text{CO}(\%, \text{ue}, \text{YAN/I})$	10	14	Exp.	0.18	0.42	51	0.748	0.565
$\text{CO}(\%, \text{ue}, \text{YOK/I})$	15	7	Exp.	0.32	0.13	69.3	0.691	0.534
$\text{CO}(\%, \text{ue}, \text{YOK/II})$	10	12	Exp.	0.13	0.38	62.4	0.674	0.546
$\text{CO}(\%, \text{ue}, \text{YOK/II/III})$	13	34	Exp.	0.3	0.21	123.8	0.684	0.549

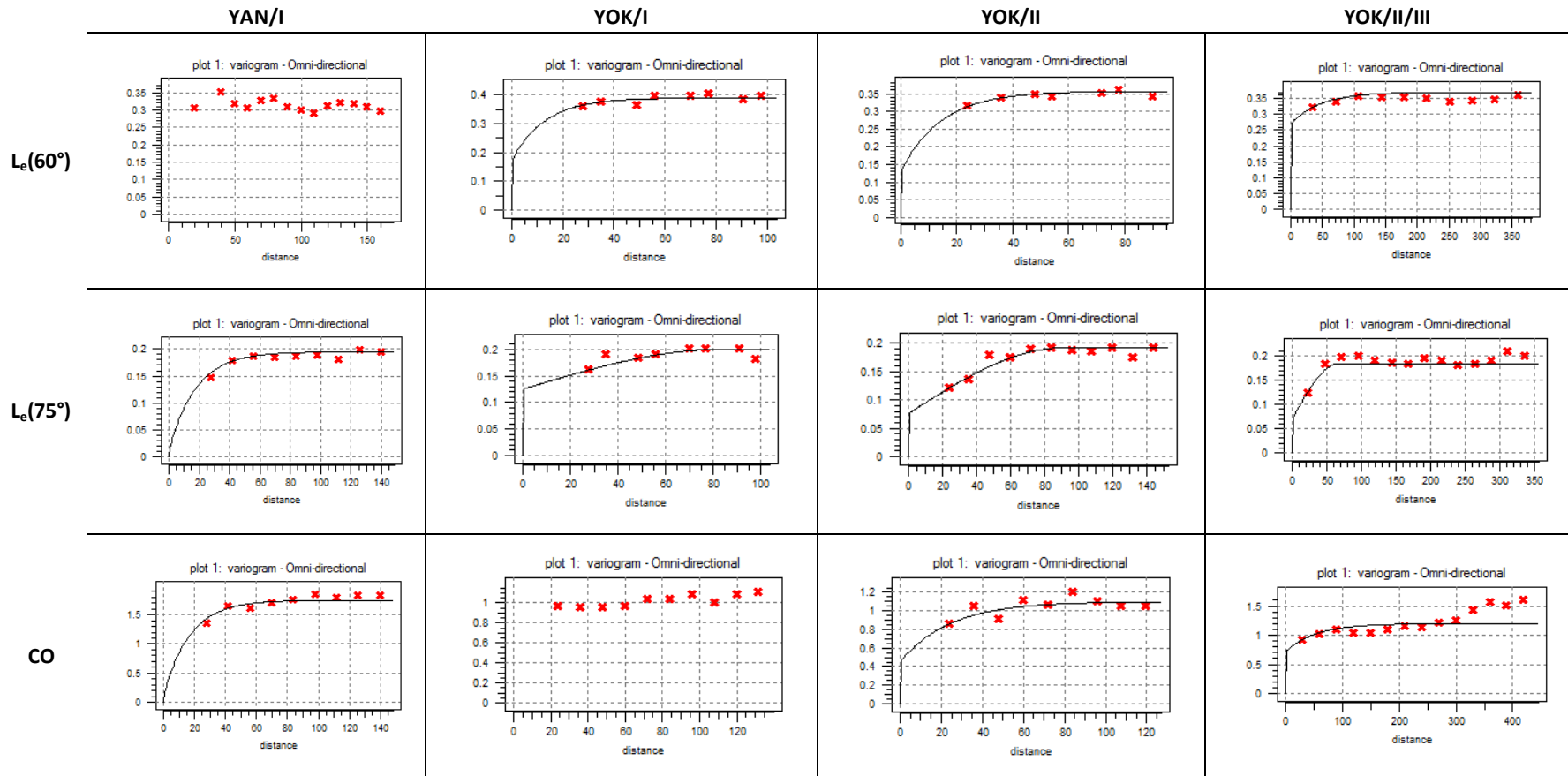


Figure 18: Experimental variograms and fitted theoretical variogram models of each plot. The distance is expressed in m. All structural parameters are derived from images taken with standard exposure values.

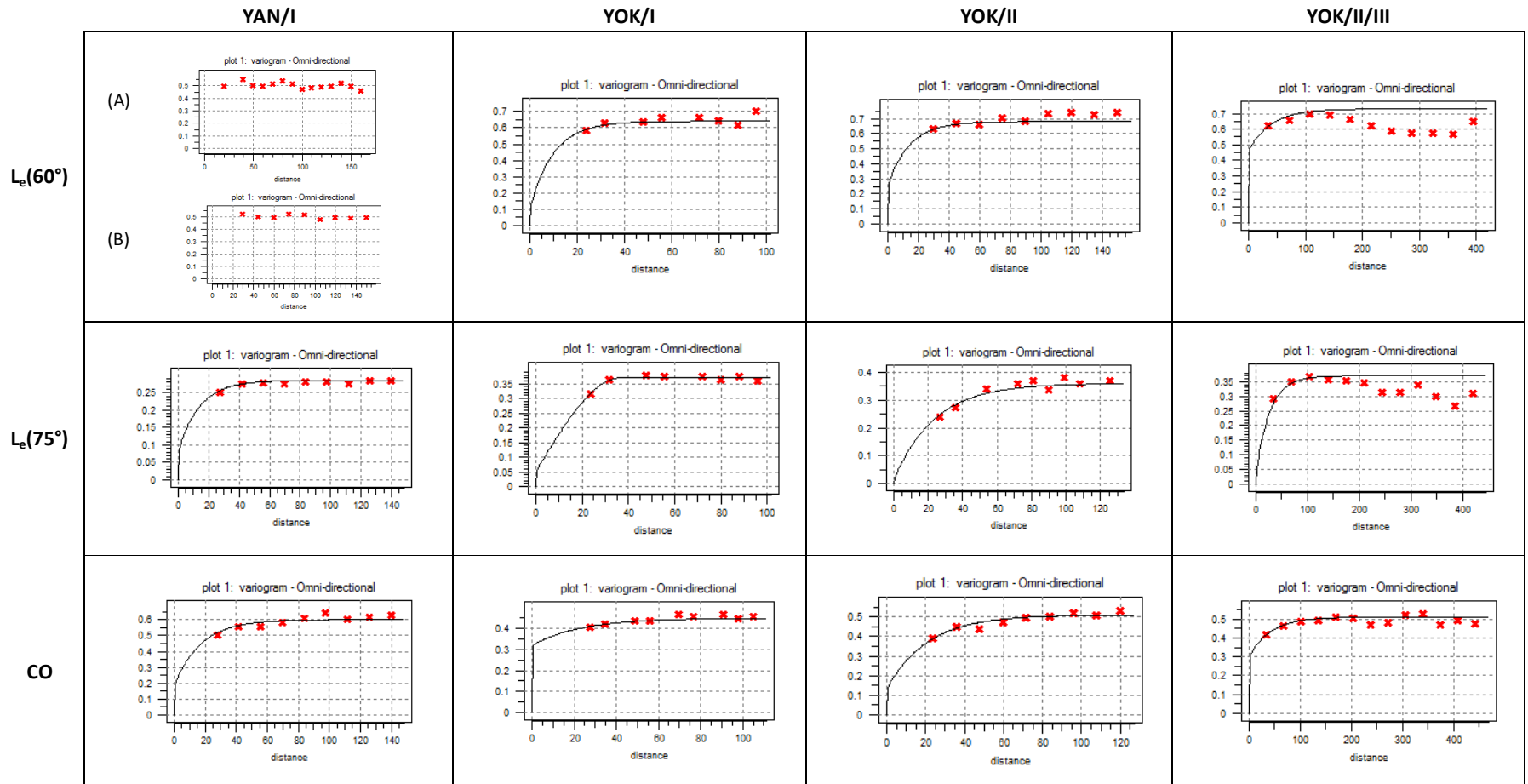


Figure 19: Experimental variograms and fitted theoretical variogram models of each plot. The distance is expressed in m. All structural parameters are derived from images taken with underexposed camera settings.

For visual representation of the spatial variability of a structural parameter within one plot, all theoretical variograms were used for the production of interpolation maps for which ordinary kriging was used. All maps can be found in Appendix 5.

In Figure 20, the interpolation maps of the parameters of YOK/II are shown. A link can be seen between the different parameters. The locations of lower and higher L_e are similar. Note that the range for $L_e(75^\circ)$ was estimated double the range of $L_e(60^\circ)$, resulting in a more coherent interpolation. An inverse relationship can be seen between both L_e and CO. Regions with a lower L_e give a higher CO and reversed. Correlation analysis using Spearman Rank correlation test confirms a significant negative relationship ($p < 0.0001$) between L_e and CO, with correlation coefficient of -0.538 between $L_e(60^\circ)$ and CO and -0.683 between $L_e(75^\circ)$ and CO. When plotting these parameters in a scatterplot (Figure 21), the same relation is found, although a strict pattern is not visible. Note that the relation between $L_e(60^\circ)$ and $L_e(75^\circ)$ is the same one as discussed in section 4.3.2, stating that $L_e(75^\circ)$ is generally higher, but that this relation changes at high L_e .

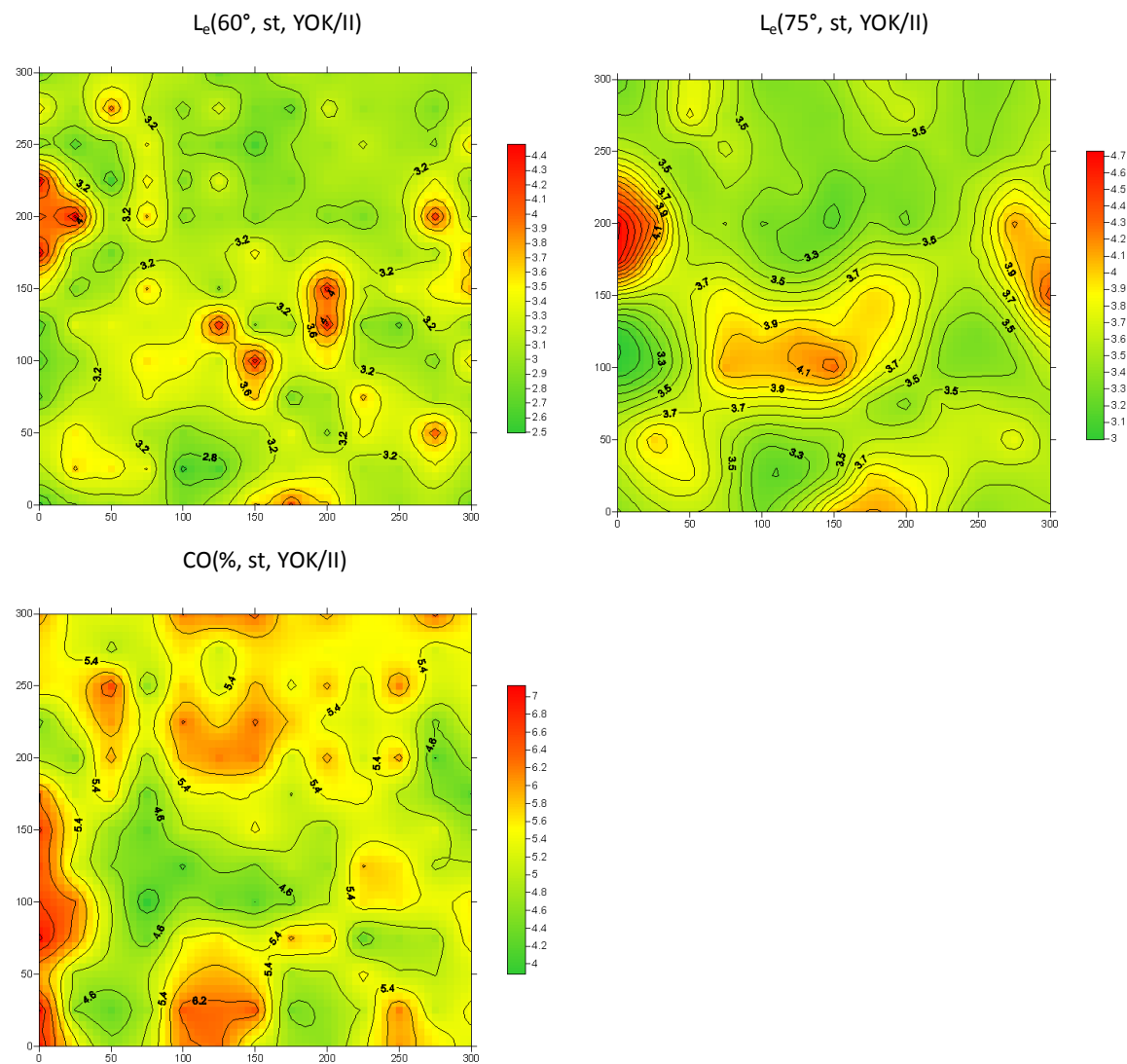


Figure 20: Interpolation maps of all structural parameters of YOK/II, st.

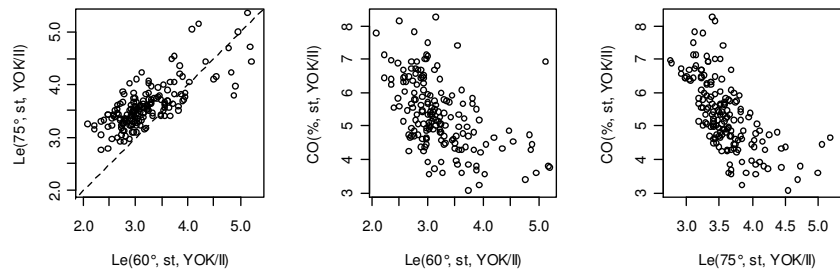


Figure 21: Comparison of structural parameters of YOK/II, st.

From some of the estimated ranges, it appears that the sampling method was not optimal and distances between measurement locations were too large. This is clearly illustrated when these variograms are used for the production of interpolation between the measurement locations. For example, the variogram of $L_e(60^\circ, \text{st}, \text{YOK/I})$ has a range of 39m, meaning that only four neighbouring measurement locations are used for interpolation. On the kriging map of this parameter (Figure 22), the points of sampling are easily distinguished and the interpolation is simply a variation of circles around the measurement locations. A more coherent map is produced with the interpolation map of $L_e(75^\circ, \text{st}, \text{YOK/I})$. This map is based on a variogram with a range of 83m, indicating that more neighbours are used during interpolation. The coherency of the maps is a result of the applied sampling scheme, discussed in detail in section 5.2.1. When inspecting the maps closely, a similar pattern of L_e is visible. For YOK/III, this effect is even larger, especially for the parameter $L_e(75^\circ, \text{YOK/II/III})$ (see Appendix 5). Both for the standard as for the underexposed images, the estimated range is smaller than the distance between two measurement locations of YOK/III itself. The applied sampling scheme is not suitable for interpolation between these measurement locations.

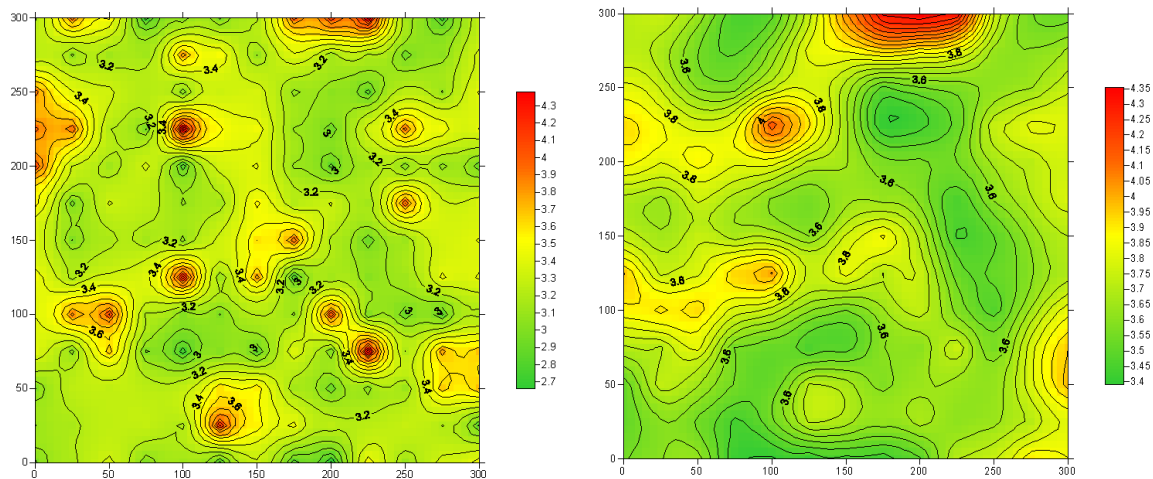


Figure 22: Interpolation maps for $L_e(60^\circ, \text{st})$ (left) and $L_e(75^\circ, \text{st})$ (Right) for plot YOK/I.

5 Discussion

A large variation exists among the reported LAI values of tropical rainforests which makes it difficult to assign a typical LAI value to different geographical variants of moist evergreen forest. Scurlock *et al.* (2001) reported a mean value of 4.8 ± 1.7 for tropical evergreen broadleaf forests ranging between 1.5 and 8.0 after removal of outliers. This is a worldwide average for this particular biome, which does not take into account that large regional variations exist. Leigh (1990) reported LAI values between 6 and 8 for tropical lowland forest. Besides the varying results due to regional variations, inconsistencies can be caused by methodological problems, both from direct and indirect measurements (Wirth *et al.*, 2001).

The values obtained in this study are still in the reported range of Scurlock *et al.* (2001), but the estimates are lower than what would be expected for these specific forests. When comparing with published results using optical methods in tropical rainforests, our results are quite low. Published values average around an LAI of 5 (see literature review section 2.3.2; reported values of Trichon *et al.*, 1998; Meir *et al.*, 2000; Vierling and Wessman, 2000; de Wasseige *et al.*, 2003; Malhado *et al.*, 2009).

The average L_e obtained in this study using hemispherical photography are rather low, with mean values derived from standard exposed images ranging between 3.2 and 3.7 for primary forest and between 2.5 and 3.1 for transition forest. Mean values derived from underexposed images are slightly higher, and thus more closely resemble the published values, with ranges between 3.9 and 4.5 for primary forest and between 2.9 and 3.9 for transition forest.

The estimated values of CO are in the same line as reported in literature (section 2.4; reported values of Ostertag, 1998; Richards, 1996). In this study, mean values from standard exposed image vary between 5.3% and 5.8% in primary forest and between 6.3% and 10% in transition forest. The values are lower when derived from underexposed images and are around 3% in primary forest and range between 3.4% and 6.5% in transition forest.

The remainder of this discussion is divided in two main parts. In the first part the used methodology of hemispherical canopy photography including image acquisition and the analysis of the images is assessed and in the second part the spatial variability in canopy structure over the different plots, including the used sample scheme, is discussed.

5.1 Part 1: Assessment of hemispherical canopy photography

5.1.1 Structural parameters and the associated inaccuracies

As mentioned at the start of this discussion, the obtained mean values of L_e are lower than expected. Several factors cause inaccuracies in the structural parameters derived from hemispherical images through gap fraction assessment. The assumptions associated with the gap fraction model are an important issue since they could not all be met, with clumping as the most serious problem. Other

problems include saturation and the used light extinction coefficient. Each topic is discussed separately below.

The variations recorded in a single plot however are considerably large. For example the mean value 4.1 of $L_e(60^\circ, ue)$ in YOK/I ranged between a minimum of 2.6 and a maximum of 6.9, indicating that the instrument is sensitive enough to capture the expected large variability of LAI in tropical rainforest.

The estimate of L_e differs according to the selected range of zenith angles used for analysis. This difference can be assigned to the presence of understory in the edge of the image and consequently included in the L_e value when large zenith angles are used for analysis. The amount of understory also changes as a relation to the canopy structure. When the canopy is less dense, more light reaches the lower levels and more understory is present, which results in $L_e(75^\circ)$ being higher than $L_e(60^\circ)$. When canopies become denser, less understory can develop and $L_e(60^\circ)$ is higher than $L_e(75^\circ)$. This effect can be seen in Figures 14 and 21. $L_e(60^\circ)$ seems more appropriate for the characterization of the canopy structure since the understory is excluded.

The estimated value of L_e also depends on the exposure setting used, with on average a 25% increase due to the use of underexposed images instead of the standard exposed images.

The CO is a reliable structural parameter since its calculation is based on a simple pixel count and does not involve particular assumptions concerning the canopy structure. Inaccuracies in estimated values will occur due to an inexact adaptation of threshold levels, but are more easily overcome than the problems encountered for L_e estimation. CO does seem highly sensitive to the exposure setting used when acquiring the image, with a 45% difference between standard exposure and underexposure.

Saturation

Due to the saturating nature of indirect methods, there is a limit above which no estimation of L_e can be made. Especially for dense tropical forests, this could be a problem. In the review of Jonckheere *et al.* (2004) an asymptotic saturation level around 5 for LAI is reported. In this study, a much higher saturation level is found for L_e using ECOM, with a value of 12. All obtained values are well below this level.

From the values obtained during clearcut experiments in Masako, it is shown that often the subsequent images cannot differentiate between a state when a particular tree is present and a new state when it is cut down. Although these trees were rather small and thus a small difference in L_e is expected, this does indicate a form of saturation.

Clumping

Clumping is the deviation from the assumption of random distribution of the foliage in the canopy. Because of aggregation of foliage at different levels (e.g. roots, branches, crown), the resulting gap

fraction is larger than would be the case in a random leaf distribution which leads to an underestimation of the derived LAI (Chen and Black, 1992; Bréda, 2003). The graph of the gap fraction distributions (Figure 15) illustrates that leaves are far from randomly distributed within the field of view of the hemispherical image. Additionally, a single clumping factor cannot be assigned to correct for the deviation from randomness since different distributions are found at different measurement locations. This is due to the frequent and irregular presence of canopy gaps with different sizes and shapes, and the high species diversity in tropical rainforest (Richards, 1996).

The assessment of a clumping factor for every measurement location should greatly improve the results and is especially an important factor to estimate in tropical rainforest due to the heterogeneity of the stand. The clumping factor must be estimated independently from the used methodology (Trichon *et al.*, 1998). A clumping analysis can be done using TRAC, since this instrument not only measures gap fraction but also gap size distribution. This instrument is easy to use in the field (hand held) and is already validated in several studies (see review of Weiss *et al.*, 2004).

Light extinction coefficient

In this study, the empirical values used to describe the light extinction coefficient are not determined for the study sites, but simply taken on from the study of Juárez *et al.* (2009) in a tropical rain forest in an Amazon forest site located in the Tapajós National Forest. This is only an approximation and proper measurements of light extinction should be taken if this methodology is repeated. A light extinction coefficient is site- and species-specific due to leaf angle, shape of the leaf, clumping, etc. (Jonckheere *et al.*, 2004).

LAI estimation

The actual objective is still the determination of LAI, since it is a more useful parameter in climate studies than L_e . For the derivation of LAI out of the calculated L_e , there is a need for additional parameters, namely a clumping factor and a WAI. As discussed above, not accounting for clumping causes an underestimation of the estimated LAI, but the inclusion of nonphotosynthetically active elements in the images causes an overestimation. It is difficult to assess the projection area of stems and branches in tropical rainforest and information from literature is scarce (Wirth *et al.*, 2001). The predominant factor is not determined, although it is presumed that clumping is more important.

5.1.2 Factors during image acquisition

From this study, a straightforward exposure setting cannot be recommended. The underexposed images result in L_e values that are on average 25% higher than the values computed with standard exposed images, and 45% lower for CO values. Simply due to the higher values of L_e and lower of CO computed from underexposed images, these values seem more realistic and more closely resemble the expected values for this type of forest (see start of this discussion), although the relative values of the standard exposed images can just as easily be interpreted. Zhang *et al.* (2005) reported that

image acquisition using automatic exposure is not reliable and that for dense canopies the images result in an overestimation of gap fractions and consequently in an underestimation of L_e . That said, the underexposed images have other important practical advantages over the standard exposed images. First, thresholding of the underexposed images is more straightforward since a sharper contrast is visible between sky and vegetation elements. Less deviation is visible for the derived parameters compared to the standard exposed images when they are analysed using different thresholding methods (Figure 10). Furthermore, from the replication of manual thresholding, it is clear that a threshold selection for an underexposed image is more obvious than for a standard exposed image and consequently more accurately repeatable. Another advantage is that the image acquisition is seemingly less dependent on weather conditions for the underexposed images, although image acquisition during sunny weather conditions is not recommended. Standard protocols for hemispherical canopy photography should be established. This protocol should also provide for adjustments depending on the type of vegetation studied, for example recommended exposure settings, height of camera for image acquisition, and auxiliary information and instrumentation needed.

5.1.3 Analysis of the images

One of the main problems in image processing reported in literature is the accurate thresholding of the image (Jonckheere *et al.*, 2005). In this study, three thresholding methods are compared. It is not a matter of selecting a correct thresholding method, because no standard binary image can be produced. The suitability of the threshold value can only be determined by visually comparing the binary image with the original image.

Selection of the appropriate software for this study depended on a single major factor, namely the amount of time available for image analysis. Due to the large amount of images that needed to be analysed, automating the process was the only way to complete the analysis in time. The ECOM was consequently used for the overall image analysis. A disadvantage though is the lack of visual control of the created binary image. The user cannot assess if the thresholding of the image is done realistically and consequently cannot know the reliability of the derived structural parameters. In this study, three ways of assessment of the results are used. First, three images taken on the same measurement location at the same time, are separately analysed and the results are compared. Next, the comparison with the two other thresholding methods – manual thresholding and edge detection – provides an idea of the robustness of the results. Finally the derived L_e is compared to LAI determined with direct measurements in clearcut experiments in transition forest.

First of all, using ECOM, an overall relative standard deviation of only 3% of the derived L_e is found for the three images acquired at the same measurement location, indicating the consistency of results.

Secondly, it can be stated that overall the three thresholding methods produce significantly different results. The selected threshold units themselves vary, resulting in the production of varying binary images and consequently different structural parameters are derived. This assessment leads to the fact that a single fixed structural parameter cannot be derived and this has to be kept in mind during interpretation of the results. From the scatterplots in Figures 9 and 10, it can be observed that the selection of the threshold unit rather than the parameters derived plays a role, since the parameter

values are closer to the 1:1 line than the threshold units, although they still differ significantly. The parameters overall also differed less significantly after averaging them per measurement location. This shows that it is better to rely on several images for one measurement location since they result in more 'stable' parameters.

Finally, the comparison with LAI from the direct measurement should provide a correct validation of the estimates of L_e from the applied indirect methodology. The parameter $L_e(60^\circ)$ is best for comparison with the direct LAI, since in both parameters the understory is not taken into account. Unfortunately, a relation between the two cannot be determined (Figure 11) because of several problems. First of all, during the clearcut experiments, lianas were not included in the measurement causing an underestimation of the LAI. For example, Clark *et al.* (2008) reported lianas contributing 12.1% to the total LAI in a primary forest site in Costa Rica. In the study sites, an assessment of the percentage contributed by lianas is not made. Since large variations in liana density exist among different sites (DeWalt *et al.*, 2010), a constant factor of underestimation of direct LAI over the different plots cannot be assigned. Secondly, the derivation of the direct LAI is based on the obtained SLA of every tree, but since this could not be done for all individuals, SLA of a tree of the same species was used. The adoption of a single SLA will also cause small deviations. Next, the direct LAI is calculated as the total leaf area divided by the ground area of the clearcut site. The projected ground area also contains errors since the crown of trees at the edges fall out of the actual clearcut site. This effect will be compensated by crowns of trees outside the site leaning in, although the predominant direction is not known. For the indirect method, the largest problem is the transformation of L_e to LAI. More site-specific parameters are necessary to make a more accurate estimation. This was discussed in section 5.1.1.

A last remark concerning image analysis is the choice of the colour channel which has the largest contrast between vegetation elements and sky and consequently is most suitable for thresholding. In this study, the blue channel is selected which is also the channel most often recommended in literature, although other selections have been made. For example Jonckheere *et al.* (2005) choose to analyse the true colour image after comparison with the blue channel image. They concluded that when an image is overexposed by the sun, the overexposed leaves are more clear in the true colour image. Note that with the ECOM script used in this study (Appendix 2), it is not possible to analyse more than one channel.

Although uncertainties concerning the reliability of the results remain, they are still useful as a comparative tool, not only inside a single plot but also between different sites. Comparison of (relative) values of structural parameters is possible due to the consistency of the applied methodology.

5.2 Part 2: Spatial variability of canopy structure

From the above discussion related to the reliability of the parameters derived from hemispherical canopy photography, $L_e(60^\circ, ue)$ and $CO(\%, ue)$ are selected as the most appropriate structural parameters in this study. The underexposed images are selected to provide overall more reliable results. $L_e(60^\circ)$ is retained to exclude the understory and characterize only the canopy structure. CO is included since it is an appropriate variable for characterizing light availability at the forest floor.

5.2.1 Spatial dependency and sampling scheme

From the theoretical variogram models in Figures 18 and 19, it is difficult to determine if spatial dependency between the structural parameters actually exists. Some variograms are very close to a pure nugget effect (no spatial dependency), although the points at the smallest lags from the experimental variograms (red points) are generally smaller than the sill and suggest that a spatial dependency may exist at smaller distances. In literature, spatial dependency in tropical forests has been described. For example Nicotra *et al.* (1999) demonstrated spatial dependence of light availability in primary and transition forest in Costa Rica with ranges for CO around 25-29m for both stand types. Spatial dependence of LAI of up to 11m was assessed in transition forest and a range of 25m was found for primary forest. In this study, the smallest lag assessed was 25m and no actual statement can be made on spatial dependency below this distance.

This shows that the applied sampling scheme did not comply with conditions necessary for a precise study on spatial dependency. A more efficient way to sample would be to distribute pairs of measurement locations at different distances and decreasing the number of redundant measurements with a constant distance between measurement locations (Burrows *et al.*, 2002).

The location maps showing the measurement locations and the obtained values of the structural parameters are useful to show the horizontal macrostructure of the forest. This map is also very accurate, since the relative standard deviation of every sample value is 3%. The interpolation maps are a lot less reliable since the spatial dependency is not determined for small distances. The reliability and coherency of the maps will improve if more measurements are made at varying distances. In this study, they do provide a visually more interpretable map than the location maps alone, and show what result is possible with these kind of measurements (for further research).

Maps of CO are a useful document for forest dynamics studies, since they are closely related to spatial distribution of radiation (Trichon *et al.*, 1998) and because light is an important factor limiting growth and survival of many forest species, and its distribution may affect regeneration patterns (Nicotra *et al.*, 1999).

5.2.2 Intra-site variability

The location maps of L_e emphasize the spatial heterogeneity of the forest structure. The variability of the parameter within one plot is large with for example a range of $L_e(60^\circ, ue)$ between 2.6 and 6.9 in YOK/I and a coefficient of variation of 19%. The interpolation maps allow for a clearer view of the area and its structural variability, but a considerable averaging of the observed values occurs due to the applied interpolation, although a high heterogeneity remained even after this averaging effect.

A highly significant negative correlation is found between L_e and CO, indicating a spatial correlation between canopy structure and light availability, as was also observed by e.g. Nicotra *et al.* (1999).

This study took place in the dry season. According to Wirth *et al.* (2001), who, in addition to spatial variability also studied temporal variability of canopy structure in a tropical moist semideciduous forest, changes in mean LAI between wet and dry season are small but significant. De Wasseige *et al.* (2003) also studied seasonal variation in a semideciduous forest in the Central African Republic and determined a decrease in foliage during the dry season of 0.34 for LAI. This indicates that it is possible that slightly higher values of L_e will be found in the wet season. Research of seasonal variability would be very interesting and provide a considerable added value for this type of study.

5.2.3 Inter-site variability

The comparison of the means of all the different plots in primary forest showed a high overall similarity of the structural parameters. Between YOK/I and YOK/II, this could be expected since the plots are only 650m apart and characteristics of the site are similar (soil, topography). When comparing these two plots with YAN/I, which is 108km further, on the other side of the Congo river, no significant difference is found. Site characteristics of Yangambi and Yoko are presumed to be quite similar, since the soils of the areas are similar, as is the topography, and the difference in elevation between the sites is less than 20m. However this is based on literature descriptions and not verified by a field assessment. Slight changes in soil composition, elevation, rainfall, and temperature can contribute to spatial differences in forest structure (Chapman *et al.*, 1997), and a more detailed site description could reveal some differences. A difference was assessed between YOK/II and YOK/III for the parameters $L_e(75^\circ, st)$ and CO(% , st) which could be the result of the difference in topography. Since no difference is found for $L_e(60^\circ, st)$ and for all parameters derived from the underexposed images, no statement can be made.

The characteristics used to compute the variogram models of the different plots should give an idea of the spatial dependency of the structural parameters. The comparison of the ranges assessed for the different plots shows the difference in variability of the structural parameters, but since the variograms are not reliable due to the applied sampling scheme, no statement can be based on these characteristics.

Significant differences are found between primary forest and transition forest. Larger average percentage of CO is obtained in transition forest, indicating more light availability compared to primary forest. L_e in transition forest is also smaller.

6 Conclusion

Hemispherical canopy photography on its own is not sufficient for the assessment of LAI in tropical rainforests due to the assumptions that need to be made for its derivation. The method is sensitive enough for the wide range of LAI values, from newly formed gaps to mature forest stages. Therefore hemispherical photography could give accurate results when it is used in combination with another instrument to obtain the auxiliary information needed for the derivation of LAI, with the emphasis on an estimation of clumping. This will not be a straightforward task because of the high heterogeneity of the forest and its dynamics. Additionally, accurate values of the extinction coefficient should be measured when this method is repeated. Hemispherical canopy photography can be used to provide good estimations of CO without additional information, and give an indication of light availability at the forest floor.

All selected sites in primary forest were similar with respect to elevation, soil characteristics and appearance, and no significant differences are found between structural parameters of the different plots, both at local and regional scale. Overall, a mean of 4.0 for $L_e(60^\circ, ue)$ is found, with values ranging between 2.6 and 7.4, and a mean of 3.0% CO ranging between 1.1% and 6.4%. A difference is obtained between primary and transitional forest, with transition forest having an overall lower L_e and higher CO.

Suggestions for further research

During this study, some shortcomings were encountered concerning the methodology. Some suggestions for further research are listed:

- The assessment of the distribution of leaves within the canopy using an independent instrument, for example TRAC, would greatly improve reliability of the results.
- The light extinction coefficient should be accurately measured since it is site-specific.
- A presurvey concerning optimal exposure settings should be made, since it is shown that this setting produces significantly different results. Underexposure is recommended for closed canopies.
- Direct measurements are necessary to validate the indirect methodology of hemispherical canopy photography in tropical rainforest until it is optimized.
- The regular grid sampling scheme is not optimal to assess spatial dependency of the canopy structure within a single plot. More efficient would be to distribute pairs of measurement locations at different distances.
- A topic in itself would be to provide a detailed protocol for hemispherical canopy photography in tropical rainforest.

7 References

- Aguilar-Amuchastegui, N., Henobry, G.M. (2006). Monitoring sustainability in tropical forests: how changes in canopy spatial pattern can indicate forest stands for biodiversity surveys. *IEEE Geoscience and Remote Sensing Letters* 3, 329 - 333.
- Asner, G., Scurlock, J., Hicke, J. (2003). Global synthesis of leaf area index observations: implications for ecological and remote sensing studies. *Global Ecology & Biogeography* 12, 191 - 205.
- Badjoko, D.H. (2009). Etudes de la structure des émergents et dominants dans le bloc sud du dispositif de la réserve forestière de la Yoko. Université de Kisangani, Faculté des sciences. 68 p.
- Black, T.A., Chen, J.M., Lee, X., Sagar, R.M. (1991). Characteristics of shortwave and longwave irradiances under a Douglas-fir forest stand. *Can. J. Forest Res.* 21, 1020 - 1028.
- Bonhomme, R., Varlet-Grancher, C., Oldeman, R.A.A. (1974). Mesures préliminaires des rayonnements solaires au-dessus et à l'intérieur de la forêt guyanaise. Note interne, INRA Bioclimatologie. 14 p.
- Brando, P.M., Nepstad, D.C., Davidson, E.A., Trumbore, S.E., Ray, D., Camargo, P. (2008). Drought effects on litterfall, wood production and belowground carbon cycling in an Amazon forest: results of a throughfall reduction experiment. *Philosophical Transactions of Royal Society B* 363, 1839 - 1848.
- Bréda, N. (2003). Ground-based measurements of leaf area index: a review of methods, instruments and current controversies. *Journal of Experimental Botany* 54, 2403 - 2417.
- Buggenhout, L. (2011). Carbon stocks in aboveground biomass of tropical forests in Yoko, Masako and Yangambi (DR Congo). Ghent University, Faculty of Bioscience Engineering, Laboratory of Plant Ecology, Masterthesis.
- Burrows, S.N., Gower, S.T., Clayton, M.K., Mackay, D.S., Ahl, D.E., Norman, J.M., Diak, G. (2002). Application of Geostatistics to characterize leaf area index (LAI) from flux tower to landscape scales using a cyclic sampling design. *Ecosystems* 5, 667 - 679.
- Chapman, C.A., Chapman, L.J., Wrangham, R., Isabirye-Basuta, G., Ben-David, K. (1997). Spatial and temporal variability in the structure of a tropical forest. *Afr. J. Ecol.* 35, 287 - 302.
- Chazdon, R.L., Fetcher, N. (1984). Photosynthetic light environments in a lowland tropical rain forest in Costa Rica. *Journal of Ecology* 72, 553 - 564.
- Chen, J.M., Black, T.A. (1992). Defining leaf area index for non-flat leaves. *Plant, Cell and Environment* 15, 421 - 429.
- Ciais, P., Bombelli, A., Williams, M., Piao, S.L., Chave, J., Ryan, C.M., Henry, M., Brender, P., Valentini, R. (2011). The carbon balance of Africa: synthesis of recent research studies. *Philosophical Transactions of the Royal Society B*. in press.

- Clark, D.B., Olivas, P.C., Oberbauer, S.F., Clark, D.A., Ryan, M.G. (2008). First direct landscape-scale measurement of tropical rain forest Leaf Area Index, a key driver of global primary productivity. *Ecology Letters* 11, 163 - 172.
- De Wasseige, C., Bastin, D., Defourny, P. (2003). Seasonal variation of tropical forest LAI based on field measurements in Central African Republic. *Agricultural and Forest Meteorology* 119, 181 - 194.
- De Wasseige, C., Devers, D., de Marcken, P., Eba'a Atyi, R., Nasi, R., Mayaux, Ph. (2009). The Forests of the Congo Basin - State of the Forest 2008, Luxembourg: Publications Office of the European Union, ISBN 978-92-79-13210-0, doi: 10.2788/32259.
- De Wulf, R. (1992). Optical remote sensing methods for agricultural crop growth monitoring and yield production. Universiteit Gent, Faculteit van de landbouwwetenschappen, Doctoraatsthesis. 263 p.
- DeWalt, S.J., Schnitzer, S.A., Chave, J., Bongers, F., Burnham, R.J., Cai, Z., Chuyong, G., Clark, D.B., Ewango, C.E.N., Gerwing, J.J., Gortaire, E., Hart, T., Ibarra-Manriquez, G., Ickes, K., Kenfack, D., Macia, M.J., Makana, J.-R., Martinez-Ramos, M., Mascaro, J., Moses, S., Muller-Landau, H.C., Parren, M.E.P., Parthasarathy, N., Perez-Salicrup, D.R., Putz, F.E., Romero-Saltos, H., Thomas, D. (2010). Annual rainfall and seasonality predict pan-tropical patterns of liana density and basal area. *Biotropica* 42, 309 - 317.
- Doughty, C.E., Goulden, M.L. (2008). Seasonal patterns of tropical forest leaf area index and CO₂ exchange. *Journal of Geophysical Research* 113, G00B06, doi:10.1029/2007JG000590.
- Engelbrecht, B., Herz, H. (2001). Evaluation of different methods to estimate understorey light conditions in tropical forests. *Journal of tropical ecology* 17, 207 - 224.
- Evans, G.C., Coombe D.E. (1959). Hemispherical and woodland canopy photography and the light climate. *Journal of Ecology* 47, 103 - 113.
- FAO (2010). Global Forest Resource Assessment 2010, Main report. Food and Agricultural Organization of the United Nations. Rome, 2010. ISBN 978-92-5-106654-6. 340 p.
- Fassnacht, K.S., Gower, S.T., Norman, J.M., McMurtrie, R.E. (1994). A comparison of optical and direct methods for estimating foliage surface area index in forests. *Agricultural and Forest Meteorology* 71, 183 - 207.
- Frazer, G.W., Canham, C.D., Lertzman, K.P. (1999). Gap light analyzer (GLA), Version 2.0: Imaging software to extract canopy structure and gap light transmission indices from true-colour fisheye photographs, users' manual and program documentation. Burnaby, BC, Canada: Simon Fraser University. 36 p.
- Frazer, G.W., Fournier, R.A., Trofymowc, J.A., Hall, R.J. (2001). A comparison of digital and film fisheye photography for analysis of forest canopy structure and gap light transmission. *Agricultural and Forest Meteorology* 109, 249 - 263.
- Gilson, P., Van Wambeke, A., Gutzwiller, R. (1956). Carte des sols et de la végétation du Congo belge et du Ruanda-Urundi. Yangambi (Planchette 2 : Yangambi). Notice explicative de la carte des sols et

de la végétation. Publications de l'institut national pour l'étude agronomique du Congo belge (I.N.E.A.C.). 33 p.

Grubb, P.J., Whitmore, T.C. (1967). A comparison of montane and lowland forest in Ecuador III. The light reaching the ground vegetation. *Journal of Ecology* 55, 33 - 57.

Hill, R. (1924). A lens for whole sky photographs. *Quarterly Journal of the Royal Meteorological Society* 50, 227 - 235.

Jarčuška, B. (2008). Methodological overview to hemispherical photography, demonstrated on an example of the software GLA. *Folia oecologica* 35, 66 - 69.

Jennings, S.B., Brown, N.D., Shiel, D. (1999). Assessing forest canopies and understorey illumination: canopy closure, canopy cover and other measures. *Forestry* 72, 59 - 73.

Jonckheere, I., Fleck, S., Nackaerts, K., Muys, B., Coppin, P., Weiss, M., Baret, F. (2004). Review of methods for in situ leaf area index determination. Part I. Theories, sensors and hemispherical photography. *Agricultural and Forest Meteorology* 121, 19 - 35.

Jonckheere, I., Nackaerts, K., Muys, B., Coppin, P. (2005). Assessment of automatic gap fraction estimation of forests from digital hemispherical photography. *Agricultural and Forest Meteorology* 132, 96 - 114.

Jonckheere, I. (2007). Hemispherical canopy photography: some acquisition guidelines. (unpublished).

Juárez, R.I.N., Rocha, H.R., Figueira, A. M.S., Goulden, M.L., Miller, S.D. (2009). An improved estimate of leaf area index based on the histogram analysis of hemispherical photographs. *Agricultural and Forest Meteorology* 149, 920 - 928.

Lee, K.S., Kim, S.H., Park, J.H., Kim, T.G., Park, Y.I., Woo, C.S. (2006). Remote sensing estimation of forest LAI in close canopy situation. *Kor. J. Rem. Sen.* 22, 305 - 311.

Leigh, E.G. (1999). Tropical forest ecology: A view from Barro Colorado Island, Oxford University Press, New York, Oxford.

Malhado, A., Costa, M., de Lima, F., Portilho, K., Figueireda, D. (2009). Seasonal leaf dynamics in an Amazonian tropical forest. *Forest Ecology and Management* 258, 1161 - 1165.

Martinez, B., Cassiraga, E., Camacho, F., Garcia-Haro, J. (2010). Geostatistics for mapping leaf area index over cropland landscape: efficiency sampling assessment. *Remote Sensing* 2, 2584 - 2606.

Matheron, G. (1963). Principles of geostatistics. *Economic Geology* 58, 1246 - 1266.

McWilliam, A.L.C., Roberts, J.M., Cabral, O.M.R., Leitao, M.V.B.R., de Costa, A.C.L., Maitelli, G.T., Zamparoni, C.A.G.P. (1993). Leaf area index and above-ground biomass of terra firme rain forest and adjacent clearings in Amazonia. *Functional Ecology* 7, 310 - 317.

Meir, P., Grace, J., Miranda, A. (2000). Photographic method to measure the vertical distribution of leaf area density in forests. *Agricultural and Forest Meteorology* 102, 105 - 111.

- Myneni R.B, Yanga, W., Nemani, R.R., Huete, A.R., Dickinson, R.E., Knyazikhina, Y., Didand, K., Fue, R., Juárez, R.I.N., Saatchi, S.S., Hashimoto, H., Ichii, K., Shabanova, N.V., Tana, B., Ratanad, P., Privette, J.L., Morisette, J.T., Vermote, E.F., Royo, D.P., Wolf, R.E., Friedl, M.A., Running, S.W., Votava, P., El-Saleous, N., Devadigar, S., Sua, Y., Salomonson, V.V. (2007). Large seasonal swings in leaf area of Amazon rainforests. *Proc. Natl Acad. Sci. USA*. 104, 4820 - 4823.
- Nicotra, A.B., Chazdon, R.L., Iriarte, S.V.B. (1999). Spatial heterogeneity of light and woody seedling regeneration in tropical wet forests. *Ecology* 80, 1908 - 1926.
- Nobis, M., Hunziker, U. (2005). Automatic thresholding for hemispherical canopy-photographs based on edge detection. *Agricultural and Forest Meteorology* 128, 243 - 250.
- Nobis, M. (2005): SideLook 1.1 - Imaging software for the analysis of vegetation structure with true-colour photographs; <http://www.appleco.ch>.
- Norman, J.M., Campbell, G.S. (1989). Canopy Structure. In: Pearcy, R.W., Ehleringer, J., Mooney, H.A., Rundel, P.W. (Eds.), *Plant Physiological Ecology. Field Methods and Instrumentation*. Chapman and Hall, London, pp. 301 - 325.
- Nshimba, S.M. (2008). Etude floristique, écologique et phytosociologique des forêts de l'île à Kisangani, R. D. Congo. Thèse de doctorant, ULB, 273 p.
- Ostertag, R. (1998). Belowground effects of canopy gaps in a tropical wet forest. *Ecology* 79, 1294 - 1304.
- Rich, P.M. (1990). Characterizing plant canopies with hemispherical photographs. *Remote Sensing Reviews* 5, 13 - 29.
- Richards, P.W. (1996). *The tropical rain forest: An ecological study*, second edition. Cambridge University Press, Cambridge, UK. 575 pages. ISBN 0-521-42194-2.
- Roberts, J.M., Cabral, O.M.R., Costa, J., da, P., McWilliam, A.L.C., de A. Sa, T.D. (1996). An overview of the leaf area index and physiological measurements during ABRACOS. In: Gash, J.H.C., Nobre, C.A., Roberts, J.M., Victoria, R.L. (Eds.), *Amazonian Deforestation and Climate*. John Wiley & Sons, p. 287 - 306.
- Sahoo, P.K., Slaughter, D.W., Albert, T.A. (1997). Threshold selection using a minimal histogram entropy difference. *Optical Engineering* 36, 1976 - 1981.
- Schneider, D., Schwalbe, E., Maas, H.-G. (2009). Validation of geometric models for fisheye lenses. *Journal of Photogrammetry and Remote Sensing* 64, 259 - 266.
- Scurlock, J.M.O., Asner, G.P., Gower, S.T. (2001). Worldwide historical estimates of leaf area index, 1932-2000. ORNL/TM-2001/268. Oak Ridge National Laboratory, Oak Ridge, USA.
- Sezgin, M., Sankur, B. (2004). Survey over image thresholding techniques and quantitative performance evaluation. *Journal of Electronic Imaging* 13, 146 - 165.
- Sterck, F.J., Bongers, F. (2001). Crown development in tropical rain forest trees: patterns with tree height and light availability. *Journal of ecology* 89, 1 - 13.

- Strahler, A.H., Jupp, D.L.B., Woodcock, C.E., Schaaf, C.B., Yao, T., Zhao, F., Yang, X., Lovell, J., Culvenor, D., Newnham, G., Ni-Meister, W., Boykin-Morris, W. (2008). Retrieval of forest structural parameters using a ground-based lidar instrument. *Can. J. Remote Sensing* 34, 426 - 440.
- Trichon, V., Walter, J.N., Laumonier, Y. (1998). Identifying spatial patterns in the tropical rain forest structure using hemispherical photographs. *Plant Ecology* 137, 227 - 244.
- Toirambe, B.B. (2010). Conduite d'une évaluation de départ de la situation de biodiversité, des impacts des pressions anthropiques sur les ressources naturelles et de la gouvernance environnementale de la Réserve de biosphère de Yangambi. WWF. 198 p.
- Verhegghen, A., Defourny, P. (2010) A new 300 m vegetation map for Central Africa based on multi-sensor times series. Third Recent Advance in Quantitative Remote Sensing, J.A. Sobrino (Ed.), ISBN: 978-84-370-795-5, Publicaciones de la Universitat de Valencia, Valencia, Spain.
- Vierling, L., Wessman, C. (2000). Photosynthetically active radiation heterogeneity within a monodominant Congolese rain forest canopy. *Agricultural and Forest Meteorology* 103, 265 - 278.
- Watson, D.J. (1947). Comparative physiological studies in the growth of field crops. I. Variation in net assimilation rate and leaf area between species and varieties, and within and between years. *Ann. Bot.* 11, 41 - 76.
- Weiss, M., Baret, F., Smith, G.J., Jonckheere, I., Coppin, P. (2004). Review of methods for in situ leaf area index (LAI) determination. Part II. Estimation of LAI, errors and sampling. *Agricultural and Forest Meteorology* 121, 37 - 53.
- Wirth, R., Weber, B., Ryel, R.J. (2001). Spatial and temporal variability of canopy structure in a tropical moist forest. *Acta Oecologica* 22, 235 - 244.
- Zhang, Y., Chen, J.M., Miller, J.R. (2005). Determining digital hemispherical photograph exposure for leaf area index determination. *Agricultural and Forest Meteorology* 133, 166 - 181.

8 Appendix

8.1 Lens distortion

Sigma 4.5mm/F2.8 Fisheye
Lens Distortion

$$Y = 2 f \cdot \sin\left(\frac{\omega}{2}\right)$$

f = 4.4

ω (deg)	Distortion
0.0	0.0
27	0.0%
45	0.0%
63	-0.2%
81	-0.7%
90	-1.4%

8.2 Matlab script: ECOM

8.2.1 L_e calculation

```

% Le75

clear all;
clc;

%*****
%purpose:
%   this software estimates the leaf area index from hemispherical photographs
%   using the following steps, in order:
%   1. gets the histogram for each hemispherical images
%   2. gets the otv following sahuo et al. 1997
%   3. gets the lai using the gap fraction method. norman and cambell 1989
%*****

%=====
% controlers
%=====
%input files
%-----
[imgfiles,bytes,names]=dirr('H:\Hemi\*.jpg','name');
nimg=numel(imgfiles);

% fileout text
%-----
fileID=fopen('lai75_selectieYOKI_green.txt','wt');
fprintf(fileID,'number\timage\tthreshold\tLAI\tCO\tgfd(1)\tgfd(2)\tgfd(3)\tgfd(4)\t
gfd(5)\tgfd(6)\tgfd(7)\tX\tMSE\tk\tTmean\n');

%image dimensions: you must know it
%-----
ncol = 4288;
nfil = 2848;

%effective area (the hemispheric image): you must know it
%-----
ncini = 978;
ncfin = 3281;
nfini = 316;
nffin = 2619;

%leaves clumping factor: you must provide this information
%-----
clfc = 1;

%#####

for im = 1:nimg,

%=====
%1.getting the histograms
%=====
hmin = 20;
hmax = 255;
ptshisto = hmax - hmin + 1;

```

```

blue=image(:,:,3);
b=blue(nfini:nffin,ncini:nctini,:); % effective area of hemispherical image

diameter=nctini-ncini;
straal = (diameter/2);
radius=floor(straal);
xc=1152;
yc=1152;
value=0;
cir = MidpointCircle(radius, diameter, xc, yc, value);

    cc = cir+ b;
    for m = 1:diameter+1,
        for n = 1:diameter+1,
            if ((cc(m,n) ~= b(m,n)))
                cc(m,n) = 0;
            else
                cc(m,n) = b(m,n);
            end
        end
    end

    cc = cc;
end

histo=zeros(1,256);
histo(:)=imhist(cc);
histo=histo(20:256);

%=====
%2.getting the optimal threshold value
%(sahoo and albert 1997, opt. eng. 36(7), 1976-1981
%=====
epixblack = zeros(1,ptshisto);
epixwhite = zeros(1,ptshisto);
dif = zeros(1,ptshisto);

    for t = 1:ptshisto,
        pit = histo/ sum(histo);          % probability of gray-level values.
        piblack = sum(pit(1:t));
        if ((t + 1) == 236)
            piwhite = 0;
        else
            piwhite = sum(pit((t+1):ptshisto));
        end

        piwhite = piwhite;

        % a priori total entropy
        et = entropy(pit(1:ptshisto)); %/pit

        % black pixels entropy
        epixblack(t)= entropy(pit(1:t)/piblack);

        % white pixels entropy
        if (piwhite == 0)
            epixwhite(t) = 0;
        else
            epixwhite(t) = entropy(pit(t+1:ptshisto)/piwhite);
        end

        epixwhite(t) = epixwhite(t);
        dif(t) = (epixblack(t) - epixwhite(t))^2;
    end

difmin = min(dif);
threshold = find(dif == difmin);
threshold = threshold + 21;    % the scale started at 20 )

```

```

%=====
%3.getting the leaf area index by using the gap fraction method
%norman, j.m., and campbell, g.s., 1989. canopy structure.
%in: pearcy r.w., ehlesinger j., mooney h.a. rundel p.w. (editors),
%plant physiological ecology. field methods and
%instrumentation. chapman and hall, london, pp. 301-325
%=====

% LAI (75 degrees) -----

zenith =[10 20 30 40 50 60 70];
naz = numel(zenith);
gfd=zeros(1,naz);

    for i = 1:diameter+1,
        for j = 1:diameter+1,
            if ((b(i,j) >= threshold))
                b(i,j) = 255;
            else
                b(i,j) = 10;
            end
        end
    end

    end
    bb = b;

R = 2*4.4*sin(pi()/4)-0.014*2*4.4*sin(pi()/4);
straal = (diameter/2.0)/ R;
    straal=floor(straal);

for zz = 1:naz ,
    switch zenith(zz)
        case 10
            cir1 = MidpointCircle(floor(straal*R), diameter, xc, yc, value);
            cir2 = MidpointCircle(floor(straal*2*4.4*sin(15*pi()/360)), diameter,
xc, yc, value);
            cir3 = MidpointCircle(floor(straal*2*4.4*sin(5*pi()/360)), diameter,
xc, yc, value);
        case 20
            cir1 = MidpointCircle(floor(straal*R), diameter, xc, yc, value);
            cir2 = MidpointCircle(floor(straal*2*4.4*sin(25*pi()/360)), diameter,
xc, yc, value);
            cir3 = MidpointCircle(floor(straal*2*4.4*sin(15*pi()/360)), diameter,
xc, yc, value);
        case 30
            cir1 = MidpointCircle(floor(straal*R), diameter, xc, yc, value);
            cir2 = MidpointCircle(floor(straal*2*4.4*sin(35*pi()/360)), diameter,
xc, yc, value);
            cir3 = MidpointCircle(floor(straal*2*4.4*sin(25*pi()/360)), diameter,
xc, yc, value);
        case 40
            cir1 = MidpointCircle(floor(straal*R), diameter, xc, yc, value);
            cir2 = MidpointCircle(floor(straal*2*4.4*sin(45*pi()/360)), diameter,
xc, yc, value);
            cir3 = MidpointCircle(floor(straal*2*4.4*sin(35*pi()/360)), diameter,
xc, yc, value);
        case 50
            cir1 = MidpointCircle(floor(straal*R), diameter, xc, yc, value);
            cir2 = MidpointCircle(floor(straal*(2*4.4*sin(55*pi()/360)-
0.001111*2*4.4*sin(55*pi()/360))), diameter, xc, yc, value);

```

```

        cir3 = MidpointCircle(floor(straal*2*4.4*sin(45*pi()/360)), diameter,
xc, yc, value);
        case 60
            cir1 = MidpointCircle(floor(straal*R), diameter, xc, yc, value);
            cir2 = MidpointCircle(floor(straal*(2*4.4*sin(65*pi()/360))-
0.002556*2*4.4*sin(65*pi()/360))), diameter, xc, yc, value);
            cir3 = MidpointCircle(floor(straal*(2*4.4*sin(55*pi()/360))-
0.001111*2*4.4*sin(55*pi()/360))), diameter, xc, yc, value);
        case 70
            cir1 = MidpointCircle(floor(straal*R), diameter, xc, yc, value);
            cir2 = MidpointCircle(floor(straal*(2*4.4*sin(75*pi()/360))-
0.005333*2*4.4*sin(75*pi()/360))), diameter, xc, yc, value);
            cir3 = MidpointCircle(floor(straal*(2*4.4*sin(65*pi()/360))-
0.002556*2*4.4*sin(65*pi()/360))), diameter, xc, yc, value);
        end
        cir4=cir1+cir2+cir3;

        for k = 1:diameter+1,

            for l = 1:diameter+1,

                if ((cir4(k,l) == 5)) %arbitrarily set to 5
                    cir4(k,l) = 0;
                else
                    cir4(k,l) = 5;
                end
            end
        end

        cc = bb-cir4;

        % --- segment of interest
        for m = 1:diameter+1,
            for n = 1:diameter+1,
                if ((cc(m,n) ~= bb(m,n)))
                    cc(m,n) = 0;
                else
                    cc(m,n) = bb(m,n);
                end
            end
        end
        cc = cc;
        end

        %-----getting the gap fraction
        w = sum(sum(cc == 255));
        b1 = sum(sum(cc == 10));
        gf = w / (b1 + w);
        if ((gf == 0.0))
            gf = 0.000005;
        else
            gf = gf;
        end
        gfd(zz) = gf;
    end

    %calculation of lai
    z = tan(zenith * pi / 180.0);
    tr = zeros(1,naz);

    % ----- gap fraction for each az and lai calculation
    tr(:)=gfd(:);

    for k = 1:naz,
        if (tr(k) == 0.0)

```

```

        tr(k) = 99999;
    else
        tr(k) = tr(k);
    end
end
tr = tr;
t = log(tr);
tmean = mean(t);

%----- finding x , norman and campbel, 89-----
a = 0.1;
b = 10;
x = 1;
dx = 0.01;
while (abs(a - b) > dx),
    s1 = 0.0;
    s2 = 0.0;
    s3 = 0.0;
    s4 = 0.0;
    for j = 1:naz,
        tz = z(j);
        kb = sqrt(x^2 + tz^2) / (x + 1.774 * (x + 1.182)^(-0.733));
        dk = (sqrt((x + dx)^2 + tz^2) / ((x + dx) + 1.774 * ((x + dx) + 1.182)^(-
0.733)) - kb);
        s1 = s1 + kb * t(j);
        s2 = s2 + kb * kb;
        s3 = s3 + kb * dk;
        s4 = s4 + dk * t(j);
    end

    f = s2 * s4 - s1 * s3;

    if ((f < 0.0))
        a = x;
    else
        b = x;
    end
    x = (a + b) / 2.0;
end

if ((s2 ~= 0.0))
    l = -s1 / s2;
else
    l = 99999;
end
lai = l / c1fc;

% mse between o measured k and calculated k
sum_erro = 0;
tmeasured = zeros(1,naz);
tcalculated = zeros(1,naz);
difsqrt = zeros(1,naz);
for kk = 1:naz,
    tmeasured(kk) = exp(t(kk));
    tcalculated(kk) = exp(-(sqrt(x^2 + z(kk)^2) / (x + 1.774 * (x + 1.182)^(-
0.733))) * lai);
    difsqrt(kk) = (tcalculated(kk) - tmeasured(kk))^2;
    sum_erro = sum_erro + difsqrt(kk);
end

mse = sqrt(sum_erro / 7);
if ((mse > 1))
    mse = 1;
else
    mse = mse;
end
end

```


8.2.2 Circle and segments description

```
% Draw a circle in a matrix using the integer midpoint circle algorithm
% Does not miss or repeat pixels
% Created by : Peter Bone
% Created : 19th March 2007
```

```
function cir = MidpointCircle(radius, diameter, xc, yc, value)
```

```
xc = int16(xc);
yc = int16(yc);
```

```
x = int16(0);
y = int16(radius);
d = int16(1 - radius);
```

```
cir(diameter+1,diameter+1)=5;
cir(1:diameter+1,1:diameter+1)=5;
```

```
cir(xc, yc+y) = value;
cir(xc, yc-y) = value;
cir(xc+y, yc) = value;
cir(xc-y, yc) = value;
```

```
while ( x < y - 1 )
    x = x + 1;
    if ( d < 0 )
        d = d + x + x + 1;
    else
        y = y - 1;
        a = x - y + 1;
        d = d + a + a;
    end
    cir( x+xc, y+yc) = value;
    cir( y+xc, x+yc) = value;
    cir( y+xc, -x+yc) = value;
    cir( x+xc, -y+yc) = value;
    cir(-x+xc, -y+yc) = value;
    cir(-y+xc, -x+yc) = value;
    cir(-y+xc, x+yc) = value;
    cir(-x+xc, y+yc) = value;
    cir( y+xc, (-x+yc):(x+yc)) = value;
    cir(-x+xc, (-y+yc):(y+yc)) = value;
    cir( x+xc, (-y+yc):(y+yc)) = value;
    cir(-y+xc, (-x+yc):(x+yc)) = value;
    cir( xc, (yc-y):(yc+y)) = value;
end
cir=uint8(cir);
```

8.3 MAS/2010/1: Species

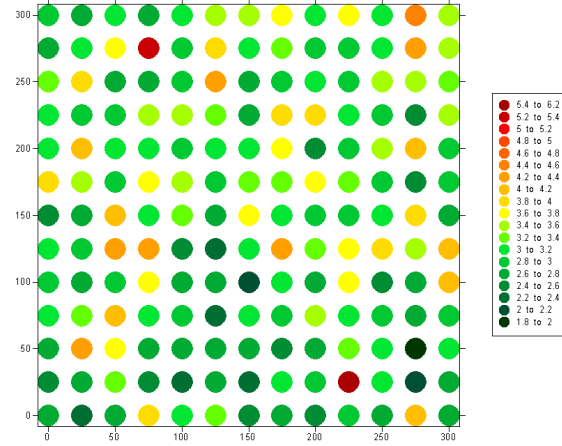
Table: Species of plot MAS/2010/1 and assigned tree number (Buggenhout, 2011).

Tree number	Species	Tree number	Species
1	<i>Musanga cecropioides</i>	27	<i>Morelia senegalensis</i>
2	<i>Harungana madagascariensis</i>	28	<i>Tetrorchidium didymostemon</i>
3	<i>Tetrorchidium didymostemon</i>	29	<i>Macaranga spinosa</i>
4	<i>Oncoba welwitschii</i>	30	<i>Tetrorchidium didymostemon</i>
5	<i>Macaranga saccifera</i>	31	<i>Morelia senegalensis</i>
6	<i>Ricinodendron heudelotii</i>	32	<i>Desplatsia dewevrei</i>
7	<i>Tetrorchidium didymostemon</i>	33	<i>Coelocaryon preussii</i>
8	<i>Macaranga spinosa</i>	34	<i>Dichostemma glaucescens</i>
9	<i>Harungana madagascariensis</i>	35	<i>Musanga cecropioides</i>
10	<i>Tetrorchidium didymostemon</i>	36	<i>Macaranga spinosa</i>
11	<i>Musanga cecropioides</i>	37	<i>Chlamydocola chlamydantha</i>
12	<i>Macaranga spinosa</i>	38	<i>Dichostemma glaucescens</i>
13	<i>Macaranga spinosa</i>	39	<i>Tetrorchidium didymostemon</i>
14	<i>Macaranga spinosa</i>	40	<i>Tetrorchidium didymostemon</i>
15	<i>Berlinia grandiflora</i>	41	<i>Musanga cecropioides</i>
16	<i>Funtumia elastica</i>	42	<i>Tetrorchidium didymostemon</i>
17	<i>Macaranga spinosa</i>	43	<i>Macaranga saccifera</i>
18	<i>Chlamydocola chlamydantha</i>	44	<i>Macaranga spinosa</i>
19	<i>Chlamydocola chlamydantha</i>	45	<i>Cleistopholis patens</i>
20	<i>Morelia senegalensis</i>	46	<i>Macaranga spinosa</i>
21	<i>Thomandersia hensii</i>	47	<i>Tetrorchidium didymostemon</i>
22	<i>Tetrorchidium didymostemon</i>	48	<i>Harungana madagascariensis</i>
23	<i>Chlamydocola chlamydantha</i>	49	<i>Tetrorchidium didymostemon</i>
24	<i>Polyalthia suaveolens</i>	50	<i>Musanga cecropioides</i>
25	<i>Musanga cecropioides</i>	51	<i>Maesopsis eminii</i>
26	<i>Thomandersia hensii</i>		

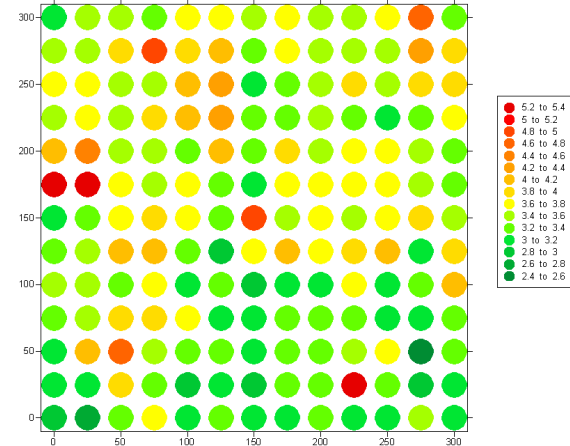
8.4 Location maps

8.4.1 YAN/I

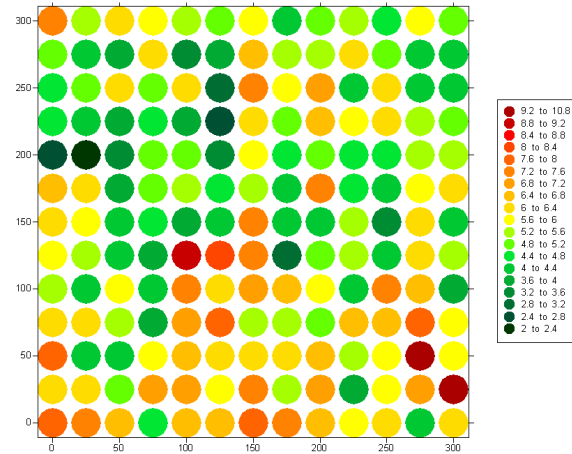
$L_e(60^\circ, \text{st, YAN/I})$



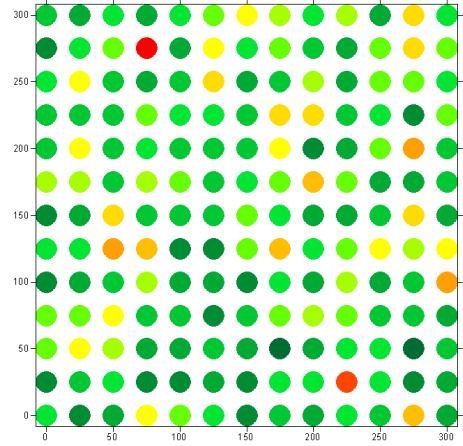
$L_e(75^\circ, \text{st, YAN/I})$



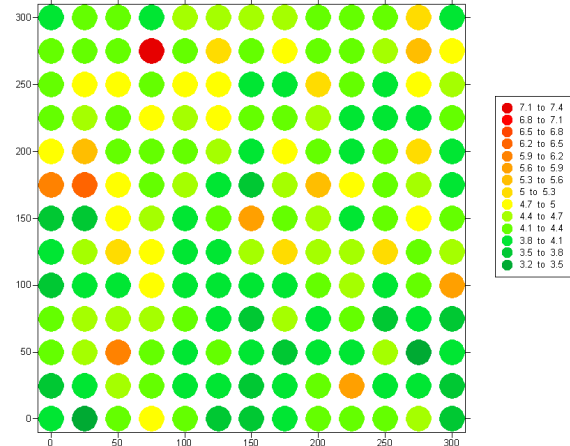
$CO(\%, \text{st, YAN/I})$



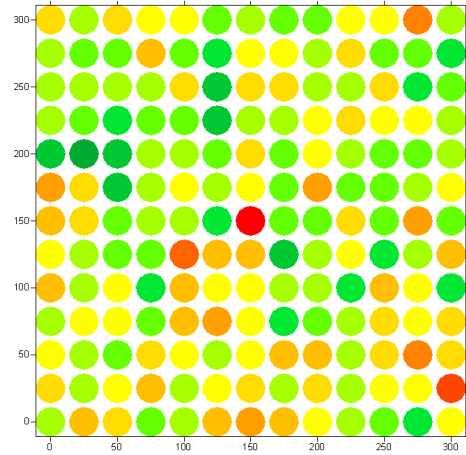
$L_e(60^\circ, ue, YAN/I)$



$L_e(75^\circ, ue, YAN/I)$

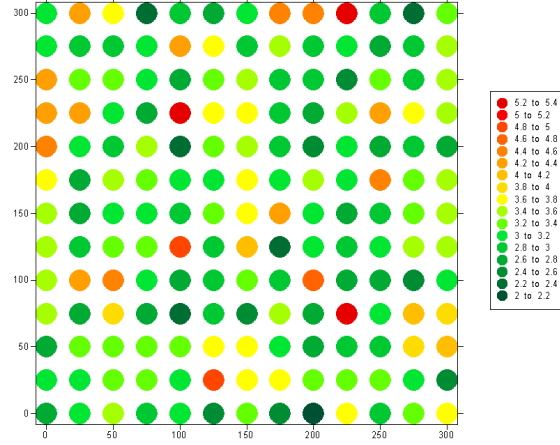


$CO(\%, ue, YAN/I)$

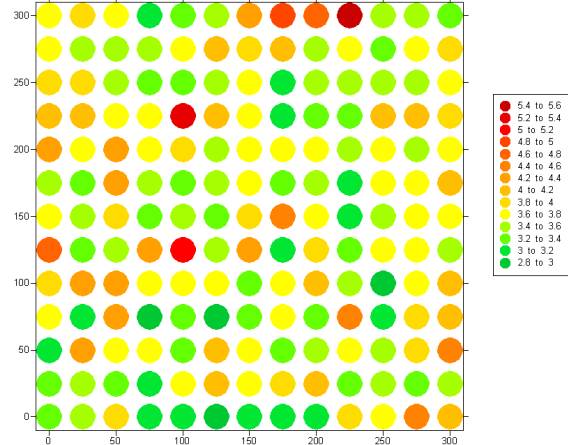


8.4.2 YOK/I

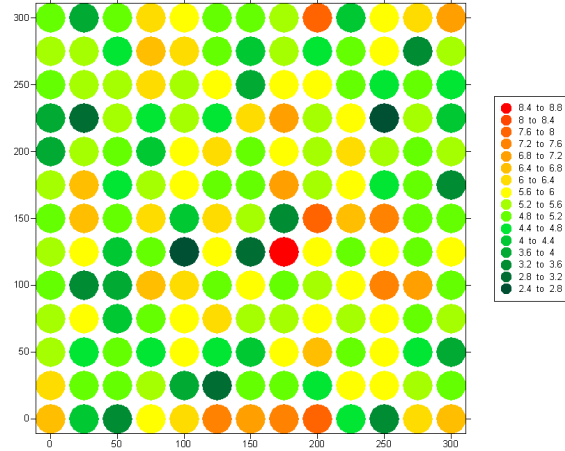
$L_e(60^\circ, \text{st, YOK/I})$



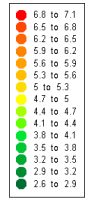
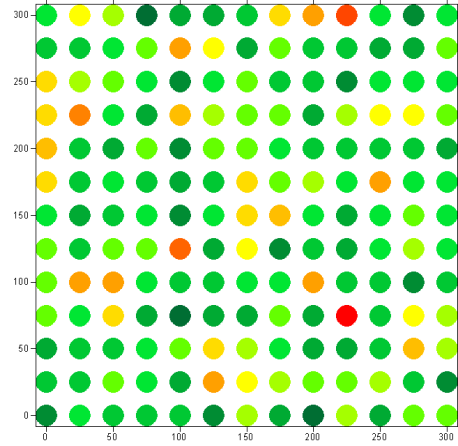
$L_e(75^\circ, \text{st, YOK/I})$



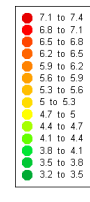
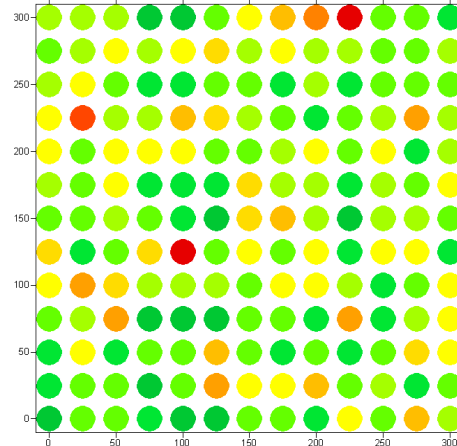
$CO(\%, \text{st, YOK/I})$



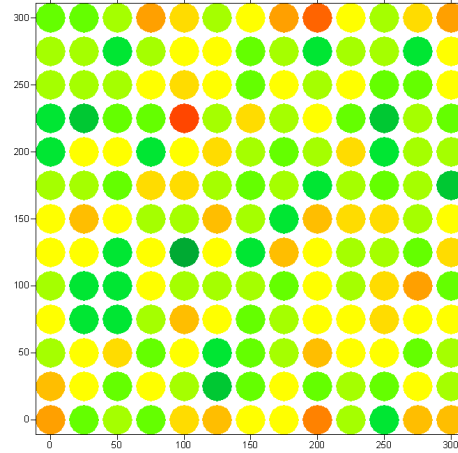
$L_e(60^\circ, ue, YOK/I)$



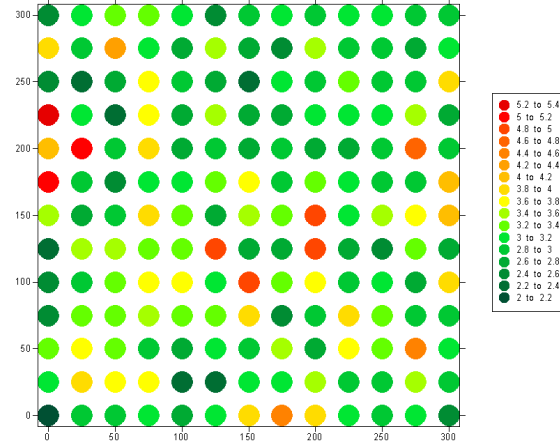
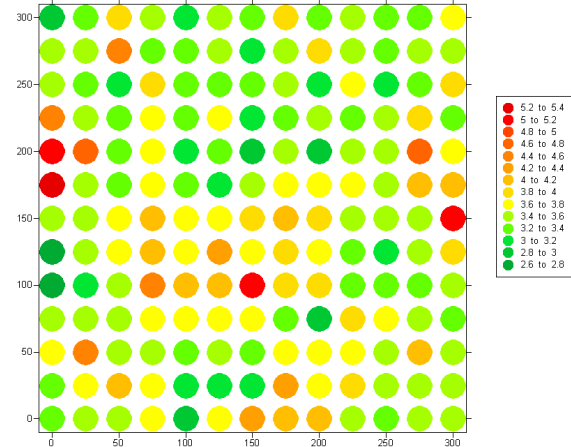
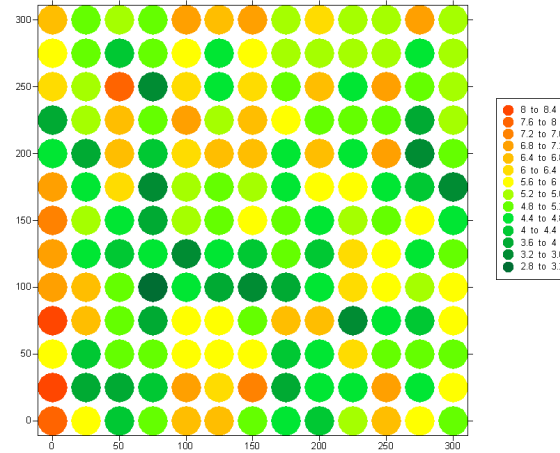
$L_e(75^\circ, ue, YOK/I)$



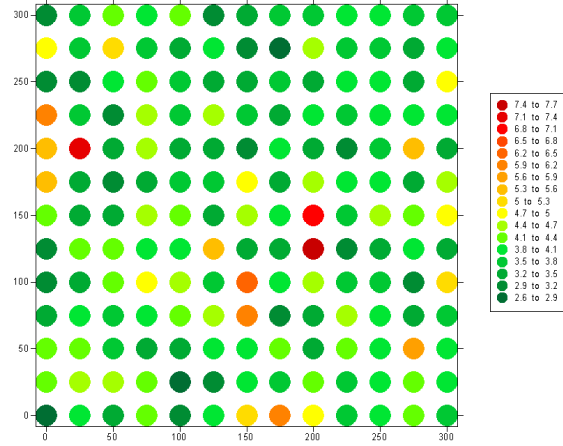
$CO(\%, ue, YOK/I)$



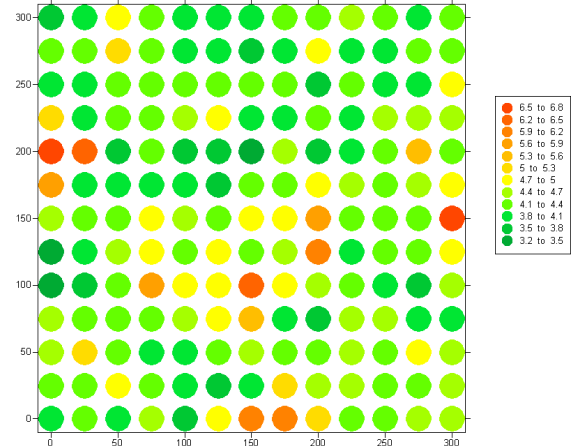
8.4.3 YOK/II

 $L_e(60^\circ, \text{st, YOK/II})$  $L_e(75^\circ, \text{st, YOK/II})$  $CO(\%, \text{st, YOK/II})$ 

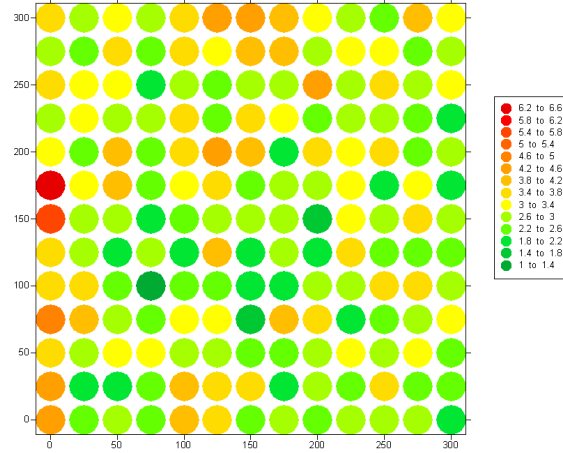
$L_e(60^\circ, ue, YOK/II)$



$L_e(75^\circ, ue, YOK/II)$

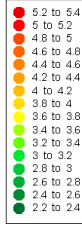
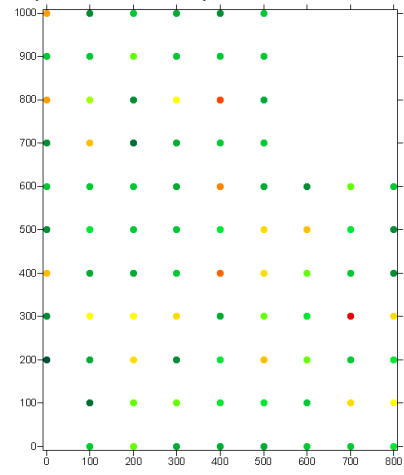


$CO(\%, ue, YOK/II)$

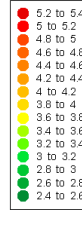
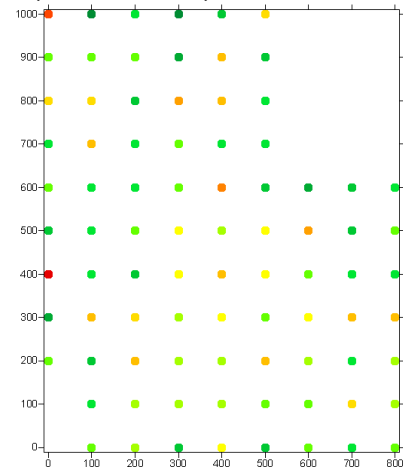


8.4.4 YOK/III

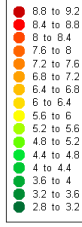
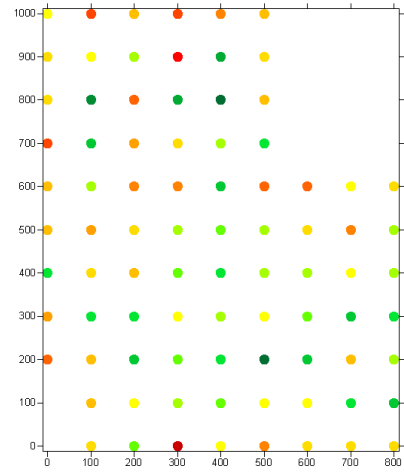
$L_e(60^\circ, \text{st, YOK/III})$



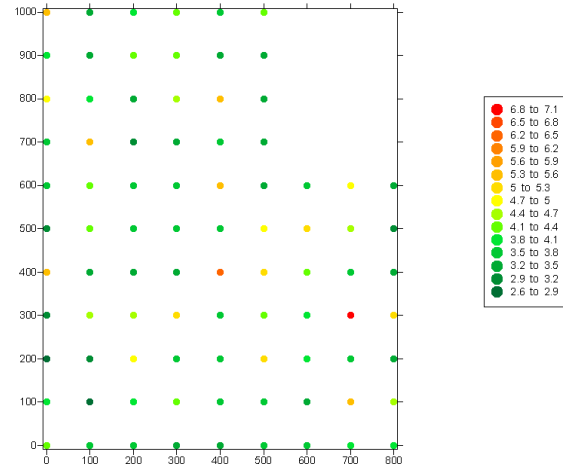
$L_e(75^\circ, \text{st, YOK/III})$



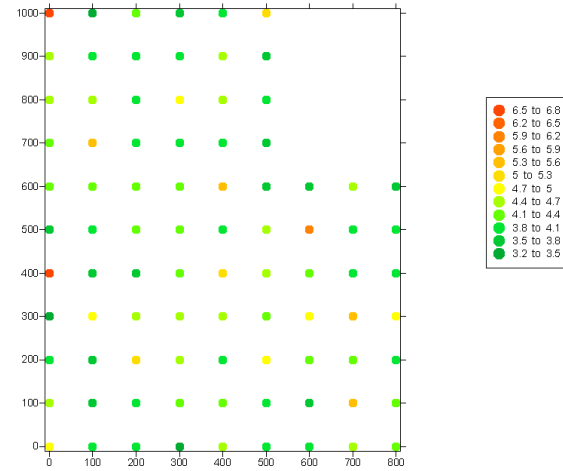
$CO(\%, \text{st, YOK/III})$



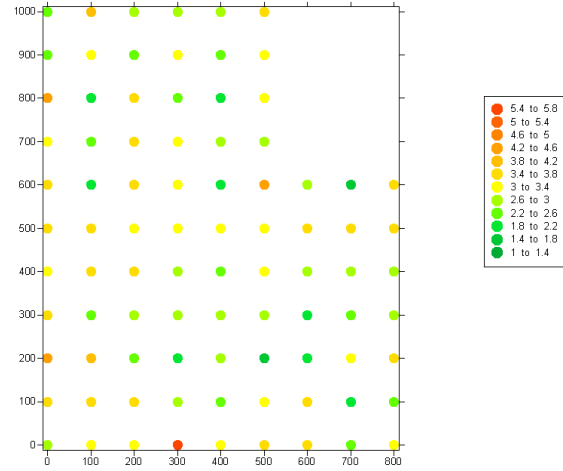
$L_e(60^\circ, ue, YOK/III)$



$L_e(75^\circ, ue, YOK/III)$

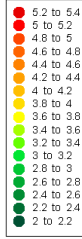
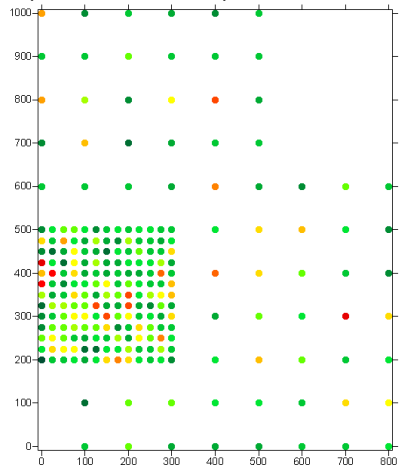


$CO(\%, ue, YOK/III)$

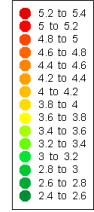
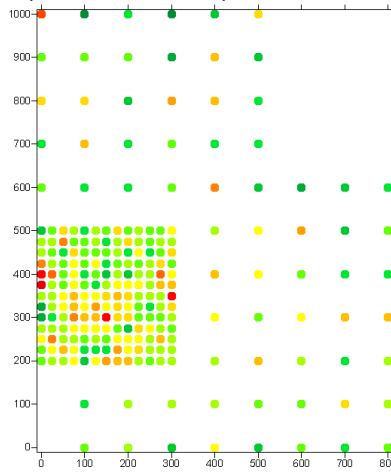


8.4.5 YOK/II/III

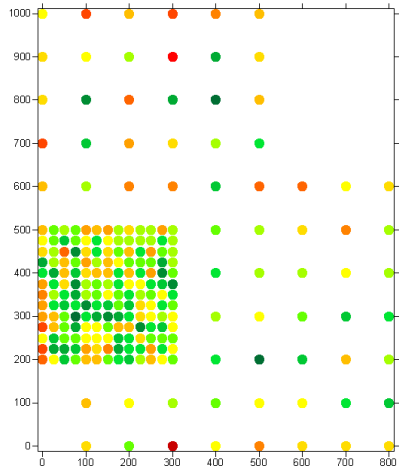
$L_e(60^\circ, \text{st, YOK/II/III})$



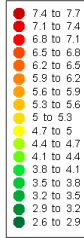
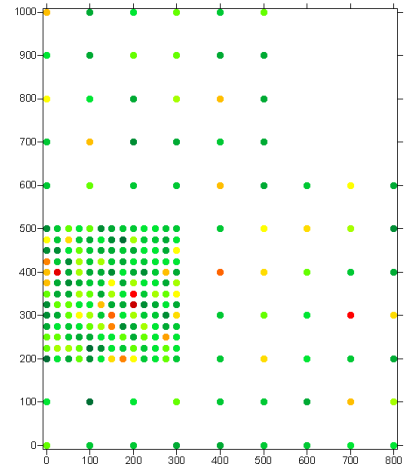
$L_e(75^\circ, \text{st, YOK/II/III})$



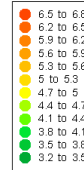
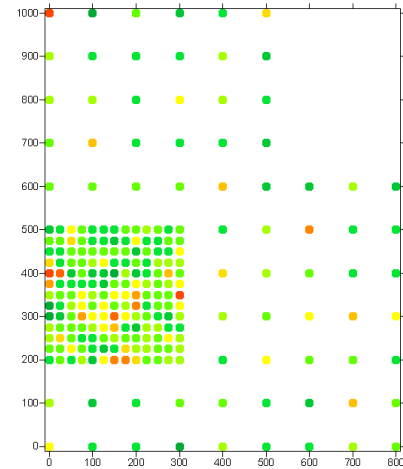
$CO(\%, \text{st, YOK/II/III})$



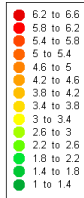
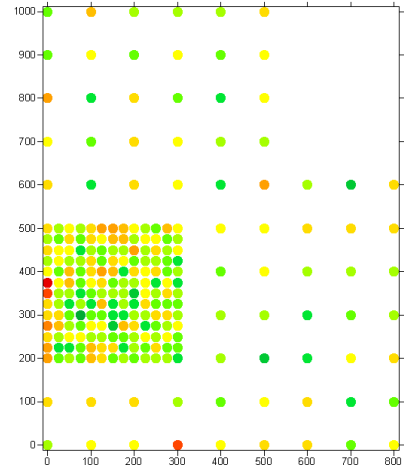
$L_e(60^\circ, ue, YOK/II/III)$



$L_e(75^\circ, ue, YOK/II/III)$



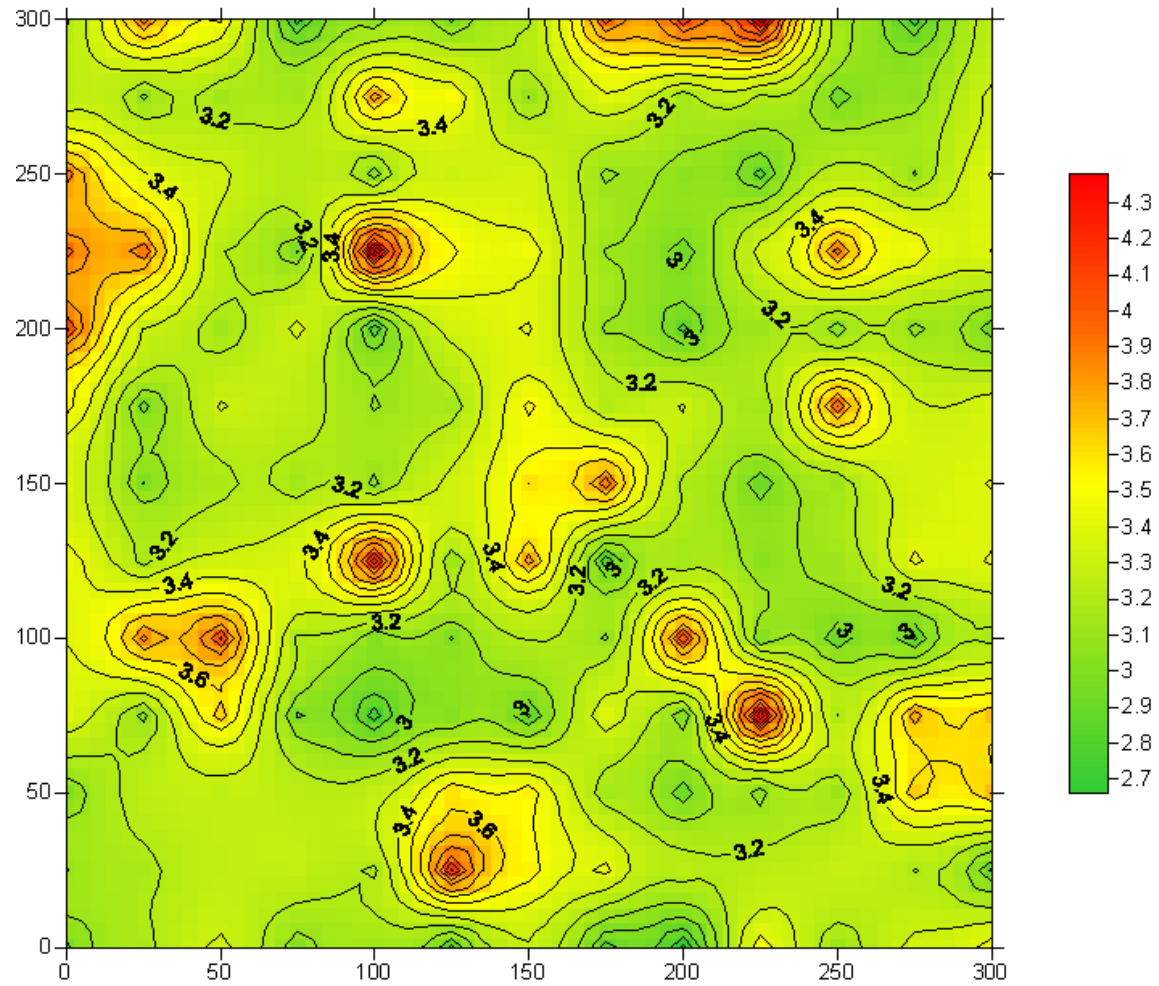
$CO(\%, ue, YOK/II/III)$

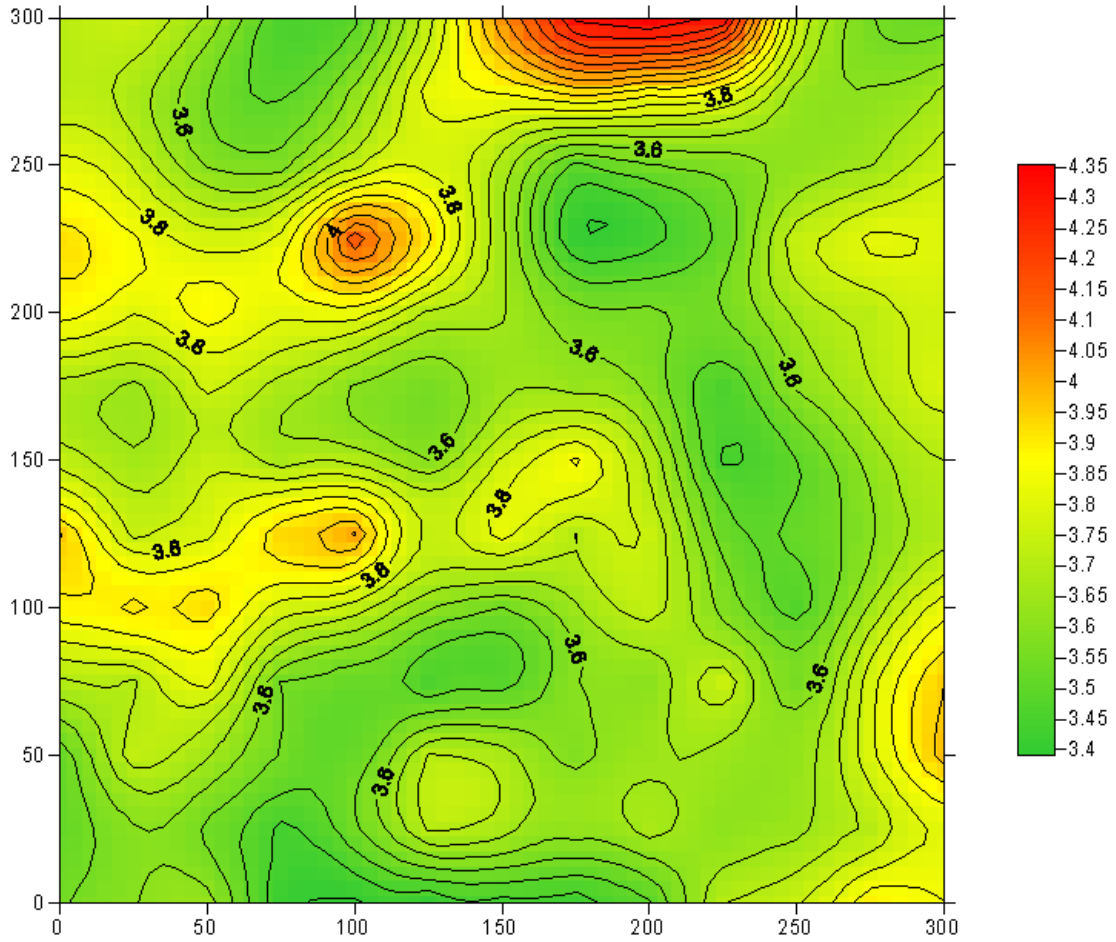


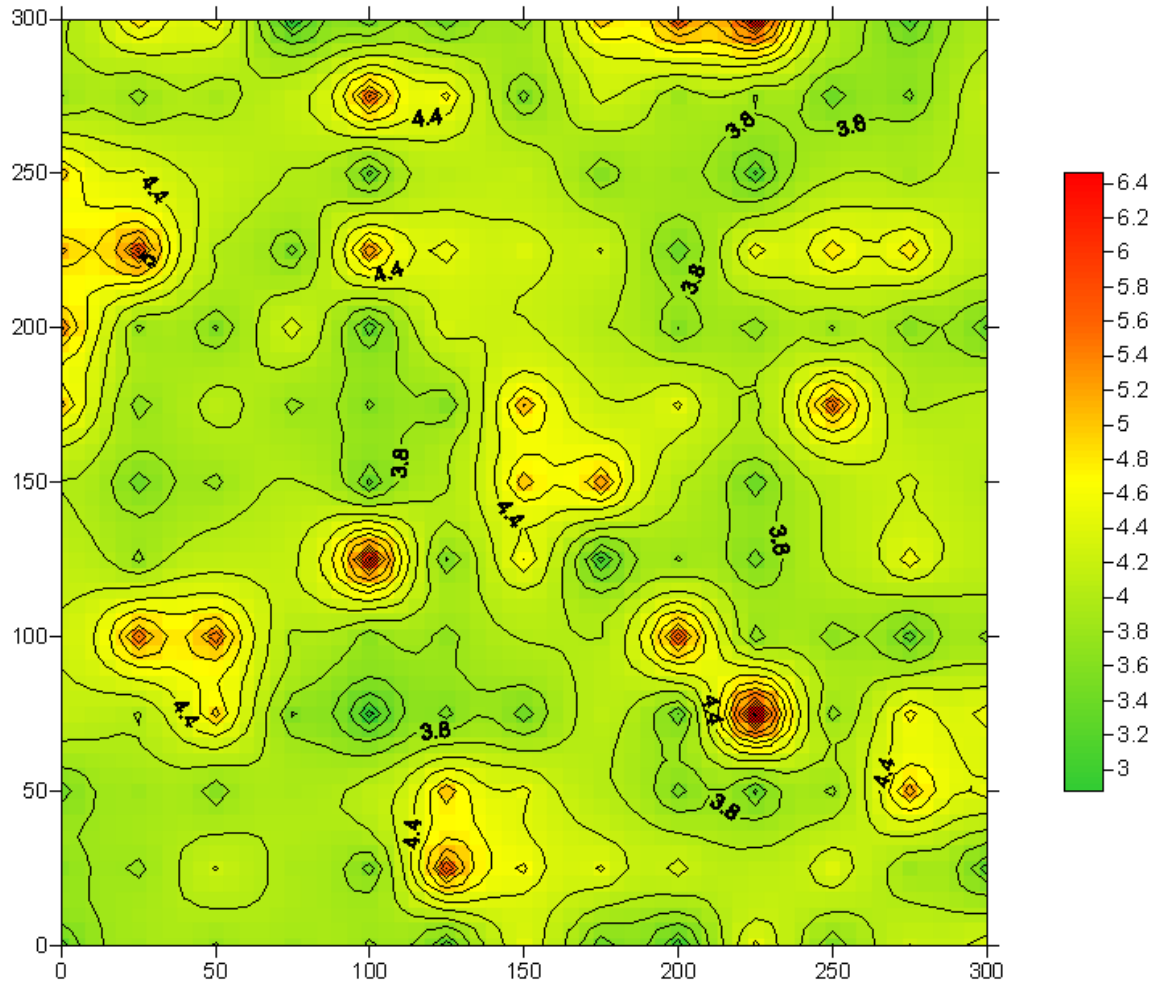
8.5 Interpolation maps

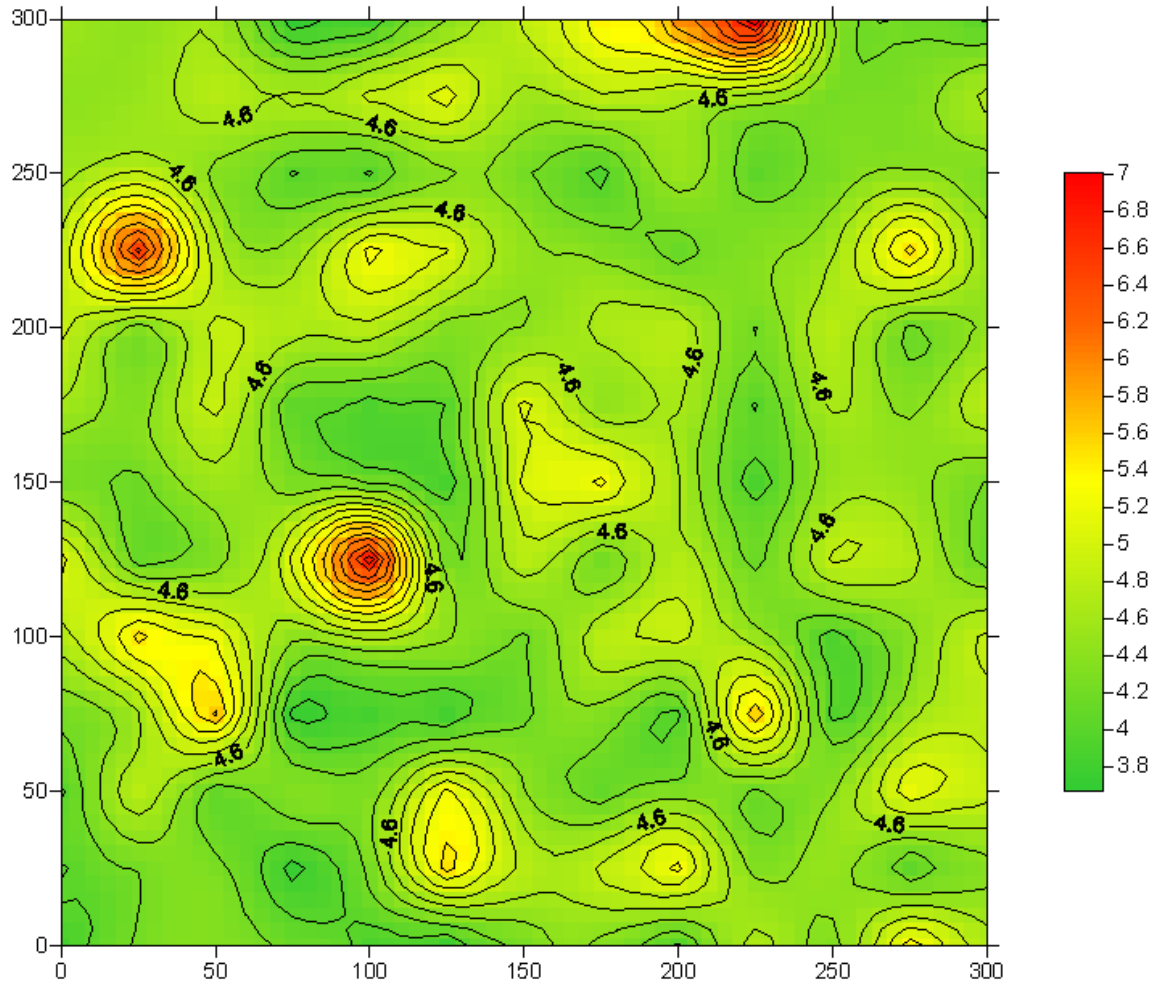
8.5.1 YOK/I

$L_e(60^\circ, \text{st}, \text{YOK/I})$

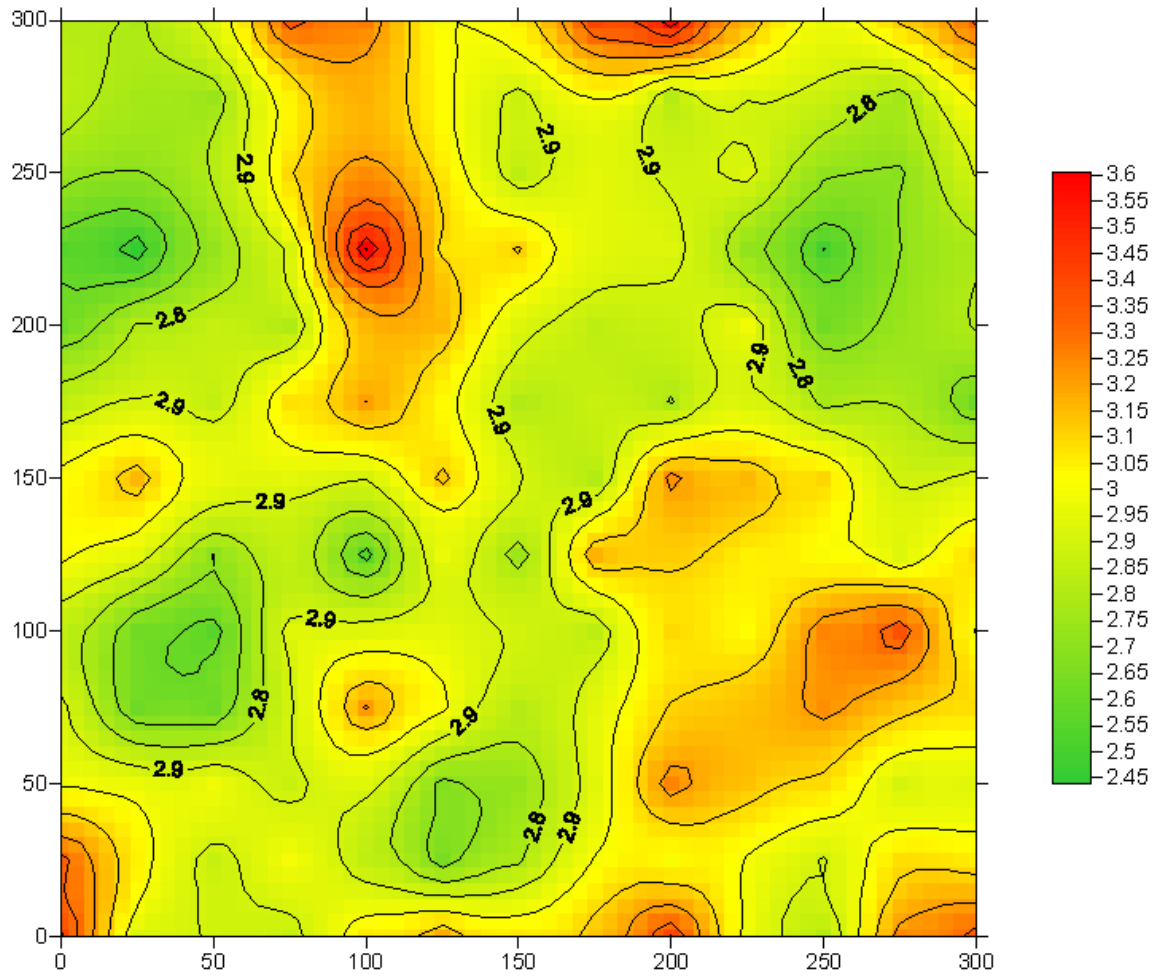


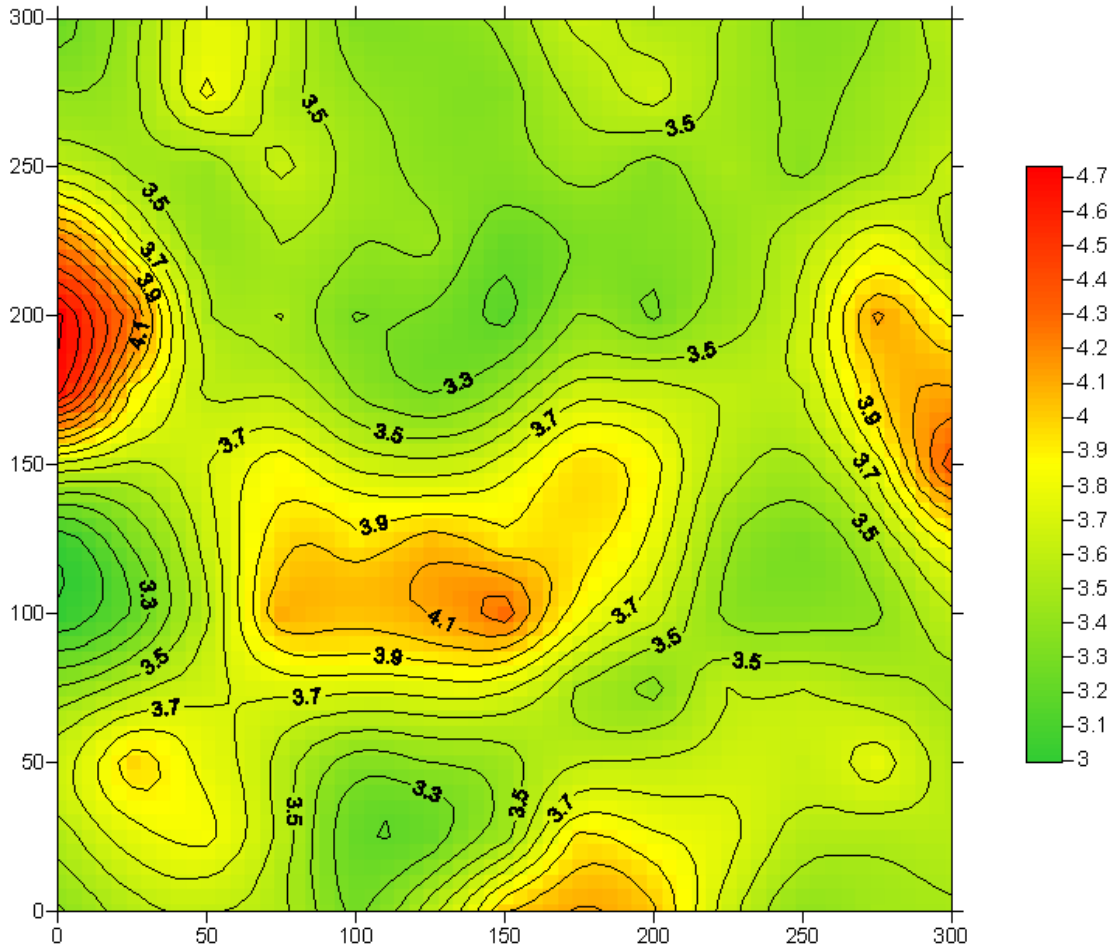
$L_e(75^\circ, \text{st}, \text{YOK/I})$ 

$L_e(60^\circ, ue, YOK/I)$ 

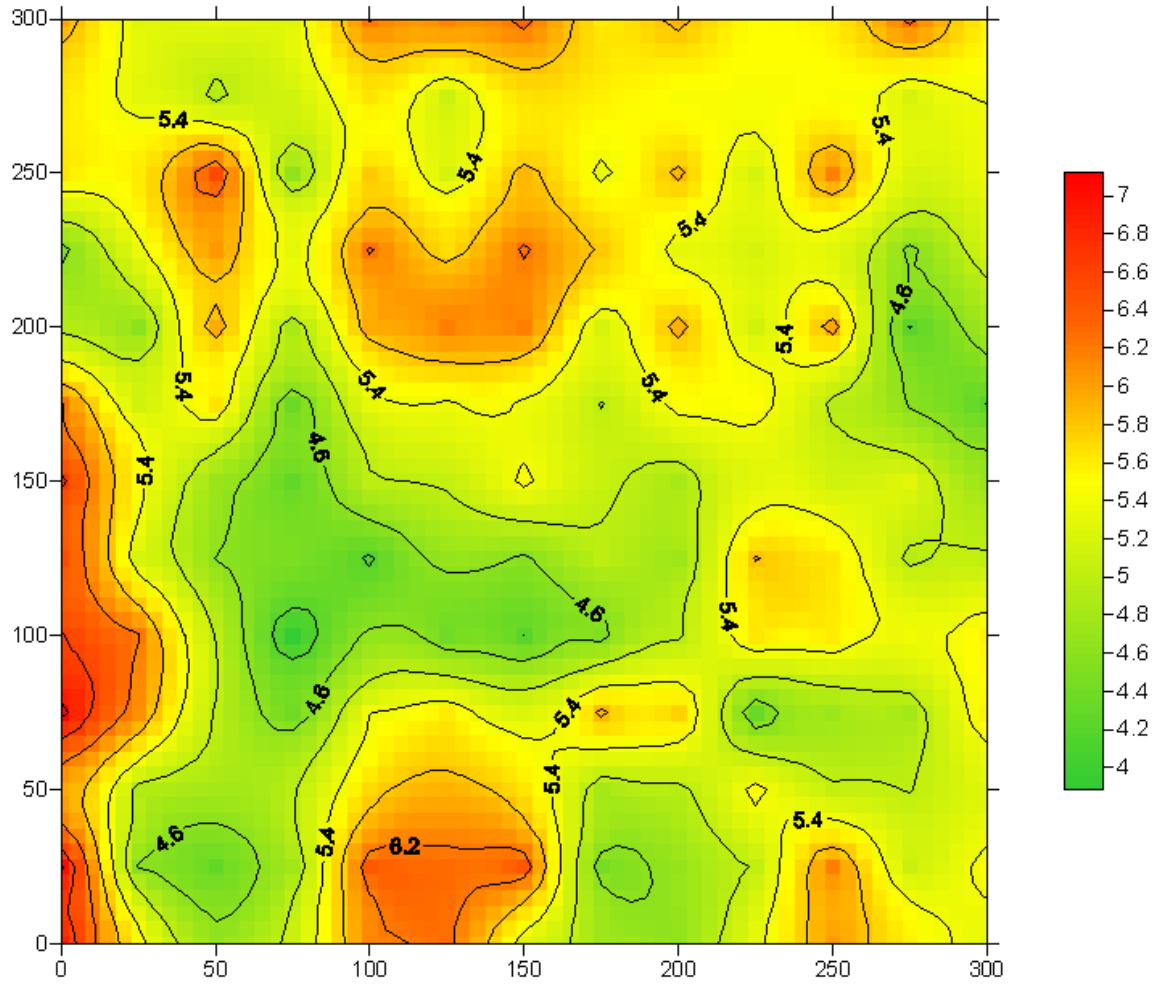
$L_e(75^\circ, ue, YOK/I)$ 

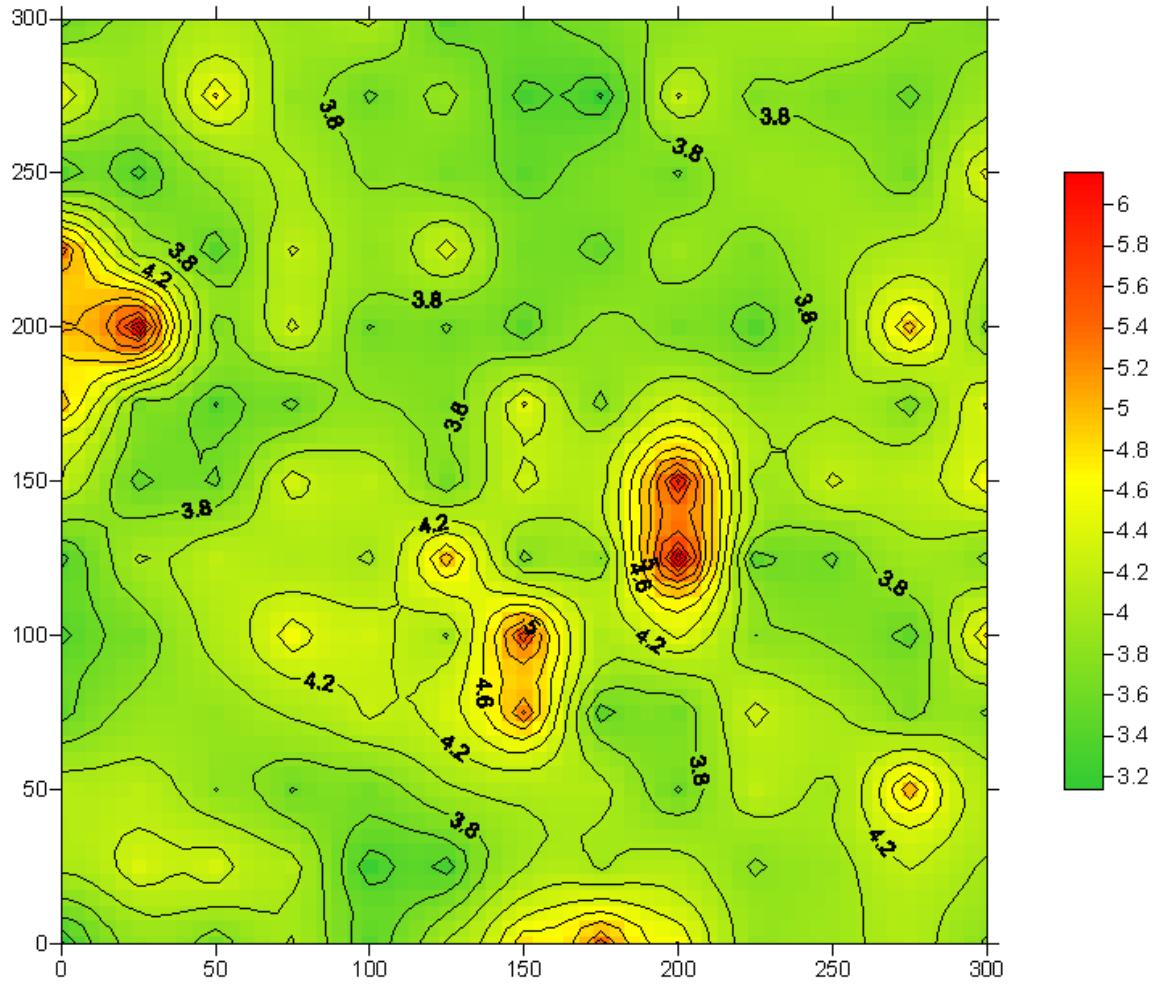
CO(% ue, YOK/I)

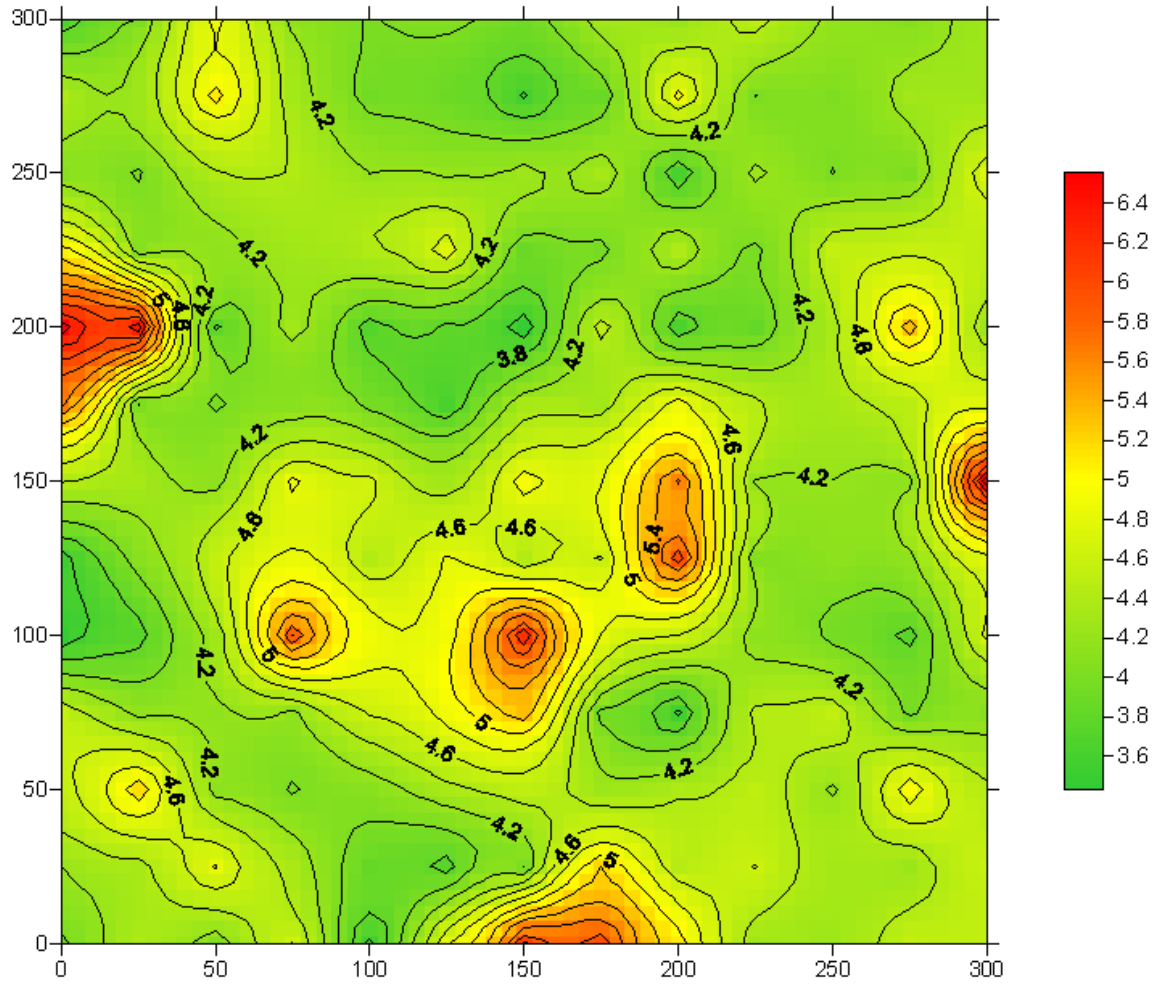


$L_e(75^\circ, \text{st, YOK/II})$ 

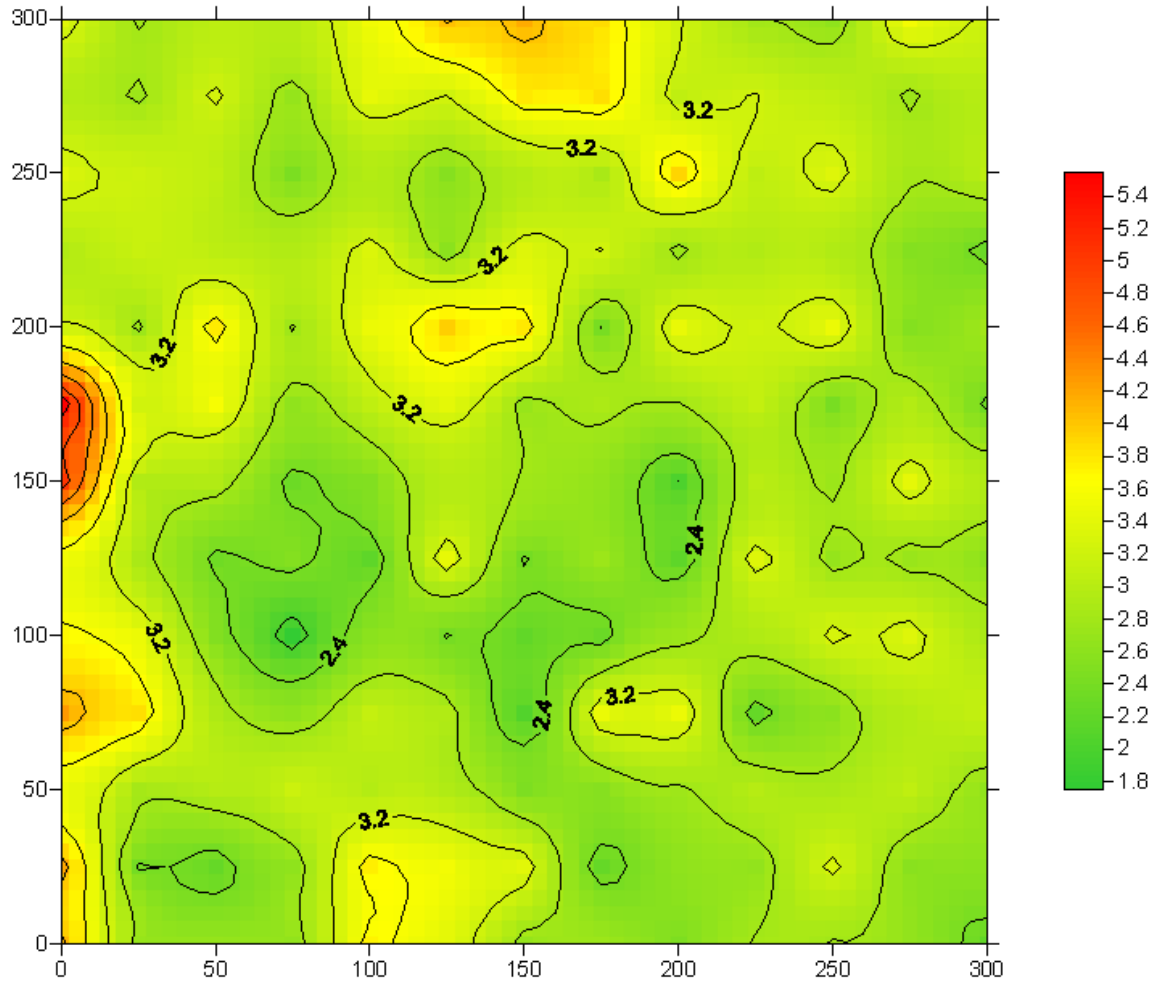
CO(% st, YOK/II)



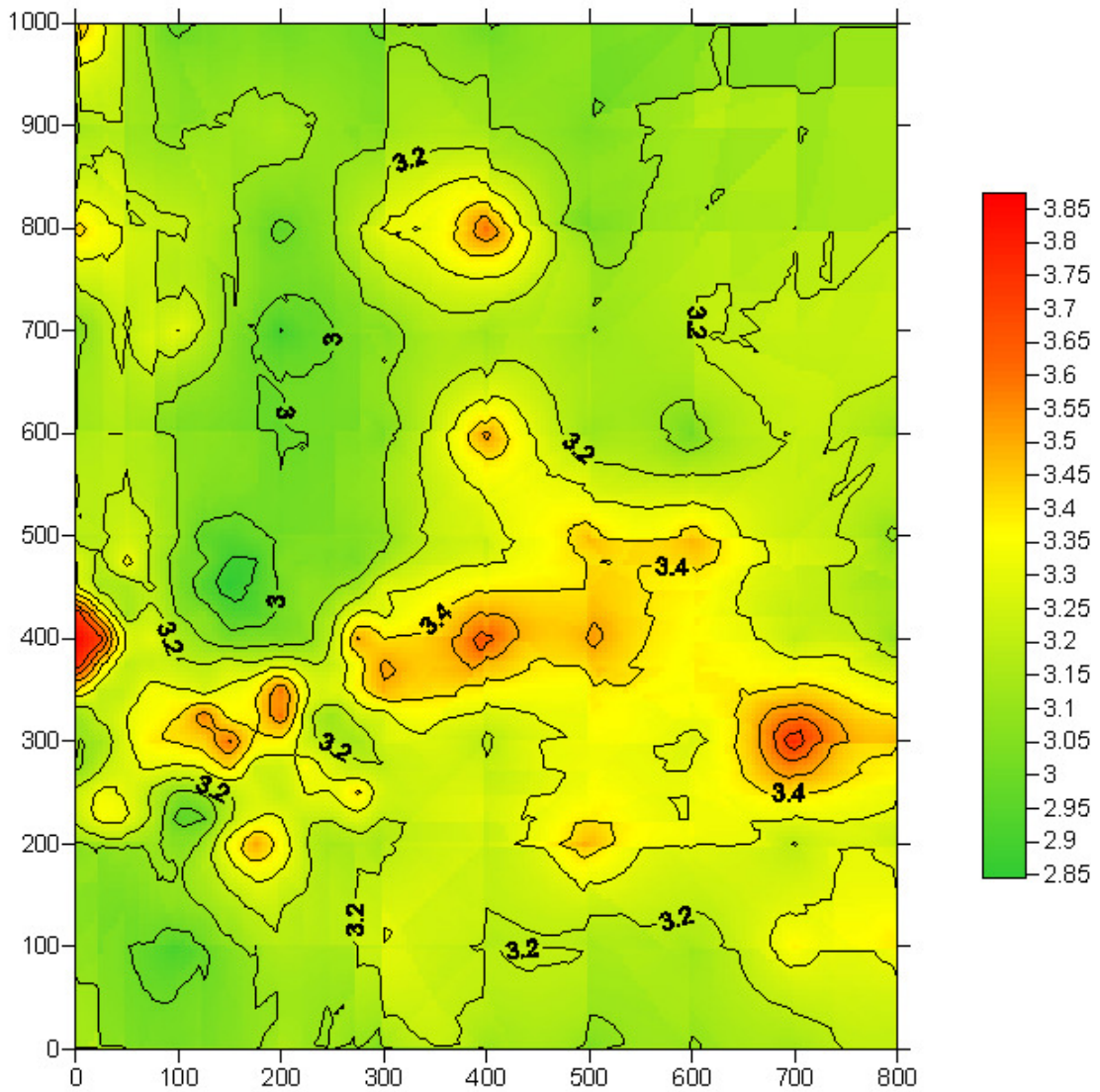
$L_e(60^\circ, ue, YOK/II)$ 

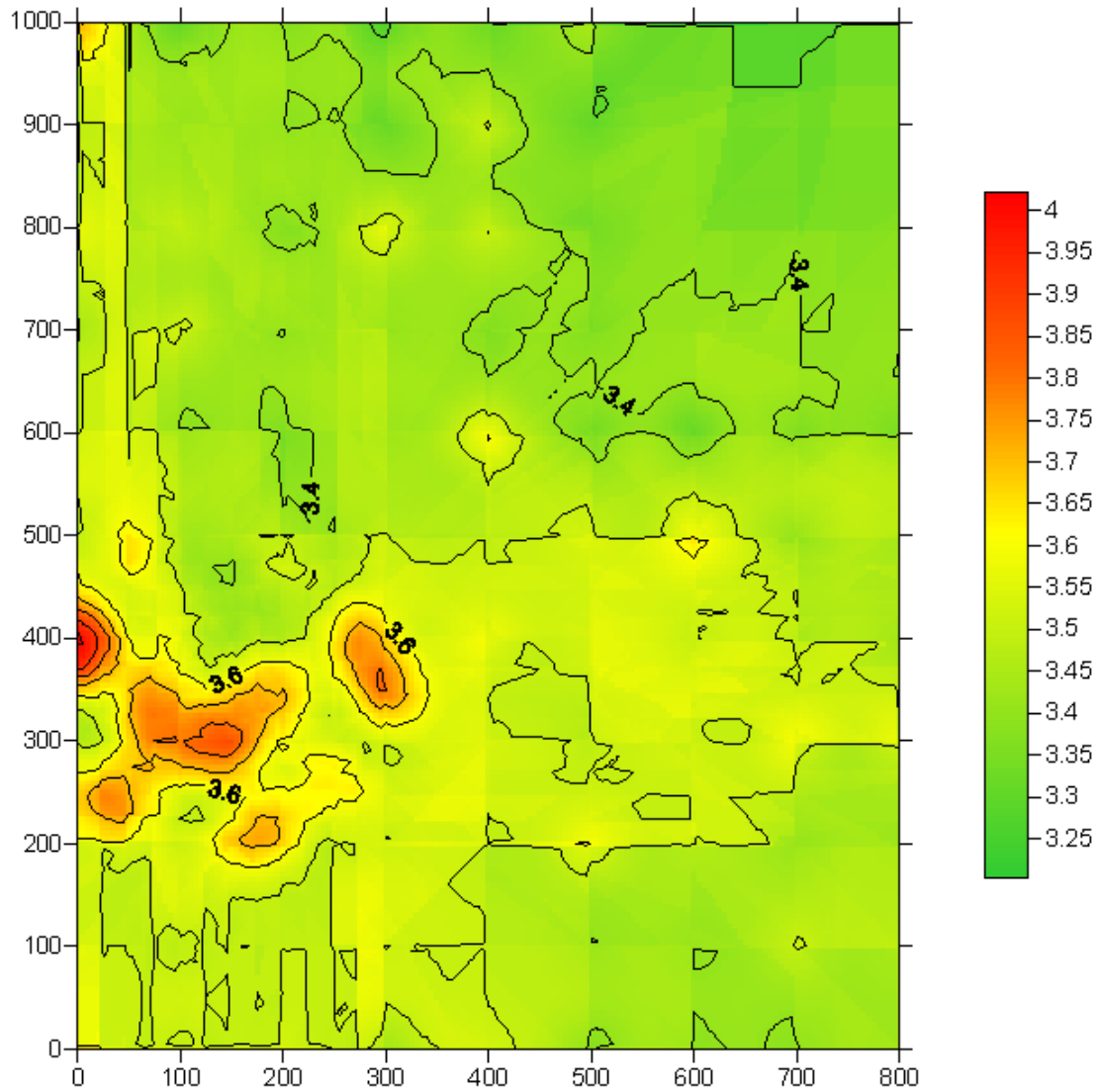
$L_e(75^\circ, ue, YOK/II)$ 

CO(% ue, YOK/II)

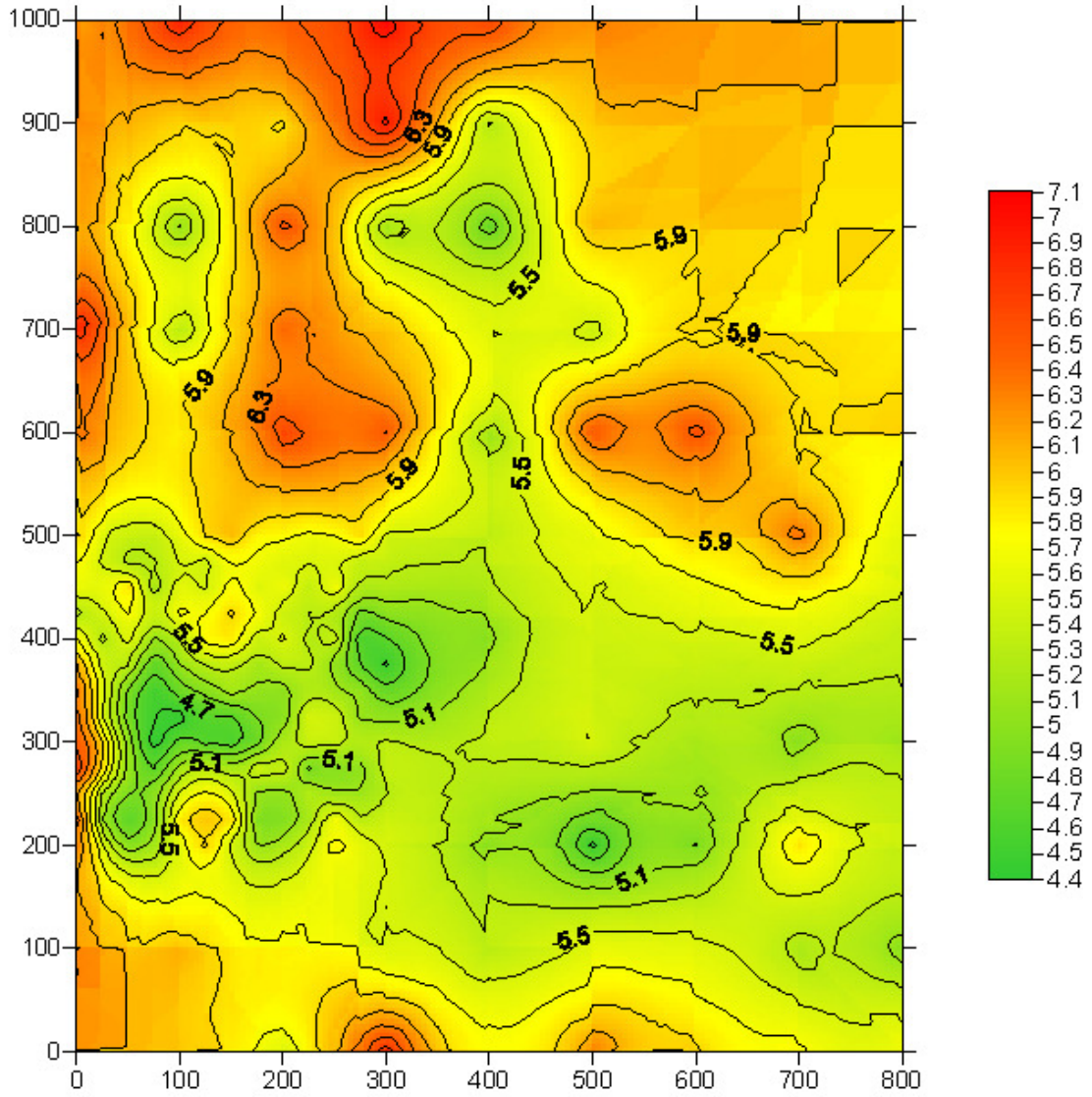


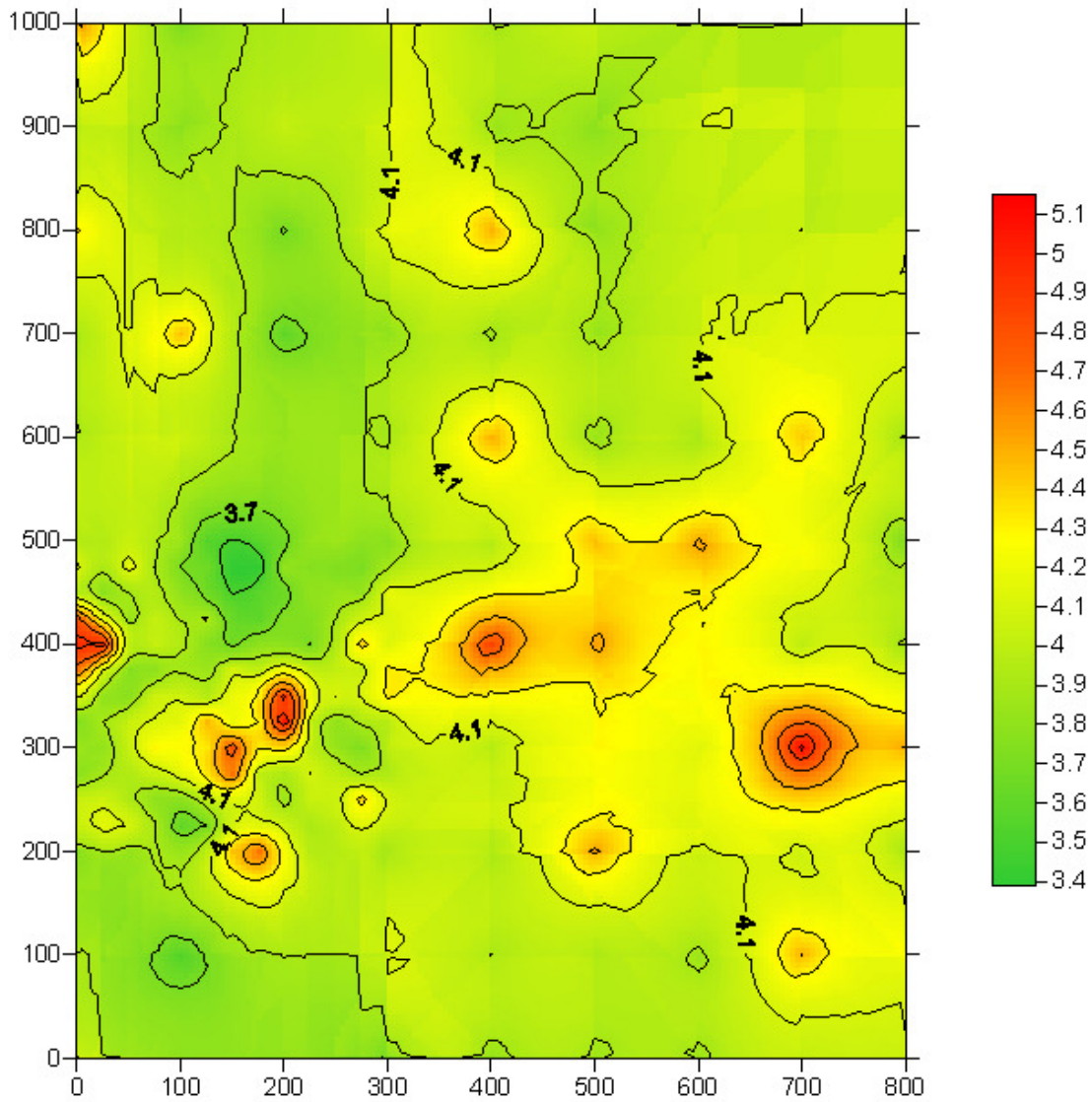
8.5.3 YOK/II/III

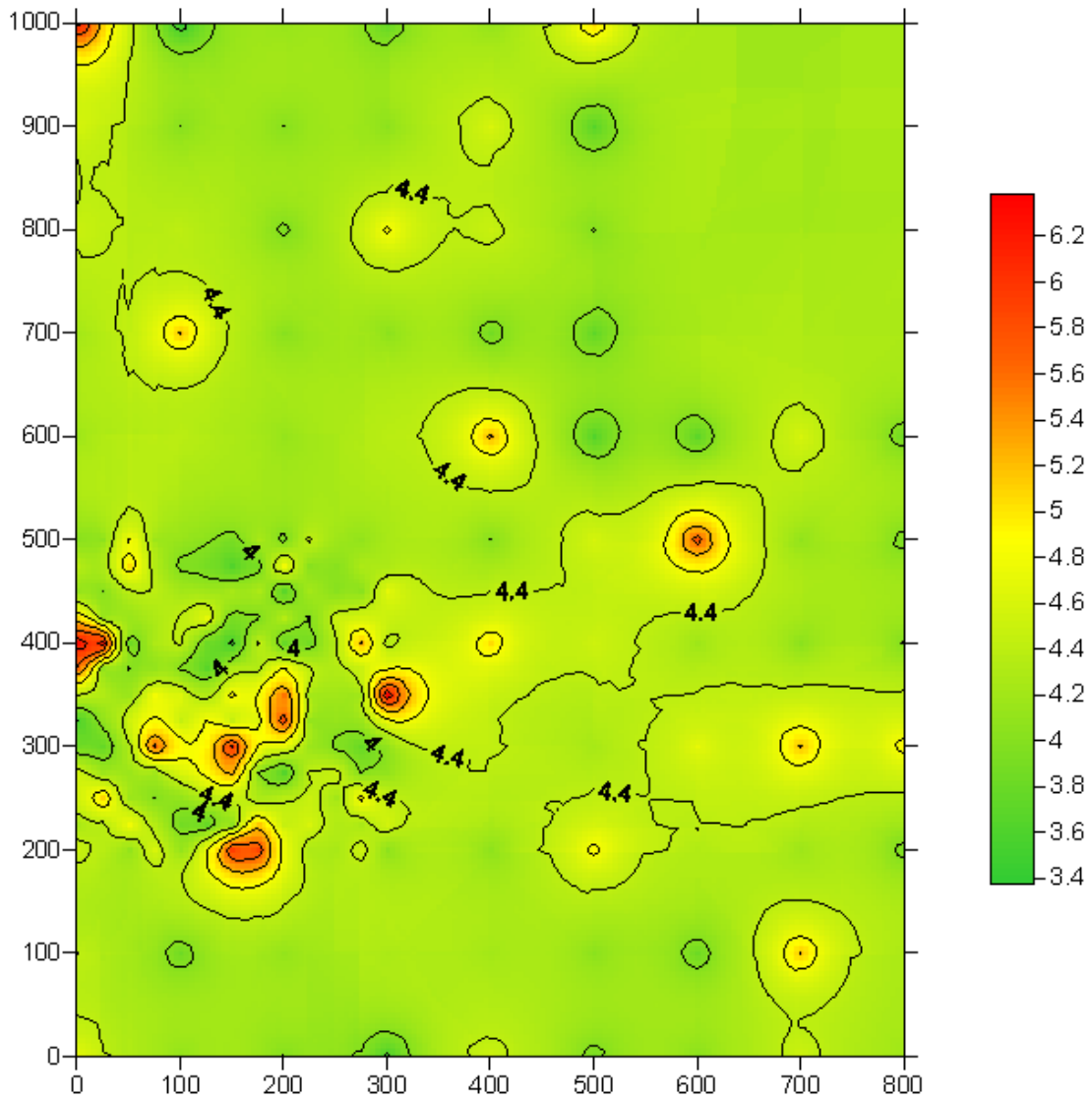
 $L_e(60^\circ, \text{st}, \text{YOK/II/III})$ 

$L_e(75^\circ, \text{st, YOK/II/III})$ 

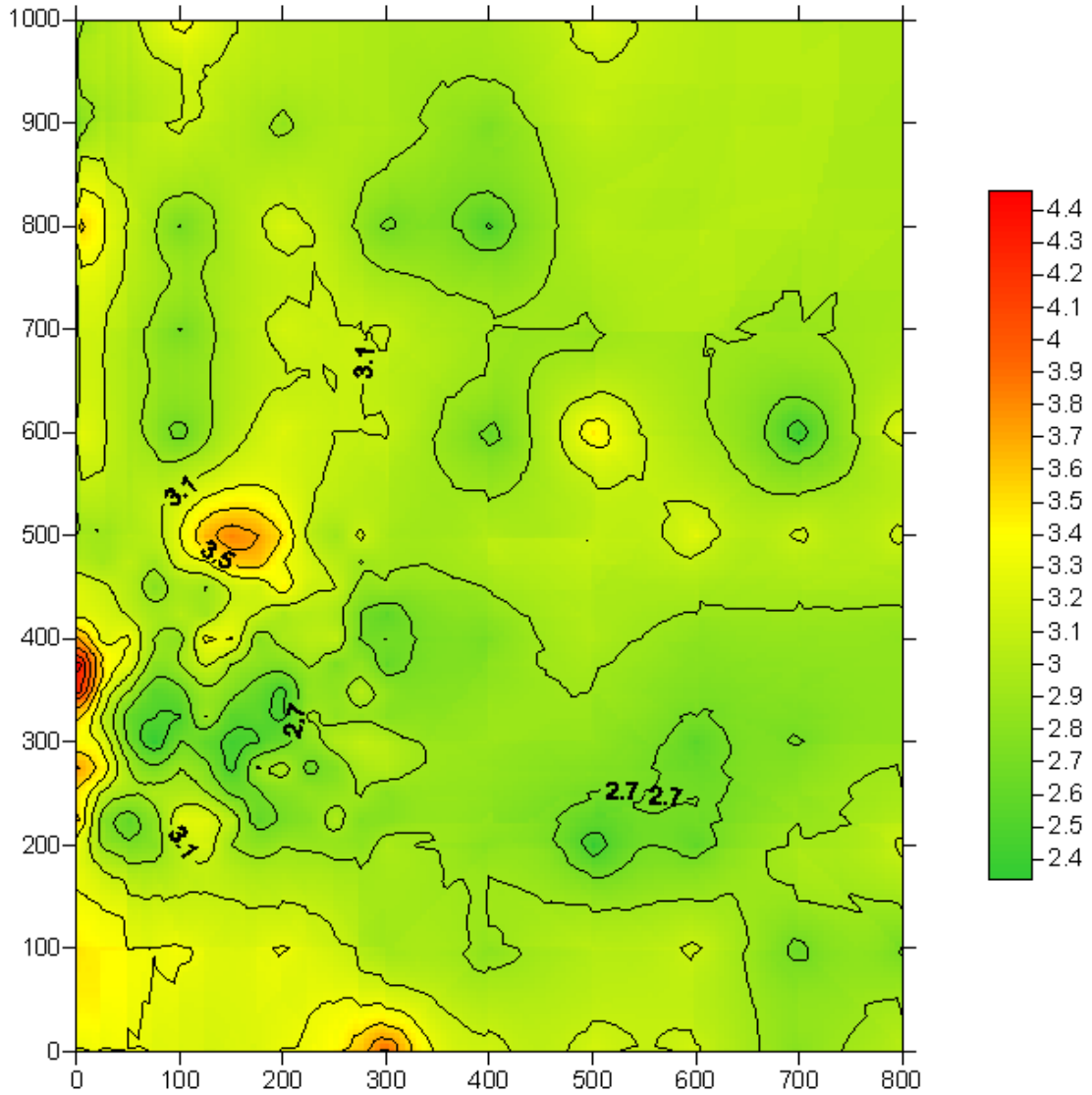
CO(% st, YOK/II/III)



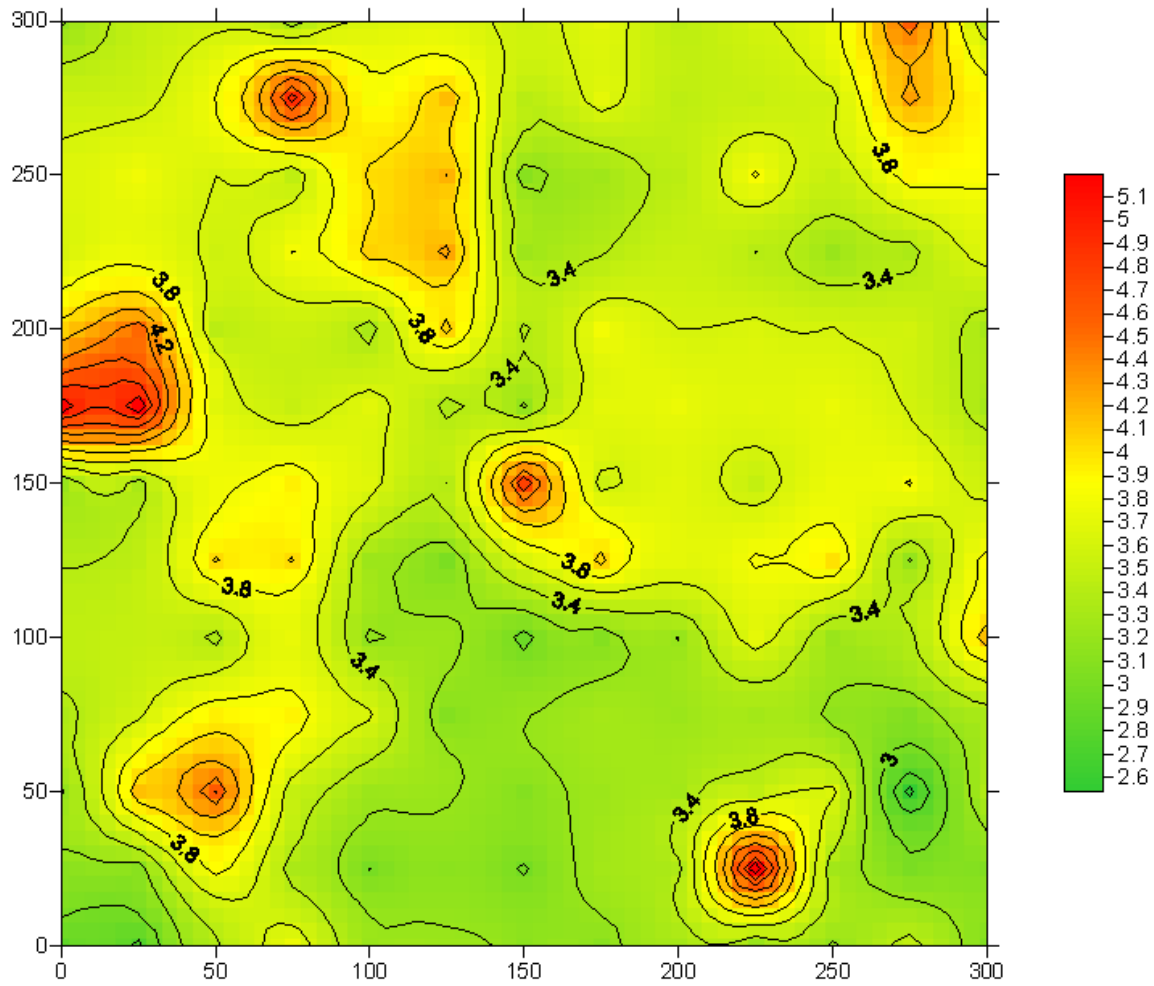
$L_e(60^\circ, ue, YOK/II/III)$ 

$L_e(75^\circ, ue, YOK/II/III)$ 

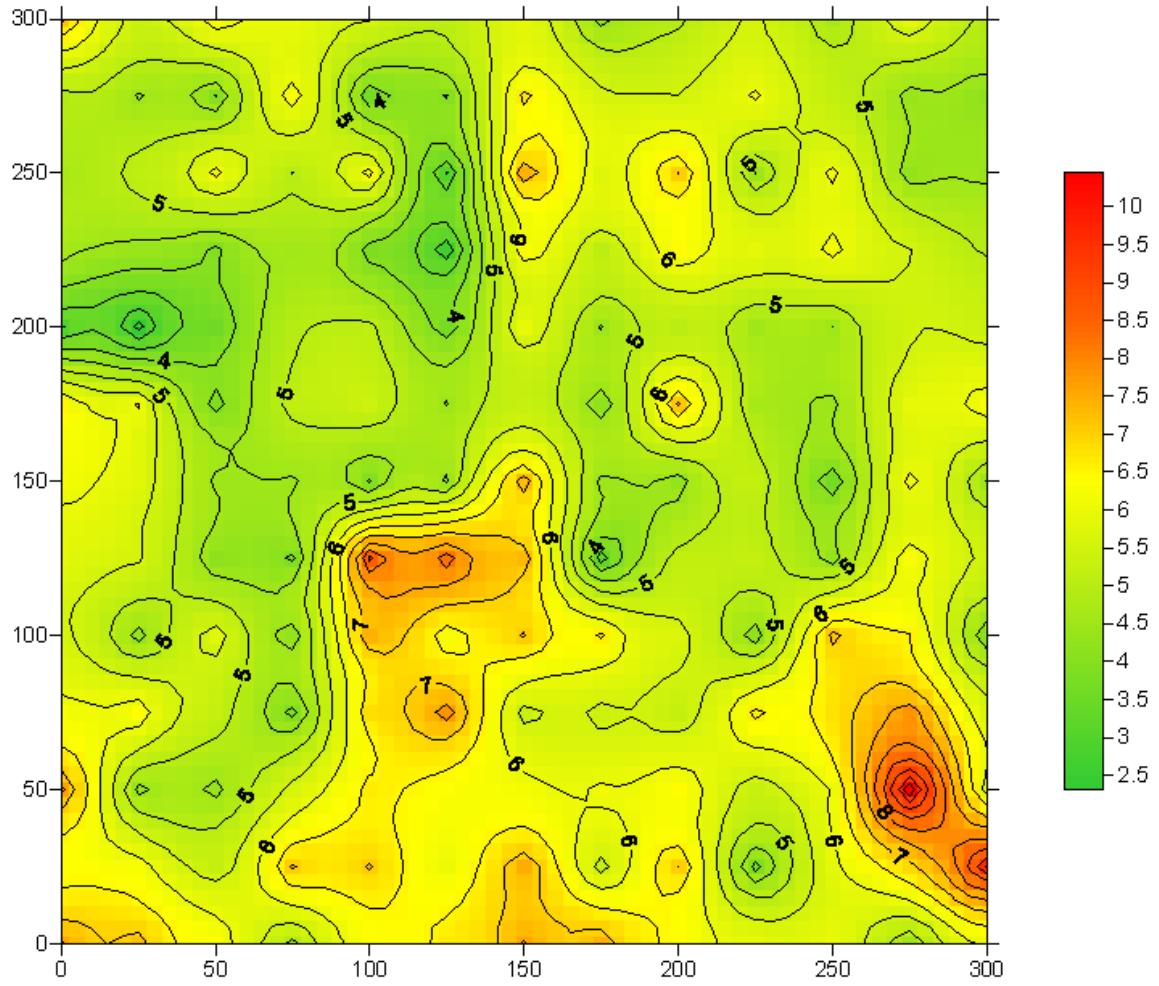
CO(% ue, YOK/II/III)

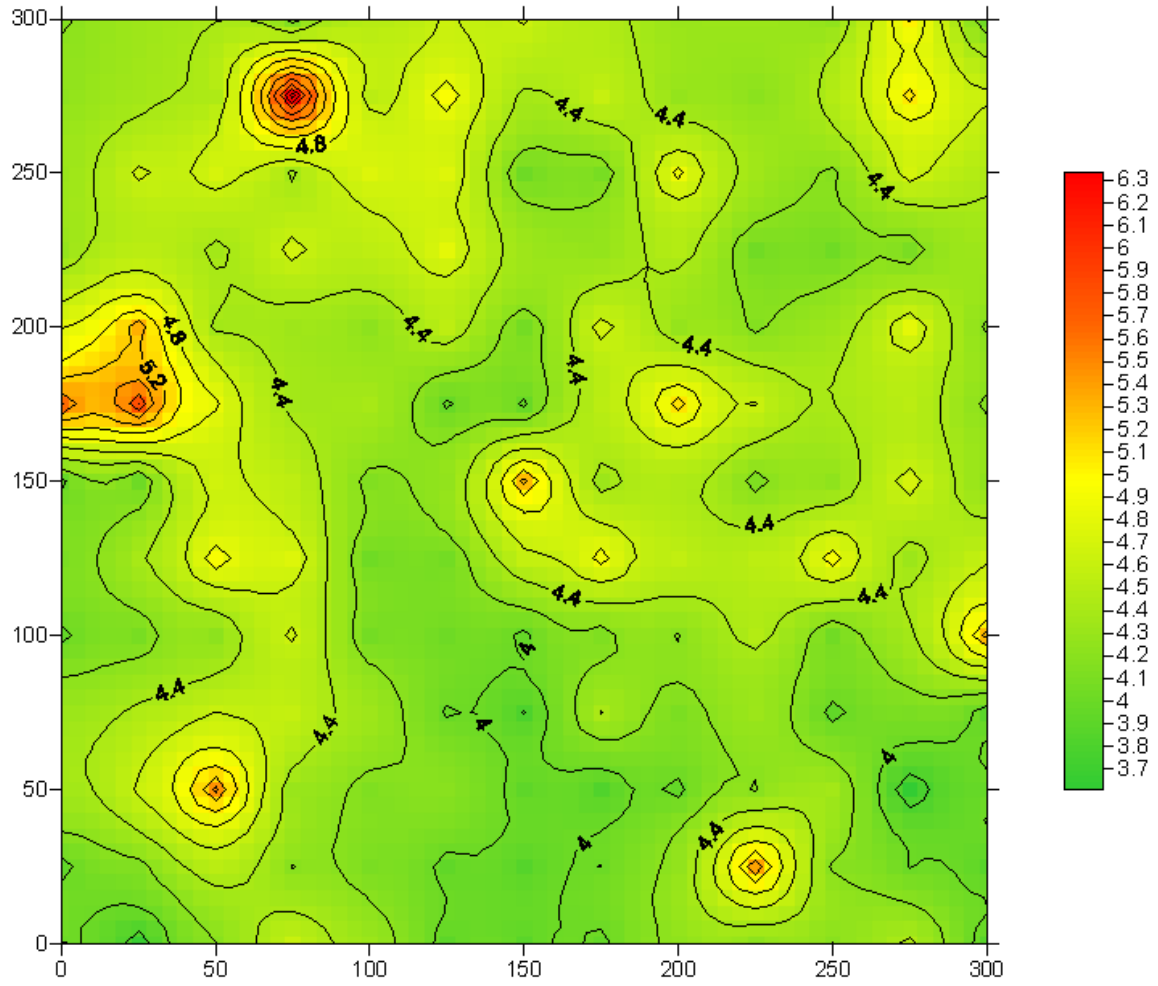


8.5.4 YAN/I

 $L_e(75^\circ, \text{st}, \text{YAN/I})$ 

CO(% st, YAN/I)



$L_e(75^\circ, ue, YAN/I)$ 

CO(% ue, YAN/I)

